

Syracuse University

SURFACE at Syracuse University

Dissertations - ALL

SURFACE at Syracuse University

1-24-2024

Development of Stochastic and Time-Dependent Quantum Chemical Methods for Accurate Description of Light-Matter Interactions with Applications in Photoionization and Inverse Photoemission in Nanomaterials

Nicole Spanedda
Syracuse University

Follow this and additional works at: <https://surface.syr.edu/etd>

 Part of the [Computational Chemistry Commons](#)

Recommended Citation

Spanedda, Nicole, "Development of Stochastic and Time-Dependent Quantum Chemical Methods for Accurate Description of Light-Matter Interactions with Applications in Photoionization and Inverse Photoemission in Nanomaterials" (2024). *Dissertations - ALL*. 1840.
<https://surface.syr.edu/etd/1840>

This Dissertation is brought to you for free and open access by the SURFACE at Syracuse University at SURFACE at Syracuse University. It has been accepted for inclusion in Dissertations - ALL by an authorized administrator of SURFACE at Syracuse University. For more information, please contact surface@syr.edu.

Abstract

There are three main focuses of this work. First, the theoretical details of the Stratified Stochastic Enumeration of Molecular Orbitals (SSE-MO) method is presented, along with its application for calculating ionization potentials (IPs) of quantum dots. The SSE-MO method can readily be applied for the purpose of efficiently and accurately calculating ionization potentials, by constructing the frequency-dependent self-energy operator and then subsequently, solving the associated Dyson equation. Constructing the frequency-dependent self-energy operator is challenging because the scaling of the computational cost with respect to system size, becomes prohibitive for large systems, such as quantum dots. This is due to the large number of 2particle-1hole (2p1h) and 1particle-2hole (1p2h) terms that must be computed. The key strategy of the SSE-MO method is to utilize a stratified stochastic enumeration scheme in order to efficiently construct the 2p1h and 1p2h terms of the self-energy operator, while maintaining high accuracy.

Second, a computational and theoretical investigation into the inverse photoemission processes in a variety of quantum dots (CdS, CdSe, PbS, and PbSe) is presented. Inverse photoemission occurs when an incident electron is captured by a material in one of the high energy unoccupied states. This captured electron then subsequently de-excites to a lower energy unoccupied state, resulting in the emission of a photon. We investigated the inverse photoemission (IPE) processes in these dots, both in the absence of an external electric field and when the dots are in the presence of a Stark field. In order to construct the spectra for the CdS, CdSe, PbS, and PbSe dots, we combined the Frequency-Dependent Geminal-Screened interaction kernel method (FD-GSIK) with time-dependent perturbation theory. Studying the inverse photoemission processes in quantum dots, can provide insight that is valuable for a variety of applications including, but not limited to, the development of scintillators and for achieving a greater understanding of the surface chemistry of materials. Additionally, investigation into the impact of Stark fields on the IPE processes in these materials can provide important information that can aid in the identification of materials that are useful for electroluminescence applications and for the development of new highly controllable photon sources. Furthermore, investigating the effects of the direction and magnitude of Stark fields on the IPE spectra of materials can provide a route to systematically enhance inverse photoemission transition probabilities and alter the energy of the emitted photon.

The third focus of this work, is a theoretical and computational investigation into field-assisted photoionization in PbS clusters and quantum dots. In particular, the results from this investigation into how the IPs, for ionization from the HOMO, of Pb_4S_4 , $\text{Pb}_{44}\text{S}_{44}$, and $\text{Pb}_{140}\text{S}_{140}$ are impacted by the application of non-ionizing Stark fields, of differing strengths and directions. The ability to control the position of the energy levels in quantum dots is highly relevant for the optimization of optoelectronic devices. In order to obtain a first-order approximation to the field-dependent Green's function IPs, of these PbS systems, we employed the recently developed SSE-MO method

accompanied by the use of a Padé approximation. The results presented in this chapter indicate that the ionization potentials of PbS clusters and quantum dots can be manipulated by carefully fine-tuning the magnitude and direction of applied static electric fields.

**Development of Stochastic and Time-Dependent Quantum
Chemical Methods for Accurate Description of Light-Matter
Interactions with Applications in Photoionization and Inverse
Photoemission in Nanomaterials**

by

Nicole Spanedda

B.S., Fairleigh Dickinson University, 2018

M.Phil., Syracuse University, 2020

Dissertation

Submitted in partial fulfillment of the requirements for the degree of
Doctor of Philosophy in Chemistry.

Syracuse University
December 2023

Copyright © Nicole Spanedda 2023
All rights reserved.

Acknowledgements

I would like to begin by thanking my research advisor, Professor Chakraborty, for his guidance during my pursuit of my PhD. Professor Chakraborty has been a truly superb and patient mentor with an unparalleled ability and willingness to teach and explain even the most subtle details of extremely complex topics in quantum chemistry, computer science, and numerical analysis. By encouraging me to gain a broader range of quantum chemistry method development experience, he has provided me with the opportunity to gain a strong knowledge base in quantum theory, while at the same time developing a versatile set of skills that are universally relevant to the broad field of theoretical and computational physical science. Professor Chakraborty is not only an excellent teacher, but he is also an extremely understanding mentor who truly cares about his students. Because of his guidance and mentorship, I feel thoroughly prepared to begin my career as a research scientist. Additionally, I would like to thank Professor Acharya, Professor Chaiken, Professor Chakraborty, Professor Korter, Professor Mohan, and Professor Zheng for taking the time to serve as members of my thesis defense committee. I also want to thank the Syracuse University Department of Chemistry faculty and staff. I especially want to acknowledge Jodi Randall for always being available to help me sort out logistical and bureaucratic issues. I also want to thank my lab-mates, Dr. Jeremy A. Scher, Dr. Peter F. McLaughlin, Kameron Shrum, Chengpeng Gao, Chandler Martin, Jessica Beyer, and Kevin Mesta, for their camaraderie and the enjoyable conversations.

I want to thank my family for all of their support and encouragement. Specifically, I want to thank my brother, John, for his consistent support and his genuine interest in my research, including the complicated mathematical details of my research. During my time at Syracuse University, spending time with my brother has been one of things that I looked forward to most when going home to visit my family. Last but not least, I truly appreciate that John has always had the utmost confidence in me and my ability to earn my PhD. I also want to thank my mother and father for all of their support. I specifically want to thank my mother for the unwavering encouragement and support. My mom truly understands the challenges and rigors of pursuing an advanced degree and because of this she has been a source of invaluable support for me. Also, she has always made a point of learning about and understanding the topics of my research. I specifically want to thank my father for both encouraging me during my pursuit of my PhD and always being interested in learning about the different aspects of my research, including the technological applications of my research. I also want to thank my dad for always being available on short notice to help me handle any unexpected challenges and problems. Additionally, I would like to thank the rest of my family for their support. I have been truly fortunate to have so many supportive family members. In fact, I have so many family members to acknowledge that it is impractical mention all of them here.

Additionally, I want to acknowledge my friends. In particular, I would like to acknowledge

my sister-in-law and friend, Sue Spanedda. Spending time with Sue has always been a fun and enjoyable part of my visits home. I also want to acknowledge my lifelong friend, Matt Schneider. Although, we have not had the opportunity to spend much time together during the past few years, Matt has always been interested to know how I am doing and is always excited to hear about my research. Last but not least, I especially want to acknowledge Kameron Shrum. I first met Kameron when he joined the Chakraborty group as an REU student. Since then, Kameron has become one of my closest friends. I consider my friendship with Kameron to be one of the best and most valuable things that I have gained during my time at Syracuse.

I also would like to acknowledge the National Science Foundation for supporting this research under Grant No. CHE-2102437, CHE-1950802, ACI-1341006, ACI-1541396. Additionally, I would like to acknowledge Syracuse University for providing computational resources which enabled the conduction of the research presented in this dissertation.

Contents

Acknowledgements	v
Contents	vii
List of Tables	ix
List of Figures	x
1 Introduction	1
2 Quantum Chemistry Background	4
2.1 Scope of Chapter Content	4
2.2 The Hartree-Fock Method and Koopmans' Theorem	4
2.3 Basic Mathematical Introduction to Green's Function Theory	7
2.4 One-Particle MBGF: Hartree-Fock Green's Function	9
3 Background: Monte Carlo Integration	10
3.1 Basics of Naive Monte Carlo integration	10
3.2 Monte Carlo Numerical in Higher Dimensions	11
3.3 Stratified Sampling	13
3.4 Control Variate Technique with Common Random Number Sampling	14
3.5 Ratio estimator with Common Random Number Sampling	17
4 Introduction to Summation by Stochastic Enumeration and Stratified Stochastic Enumeration	18
4.1 Stochastic Enumeration for Computing Sums	18
4.2 Stratified Stochastic Enumeration for Computing Sums	19
5 Stratified Stochastic Enumeration of Molecular Orbitals method: Applied for Investigation of Ionization Potential in Quantum Dots	20
5.1 Scope of Chapter Content	20
5.2 Introduction	21
5.3 Theory	24
5.4 Results	37
5.5 Discussion	44
5.6 Conclusions	52
6 Background: Time-Dependent Schrödinger Equation and Time-dependent Perturbation Theory	53
6.1 Scope of Chapter Content	53
6.2 Time-Dependent Schrödinger Equation	53

6.3	Introduction to Time-dependent Perturbation Theory: First-Order	54
7	Enhancement of Spontaneous Photon Emission in Inverse Photoemission Transitions in Semiconductor Quantum Dots	56
7.1	Scope of Chapter Content	56
7.2	Introduction	57
7.3	Theory	59
7.4	Results	64
7.5	Discussion	79
7.6	Future Directions	80
8	Nonlinear Stark effect and field-assisted photoionization in PbS semiconductor quantum dots	81
8.1	Scope of Chapter Content	81
8.2	Introduction	81
8.3	Theory	82
8.4	Results and Discussion	85
8.5	Conclusions	89
	Bibliography	91

List of Tables

5.1	Ionization potentials (eV) of ten electron systems: comparison with benchmark literature values	38
5.2	Self-energy and Ionization Potentials (eV) of PbS and CdS Quantum Dots from Single-shot Solution	41
5.3	Self-energy and Ionization Potentials (eV) of PbS and CdS Quantum Dots from Iterative Solution	42
5.4	Computational time for constructing self-energy: SSE-MO vs. Sequential Enumeration	42
5.5	Total number of sampling points in the combined MO-Cartesian space assuming 100 points per Cartesian coordinate.	45
7.1	Electric Field Vector Information	67
7.2	Percent change in maximum relative transition probabilities for electric fields along x, y, and z directions (Equation 7.1).	67
7.3	Change in emitted photon energies (eV) at the maximum relative transition probabilities for electric fields aligned along x, y, and z directions (Equation 7.2).	69
7.4	Overall change in the IPE spectra for maximally coupled directed Stark fields (Equation 7.3).	76
8.1	Electric field vector magnitudes	84

List of Figures

5.1	The percent contribution of terms A_i^{2p1h} and A_i^{1p2h} (defined in Equation 5.5) to the total self-energy as a function of hole index (i) for Pb_4S_4	23
5.2	Curve labeled ω intersects with the curve labeled $\omega_0 + \Sigma$ at the value of ω for which the diagonal approximation to the Dyson equation converges, for $\text{Pb}_{140}\text{S}_{140}$	39
5.3	Poles of $G_0(\omega)$ and $G(\omega)$ for Pb_4S_4	40
5.4	Poles of $G_0(\omega)$ and $G(\omega)$ for $\text{Pb}_{44}\text{S}_{44}$	40
5.5	Poles of $G_0(\omega)$ and $G(\omega)$ for $\text{Pb}_{140}\text{S}_{140}$	41
5.6	A_{wp}/A_{wp}^{\max} (ordinate) plotted as a function of $\omega/\omega_{\text{opt}}$ (abscissa) for PbS systems. A_{wp}/A_{wp}^{\max} is the ratio of $A_{\text{sp}}(\omega)$ and the maximum value of $A_{\text{sp}}(\omega)$. ω_{opt} is the value of ω at which diagonal approximation to the Dyson equation converges.	43
5.7	A_{wp}/A_{wp}^{\max} (ordinate) plotted as a function of $\omega/\omega_{\text{opt}}$ (abscissa) for CdS systems. A_{wp}/A_{wp}^{\max} is the ratio of $A_{\text{sp}}(\omega)$ and the maximum value of $A_{\text{sp}}(\omega)$. ω_{opt} is the value of ω at which diagonal approximation to the Dyson equation converges.	44
5.8	Cumulative sum of the percent contributions of the segments composing the sample space for the 2p1h and 1p2h terms of the self-energy (ordinate) versus the segment index (abscissa) for Pb_4S_4 (Figure A), $\text{Pb}_{44}\text{S}_{44}$ (Figure B), and $\text{Pb}_{140}\text{S}_{140}$ (Figure C).	46
5.9	Cumulative sum of the percent contributions of the segments composing the sample space for the 2p1h and 1p2h terms of the self-energy (ordinate) versus the segment index (abscissa) for Cd_6S_6 (Figure A), $\text{Cd}_{24}\text{S}_{24}$ (Figure B), and $\text{Cd}_{45}\text{S}_{45}$ (Figure C).	47
5.10	Frequency distributions of the standard deviations (units of eV) for the segments that compose the sample space of the 2p1h and 1p2h terms of the self-energy operator for $\text{Pb}_{140}\text{S}_{140}$	48
5.11	Frequency distributions of the standard deviations (units of eV) for the segments that compose the sample space of the 2p1h and 1p2h terms of the self-energy operator for $\text{Cd}_{45}\text{S}_{45}$	48
5.12	Sample standard deviation ($\sigma_{\bar{x}}$) in ionization potential (units of eV) versus the number of sampling points used to construct the self-energy for $\text{Pb}_{140}\text{S}_{140}$	49

7.1	Impact of Stark field on IPE process. Incoming electrons have a distribution of kinetic energies (shown in purple). Application of external electric field changes the molecular orbital energies (shown in green) and the frequency of the emitted photon ($\hbar\omega_{\text{field-on}}$, shown in red).	58
7.2	Feynman–Goldstone diagram for the first-order approximation to the inverse photoemission transition amplitude.	62
7.3	Subplots A and B (relative transition probability versus ω) display the inverse photoemission spectra obtained using the FD-GSIK method and MBPT for the $\text{Cd}_{24}\text{S}_{24}$ and $\text{Cd}_{45}\text{S}_{45}$ quantum dot, respectively.	64
7.4	Subplots A and B (relative transition probability versus ω) display the inverse photoemission spectra obtained using the FD-GSIK method and MBPT for the $\text{Cd}_{24}\text{Se}_{24}$ and $\text{Cd}_{54}\text{Se}_{54}$ quantum dots, respectively.	65
7.5	Subplots A and B (relative transition probability versus ω) display the inverse photoemission spectra obtained using the FD-GSIK method and MBPT for the $\text{Pb}_{44}\text{S}_{44}$ and $\text{Pb}_{140}\text{S}_{140}$ quantum dots, respectively.	65
7.6	Subplots A and B (relative transition probability versus ω) display the inverse photoemission spectra obtained using the FD-GSIK method and MBPT for the $\text{Pb}_{29}\text{Se}_{29}$ and $\text{Pb}_{52}\text{Se}_{52}$ quantum dots, respectively.	66
7.7	Relative transition probability (ordinate) versus ω (abscissa) for $\text{Cd}_{24}\text{S}_{24}$ in the presence of electric fields aligned along the x-direction (Subplot A), y-direction (Subplot B), and z-direction (Subplot C).	68
7.8	Relative transition probability (ordinate) versus ω (abscissa) for $\text{Cd}_{45}\text{S}_{45}$ in the presence of electric fields aligned along the x-direction (Subplot A), y-direction (Subplot B), and z-direction (Subplot C).	69
7.9	Relative transition probability (ordinate) versus ω (abscissa) for $\text{Cd}_{24}\text{Se}_{24}$ in the presence of electric fields aligned along the x-direction (Subplot A), y-direction (Subplot B), and z-direction (Subplot C).	70
7.10	Relative transition probability (ordinate) versus ω (abscissa) for $\text{Cd}_{54}\text{Se}_{54}$ in the presence of electric fields aligned along the x-direction (Subplot A), y-direction (Subplot B), and z-direction (Subplot C).	71
7.11	Relative transition probability (ordinate) versus ω (abscissa) for $\text{Pb}_{44}\text{S}_{44}$ in the presence of electric fields aligned along the x-direction (Subplot A), y-direction (Subplot B), and z-direction (Subplot C).	72
7.12	Relative transition probability (ordinate) versus ω (abscissa) for $\text{Pb}_{140}\text{S}_{140}$ in the presence of electric fields aligned along the x-direction (Subplot A), y-direction (Subplot B), and z-direction (Subplot C).	73
7.13	Relative transition probability (ordinate) versus ω (abscissa) for $\text{Pb}_{29}\text{Se}_{29}$ in the presence of electric fields aligned along the x-direction (Subplot A), y-direction (Subplot B), and z-direction (Subplot C).	74
7.14	Relative transition probability (ordinate) versus ω (abscissa) for $\text{Pb}_{52}\text{Se}_{52}$ in the presence of electric fields aligned along the x-direction (Subplot A), y-direction (Subplot B), and z-direction (Subplot C).	75
7.15	Relative transition probability versus ω for $\text{Cd}_{24}\text{S}_{24}$ (subplot A) and $\text{Cd}_{45}\text{S}_{45}$ (subplot B), in the presence of electric fields with which the dots are maximally coupled, along with the spectra for the E3 field.	77

7.16	Relative transition probability versus ω for $\text{Cd}_{24}\text{Se}_{24}$ (subplot A) and $\text{Cd}_{54}\text{Se}_{54}$ (subplot B), in the presence of electric fields with which the dots are maximally coupled, along with spectra for the E3 field.	77
7.17	Relative transition probability versus ω for $\text{Pb}_{44}\text{S}_{44}$ (subplot A) and $\text{Pb}_{140}\text{S}_{140}$ (subplot B), in the presence of electric fields with which the dots are maximally coupled, along with spectra for the E3 field.	78
7.18	Relative transition probability versus ω for $\text{Pb}_{29}\text{Se}_{29}$ (subplot A) and $\text{Pb}_{52}\text{Se}_{52}$ (subplot B), in the presence of electric fields with which the dots are maximally coupled, along with spectra for the E3 field.	78
8.1	Comparison of Padé approximation IPs and Green's function IPs obtained using first-order approximation (Equation 8.4) and the SSE-MO method, for $\text{Pb}_{140}\text{S}_{140}$. Electric fields are aligned along an axis that is orthogonal with respect to the expectation value of the dipole moment operator of the HOMO.	85
8.2	Impact of static external electric fields on the ionization potentials of Pb_4S_4 , $\text{Pb}_{44}\text{S}_{44}$, and $\text{Pb}_{140}\text{S}_{140}$. The fields were aligned with these systems along axes parallel with respect to the expectation value of the dipole moment operator of their HOMOs.	87
8.3	Impact of static external electric fields on the ionization potentials of Pb_4S_4 , $\text{Pb}_{44}\text{S}_{44}$, and $\text{Pb}_{140}\text{S}_{140}$. The fields were aligned with these systems along axes orthogonal with respect to the expectation value of the dipole moment operator of their HOMOs.	87
8.4	Inter-system comparison of the impact of static external electric fields on the ionization potentials of Pb_4S_4 , $\text{Pb}_{44}\text{S}_{44}$, and $\text{Pb}_{140}\text{S}_{140}$, The fields were aligned with these systems along the x (subplot A), y (subplot B), or z axes (subplot C).	88

Chapter 1

Introduction

Quantum chemistry is a sub-field of chemistry that focuses on achieving a greater theoretical understanding of the properties and behavior of chemical systems by applying quantum mechanics. Quantum chemical methods can also be applied in order to gain a greater understanding of light-matter interactions in chemical systems and materials. Within the framework of quantum theory, light-matter interactions involve the coupling of the quantum states of a system, with electromagnetic radiation. This coupling can induce changes in the states of a chemical system or material and can also initiate the occurrence of various process. Some examples of processes that can be initiated as a result of light-matter interactions include, but are not limited to, photoionization, inverse photoemission, elastic or inelastic scattering, and a variety of other absorption and emission processes.

A major computational bottle-neck for applying traditional first-principles quantum chemistry methods for studying the properties of large chemical systems and materials, is the unfavorable scaling of the computational cost of these methods, with respect to system size. Additionally, when investigating the properties of materials a very large number of electron-electron interactions must be accounted. This in particular can become very computationally prohibitive when applying traditional first-principles quantum chemistry methods for investigating the properties of a variety of materials, including nanomaterials. Nanomaterials are a novel class of materials that have generated alot of interest, due to the highly controllable nature of their electronic properties and their applicability in a variety of areas including, but not limited to, the development of novel electronic devices and the design of more efficient photovoltaic devices. One approach to circumvent the aforementioned computational bottle-necks, associated with the use of traditional first-principles quantum chemistry methods, is to incorporate the use of stochastic methodology. Some examples of stochastic techniques include random and quasi-random sampling, Monte Carlo integration, and stochastic enumeration. Additionally, the use of stochastic techniques can enable the use of well defined metrics for error analysis, along with providing a route to systematically reduce the error in the results obtained from computation. Stochastic techniques can be applied to solve very challenging quantum chemistry problems including, but not limited to, the construction of the frequency-dependent self-energy operator and the implementation of methodology, such as second and third order Møller-Plesset perturbation theory, for very large systems and materials. [114, 125, 122] For example, it has been demonstrated that by applying stratified stochastic enumeration, the ionization potentials of quantum dots can be calculated, by first constructing the frequency-dependent self-energy operator and then solving the associated Dyson equation. [114] The Ionization potential (IP) (or ionization energy) is defined as the energy needed to remove an

electron from a chemical system. Ionization potential is a fundamental property of a material which is relevant to mass spectroscopy, photoelectron spectroscopy, electrochemistry, photocatalysis, light-induced electron-transfer processes, and the development of photovoltaics. For example, in conjunction with the electron affinity, for the addition of an electron to the lowest-occupied molecular orbital (LUMO), knowledge of the ionization potential, for ionization from the highest-occupied molecular orbital (HOMO), can be used to directly determine the band gap of materials, including quantum dots. The bandgap of a materials, such as quantum dots, is especially relevant for the development of Solar Cells. [114, 47, 58]

As previously mentioned, there are many interesting processes that can occur as a result of light-matter interactions in chemical systems and materials. When modeling many of these processes, the use of time-dependent quantum mechanics is often warranted. These processes, which are typically experimentally observed using spectroscopy, can often involve the absorption of electromagnetic radiation, followed by an electronic transition, and possibly the emission of a photon. Even when considering this seemingly simple process of absorption, followed by electronic transition and possibly photon emission, there are many different possible pathways along which each step can occur. This is one of the reasons why it is particularly challenging to theoretically and computationally simulate the spectra for these aforementioned processes, especially for large chemical systems and materials. It is essential to highlight simulating this example process is relatively simple, when compared to some other light-matter interaction induced processes. For example, the inverse photoemission (IPE) process is particularly challenging to simulate because transitions between unoccupied orbitals play an essential role in the IPE process.

During the process of inverse photoemission an incident electron is captured by a material in a high energy unoccupied states. Next, this captured electron then de-excites to a lower energy unoccupied state, resulting in the emission of a photon. [113] In order to accurately model the IPE process using time-dependent quantum chemical methods, such as time-dependent perturbation theory (TDPT), the effects of electron correlation should be considered. It is known that simply subtracting the energy of the final state (orbital to which the electron de-excites) from the energy of the initial state (orbital in which the electron is captured) does not provide accurate electronic transition energies. Therefore, the transition energy associated with the de-excitation step should be calculated using methodology that accounts for the effects of electron correlation. Many-body perturbation theory and the Frequency-Dependent Geminal-Screened interaction kernel (FD-GSIK) method are examples of methods that can be used to predict correlated transition energies. Using the FD-GSIK method for calculating the correlated transition energies is a particularly effective approach. The main reason for this is because the computational cost of the FD-GSIK method scales linearly with respect to system size. [73] Simulating the inverse photoemission processes in quantum dots can provide valuable information about the unoccupied states of these systems. For example, simulating the IPE process in quantum dots can enable the identification of probable unoccupied-to-unoccupied orbital transitions that can result in the emission of a photon with energy that is less then the bandgap.

By manipulating the environment of a material, it is possible enhance and control light-matter interaction induced processes. For example, light-matter interaction induced processes, such as photoionization and IPE processes, can be enhanced and finely controlled by the application of carefully chosen external electric fields. It is known that the the optical and electronic properties of atoms, molecules, and materials are altered when in the presence of an external electric field. This phenomenon is known as the Stark effect. In many-electron systems, the electronic and

optical properties display a non-linear dependence on the strength of an applied electric field, this effect is often referred to as the nonlinear Stark effect. For quantum confined systems, such as quantum dots, this effect is typically referred to as the quantum-confined Stark effect. [75, 12, 10] By taking advantage of the Stark effect, even complicated light-matter interaction induced processes, such as IPE processes, can be systematically controlled. For example, it has been demonstrated that control of the IPE transition probabilities and emitted photon frequencies can be achieved by the systematic application of carefully chosen Stark fields. It has also been demonstrated that the ionization potentials of PbS quantum dots can be fine-tuned by the application of meticulously selected external static electric fields. Achieving field-dependent control of IPE and photoionization processes is relevant for applications including, but not limited to, the enhancement of electron-transfer reactions, the optimization of photovoltaics, and the development of novel highly controllable photon sources. [117, 47, 106]

Chapter 2

Quantum Chemistry Background

2.1 Scope of Chapter Content

In this chapter the fundamentals of the Hartree-Fock approximation, along with Koopmans' Theorem, for predicting ionization potentials (IPs) and electron affinities (EAs) of many electron systems is presented. Additionally, we briefly introduce the concept of green's functions, at first in a very simple and general mathematical context. Following this mathematical introduction, we introduce the one-particle many-body Green's function in the context of Hartree-Fock theory. In this chapter, we do not discuss the use of Green's function theory in the context of accounting for the effects of electron-correlation and orbital relaxation. A brief overview of the Dyson equation, which enables us to account for the effects of electron-correlation and orbital relaxation, is provided in chapter 5. It would be negligent not to mention that there are many different aspects Green's function theory and its applications in quantum chemistry. This chapter solely presents a foundational introduction to the basics of Green's function theory, in a context that is directly relevant to the material presented in later chapters.

2.2 The Hartree-Fock Method and Koopmans' Theorem

Before introducing the fundamentals of Hartree-Fock theory, the concept of Slater determinants will be introduced. It is well known that it imperative that a many-electron wave function is anti-symmetric with respect to the interchanging of both the spatial and spin coordinates of any two electrons. This means that the wave function must change sign as a result interchanging the spatial and spin coordinates of any two electrons. One simple and well known anti-symmetric wave function is a single Slater determinant. For an N-electron system, the form of the Slater determinant is given as follows. [116]

$$\Psi = \frac{1}{\sqrt{N!}} \begin{vmatrix} \chi_1(1) & \chi_2(1) & \cdots & \chi_N(1) \\ \chi_1(2) & \chi_2(2) & \cdots & \chi_N(2) \\ \chi_1(3) & \chi_2(3) & \cdots & \chi_N(3) \\ \vdots & \vdots & \ddots & \vdots \\ \chi_1(N) & \chi_2(N) & \cdots & \chi_N(N) \end{vmatrix} \quad (2.1)$$

In Equation 2.1, $\frac{1}{\sqrt{N!}}$ ensures normalization. It is imperative to point out that the electrons, $\{(1), (2), \dots (N)\}$, are indexed along the rows of the determinant and the spin orbitals, $\{\chi_1, \chi_2, \dots \chi_N\}$,

are indexed across the columns of the Slater determinant. Since this desired anti-symmetry is an intrinsic property of determinants, the interchange of any two rows of the determinant in [Equation 2.1](#), the sign of Ψ will change. Within the framework of the Hartree-Fock approximation, one can identify a minimal energy single Slater determinant, that best approximates the ground state of an N-electron system. This can be achieved by finding an optimal set of spin orbitals, which results in the minimization of the following energy expression. [\[116\]](#)

$$E_0 = \sum_i^N \langle \chi_i | \hat{h} | \chi_i \rangle + \frac{1}{2} \sum_i^N \sum_j^N \langle \chi_i \chi_j | | \chi_i \chi_j \rangle \quad (2.2)$$

By solving the Hartree-Fock equation, these optimal spin-orbitals can be obtained. The Hartree-Fock equation is a pseudo-eigenvalue equation that is solved iteratively and is defined as follows.

$$\hat{f} \chi_i = \varepsilon_i \chi_i \quad (2.3)$$

In [Equation 2.3](#), \hat{f} is the Fock operator which is given as,

$$\hat{f} = \hat{h} + \sum_j^N (\hat{J}_j - \hat{K}_j) \quad (2.4)$$

where \hat{h} is a one-electron Hamiltonian and is defined as follows.

$$\hat{h} = \frac{1}{2} \nabla_i^2 + \sum_A^M \frac{Z_A}{R_{iA}} \quad (2.5)$$

In [Equation 2.4](#), \hat{J}_j is the Coulomb operator and \hat{K}_j is the exchange operator. The actions of both the Coulomb operator and exchange operator on spin orbital, $\chi_i(1)$, are demonstrated below. [\[116\]](#)

$$\hat{J}_j \chi_i(1) = \langle \chi_j(2) | r_{12}^{-1} | \chi_j(2) \rangle \chi_i(1) \quad (2.6)$$

$$\hat{K}_j \chi_i(1) = \langle \chi_j(2) | r_{12}^{-1} | \chi_i(2) \rangle \chi_j(1) \quad (2.7)$$

One can think of the coulomb and exchange operators as composing a one-electron potential that describes the average potential or "mean-field" experienced by an electron 1 in spin orbital χ_i . Now that we have defined the Fock operator, we can see that the energy (ε_i) of some individual spin orbital, χ_i can be determined from the Hartree-Fock approximation as follows. [\[116\]](#)

$$\varepsilon_i = \langle \chi_i | \hat{f} | \chi_i \rangle = \langle \chi_i | \hat{h} | \chi_i \rangle + \sum_j^N (\langle \chi_i | \hat{J}_j | \chi_i \rangle - \langle \chi_i | \hat{K}_j | \chi_i \rangle) \quad (2.8)$$

Using more compact notation, we express [Equation 2.8](#) as given below.

$$\varepsilon_i = \langle i | \hat{h} | i \rangle + \sum_j^N \langle ij | ij \rangle - \langle ij | ji \rangle \quad (2.9)$$

$$= \langle i | \hat{h} | i \rangle + \sum_j^N \langle ij || ij \rangle \quad (2.10)$$

At this point, it is natural to wonder if any chemically relevant properties can be easily obtained from the Hartree-Fock approximation. Upon solving the Hartree-Fock equation, one can easily obtain a first approximation to the ionization potentials and electron affinities of many-electron chemical systems through the application of Koopmans' Theorem. Since the Koopmans' ionization potential is a quantity that is of direct relevance to the content of this dissertation, we will now demonstrate how ionization potentials can be obtained using Koopmans' theorem. First consider the following expression for the expectation value of the energy for the N-electron single determinant state, within the Hartree-Fock formalism.

$$E_0^N = \sum_i^{N_{\text{occ}}} \langle i | \hat{h} | i \rangle + \frac{1}{2} \sum_i^{N_{\text{occ}}} \sum_j^{N_{\text{occ}}} \langle ij || ij \rangle \quad (2.11)$$

In Equation 2.11, the summations are performed over all occupied orbitals. Next, consider the following expression for the expectation value of the energy for the (N-1)-electron state, which is generated upon the removal of an electron from spin orbital k .

$$E_k^{N-1} = \sum_{i \neq k}^{N_{\text{occ}}} \langle i | \hat{h} | i \rangle + \frac{1}{2} \sum_{i \neq k}^{N_{\text{occ}}} \sum_{j \neq k}^{N_{\text{occ}}} \langle ij || ij \rangle \quad (2.12)$$

The Koopmans' approximation to the ionization potential, for the removal of an electron from spin orbital k , can be obtained by subtracting Equation 2.11 from Equation 2.12.

$$E_k^{N-1} - E_0^N = -\langle k | \hat{h} | k \rangle - \frac{1}{2} \sum_{i, [j=k]} \langle ij || ij \rangle - \frac{1}{2} \sum_{j, [i=k]} \langle ij || ij \rangle \quad (2.13)$$

$$= -\langle k | \hat{h} | k \rangle - \frac{1}{2} \sum_{i, [j=k]} \langle ik || ik \rangle - \frac{1}{2} \sum_{j, [i=k]} \langle kj || kj \rangle \quad (2.14)$$

Upon examination of Equation 2.13, we see that only the following terms remain after performing the subtraction.

$$-\langle k | \hat{h} | k \rangle - \sum_j \langle kj || kj \rangle = -\varepsilon_k \quad (2.15)$$

In Equation 2.15, we see that within the framework of Koopmans' theorem, the ionization potential for the removal of an electron from spin orbital k , is simply the negative of the energy of spin orbital k . By performing a similar deviation it can also be demonstrated that, within the framework of the Koopmans' approximation, the electron affinity for the addition of an electron to spin orbital r is approximated to be equal to $-\varepsilon_r$. [116]

Since the energies of all the spin orbitals are obtained from performing a Hartree-Fock calculation, the Koopmans' approximation provides an extremely convenient route for obtaining first approximations to the ionization potentials of many-electron systems. Note that Koopmans' theorem has been interchanged with Koopmans' approximation throughout this section. The reason for

this is that Koopmans' theorem does not include the effects of electron-correlation and orbital relaxation. One would expect the spin orbitals to change after the removal of an electron. Koopmans' approximation does not account for the changes in the spin orbitals that would realistically occur upon ionization. Therefore, Koopmans' approximation is considered to be a "frozen orbital approximation". [116] There are a variety of approaches to incorporate the effects of electron-correlation and orbital relaxation, in order to more accurately predict ionization potentials and electron affinities of many-electron systems. In this dissertation, we will focus on the use of Green's function theory, particularly the Dyson equation, as a means of obtaining a more accurate estimate of ionization potentials.

2.3 Basic Mathematical Introduction to Green's Function Theory

Consider the following matrix equation and assume that we would like to solve this equation to determine the vector, \mathbf{w} .

$$(E\mathbf{I} - \mathbf{H}_0)\mathbf{w} = \mathbf{u} \quad (2.16)$$

In Equation 2.16, E is a parameter, \mathbf{H}_0 is a $N \times N$ Hermitian matrix, \mathbf{I} is the $N \times N$ identity matrix and \mathbf{u} is a vector. In order to determine the vector, \mathbf{w} , we can utilize the inverse of the matrix, $E\mathbf{I} - \mathbf{H}_0$, as follows.

$$(E\mathbf{I} - \mathbf{H}_0)^{-1}(E\mathbf{I} - \mathbf{H}_0)\mathbf{w} = (E\mathbf{I} - \mathbf{H}_0)^{-1}\mathbf{u} \quad (2.17)$$

By recognizing that $(E\mathbf{I} - \mathbf{H}_0)^{-1}(E\mathbf{I} - \mathbf{H}_0) = \mathbf{I}$ and using $\mathbf{G}_0(E)$ to represent $(E\mathbf{I} - \mathbf{H}_0)^{-1}$, we obtain the following two equations.

$$\mathbf{w} = \mathbf{G}_0(E)\mathbf{u} \quad (2.18)$$

$$\mathbf{w}_i = \sum_j (\mathbf{G}_0(E))_{ij} \mathbf{u}_j \quad (2.19)$$

Upon examination of Equation 2.19, we see that the elements of \mathbf{w} can be obtained for any vector, \mathbf{u} , if $\mathbf{G}_0(E)$ is known. We can reformulate $\mathbf{G}_0(E)$ using the eigenvectors (\mathbf{v}^α) and eigenvalues ($E_\alpha^{(0)}$) of \mathbf{H}_0 .

$$(\mathbf{G}_0(E))_{ij} = \sum_\alpha \frac{v_i^\alpha v_j^{\alpha*}}{E - E_\alpha^{(0)}} \quad (2.20)$$

Upon examination of Equation 2.20, that the poles of $(\mathbf{G}_0(E))_{ij}$ occur at $E = E_\alpha^{(0)}$. [116] Now assume that we would like to solve the inhomogeneous differential equation, shown below, for $a(x)$.

$$(E - H_0)a(x) = b(x) \quad (2.21)$$

In Equation 2.21, E is a parameter and H_0 is a Hermitian differential operator, whose eigenvectors and eigenvalues are $\Psi_\alpha(x)$ and $E_\alpha^{(0)}$, respectively. Assume that $b(x)$ is known. Note that we can expand $a(x)$ and $b(x)$ in terms of the eigenvectors of H_0 .

$$a(x) = \sum_\alpha a_\alpha \Psi_\alpha(x) \quad (2.22)$$

$$b(x) = \sum_{\alpha} b_{\alpha} \Psi_{\alpha}(x) \quad (2.23)$$

Since $b(x)$ is known, we can determine b_{α} by solving the following integral while integrating over all x .

$$b_{\alpha} = \int dx' \Psi_{\alpha}^{*}(x') b(x') \quad (2.24)$$

Once the coefficients, b_{α} , are found we can rewrite Equation 2.21 by incorporating Equation 2.22 and Equation 2.23, along with using the eigenvectors of H_0 , to obtain the following.

$$\sum_{\alpha} a_{\alpha} (E - E_{\alpha}^{(0)}) \Psi_{\alpha}(x) = \sum_{\alpha} b_{\alpha} \Psi_{\alpha}(x) \quad (2.25)$$

Since the $\Psi_{\alpha}(x)$ are form an orthonormal basis, by multiplying both side of Equation 2.25 by $\Psi_{\alpha}^{*}(x)$ and then integrating, we can observe the following relationship between the coefficients, a_{α} and b_{α} .

$$a_{\alpha} (E - E_{\alpha}^{(0)}) = b_{\alpha} \quad (2.26)$$

Next, we can substitute Equation 2.26 into Equation 2.22 in order to obtain the following expression for $a(x)$.

$$a(x) = \sum_{\alpha} \frac{b_{\alpha}}{E - E_{\alpha}^{(0)}} \Psi_{\alpha}(x) \quad (2.27)$$

Now we can substitute Equation 2.24 for b_{α} in Equation 2.27, to obtain the following integral equation.

$$a(x) = \sum_{\alpha} \int dx' \frac{\Psi_{\alpha}(x) \Psi_{\alpha}^{*}(x')}{E - E_{\alpha}^{(0)}} b(x') \quad (2.28)$$

By defining the following Green's function,

$$G_0(x, x', E) = \sum_{\alpha} \frac{\Psi_{\alpha}(x) \Psi_{\alpha}^{*}(x')}{E - E_{\alpha}^{(0)}} \quad (2.29)$$

we can rewrite our expression for $a(x)$ as follows.

$$a(x) = \int dx' G_0(x, x', E) b(x') \quad (2.30)$$

By working through this process, we have successfully reduced the equation of interest (Equation 2.21) from an inhomogeneous differential equation to an integration problem. Upon examination of Equation 2.30, we see that the poles of $G_0(x, x', E)$ occur at $E = E_{\alpha}^{(0)}$. [116]

2.4 One-Particle MBGF: Hartree-Fock Green's Function

In this section, we will use results obtained from the previous section, in order to work our way towards the definition of the Hartree-Fock Green's function (HFGF), in an efficient manner. Consider the Hartree-Fock Hamiltonian which is given as,

$$H_0 = \sum_i f_i \quad (2.31)$$

where f_i is the Fock operator for electron i . An optimal set of orthonormal spin orbitals (χ_i) and orbital energies (ε_i), for a N-electron system, can be determined by solving the Hartree-Fock equation, as discussed in the section 2.2. Using Equation 2.29, which was obtained in the previous section, we can intuitively construct an analogous Green's function, $G_0(\mathbf{x}, \mathbf{x}', E)$, which is defined below. [116]

$$G_0(\mathbf{x}, \mathbf{x}', E) = \sum_a \frac{\chi_a(\mathbf{x})\chi_a^*(\mathbf{x}')}{E - \varepsilon_a} + \sum_r \frac{\chi_r(\mathbf{x})\chi_r^*(\mathbf{x}')}{E - \varepsilon_r} \quad (2.32)$$

Note that in Equation 2.32, we are summing over both the occupied spin orbitals and the virtual spin orbitals, which are indexed by a and r , respectively. By using Equation 2.32, along with the results obtained in the previous section, we can define the elements of $\mathbf{G}_0(\mathbf{x}, \mathbf{x}', E)$, in its matrix form as follows.

$$(\mathbf{G}_0(E))_{ij} = \int \int d\mathbf{x}d\mathbf{x}' \chi_i^*(\mathbf{x})\mathbf{G}_0(\mathbf{x}, \mathbf{x}', E)\chi_j(\mathbf{x}') = \frac{\delta_{ij}}{E - \varepsilon_i} \quad (2.33)$$

Analogous to the representation of $\mathbf{G}_0(E)$ used in the previous section, we can write the following matrix equation for $\mathbf{G}_0(E)$ in the context of Hartree-Fock theory.

$$\mathbf{G}_0(E) = (E\mathbf{I} - \boldsymbol{\varepsilon})^{-1} \quad (2.34)$$

In Equation 2.34, $\boldsymbol{\varepsilon}$ is a diagonal matrix whose elements are the Hartree-Fock spin orbital energies. It is particularly relevant to highlight the connection between Equation 2.34 and Koopmans' theorem, which was discussed in section 2.2. Koopmans' theorem states that the ionization potential, for the removal of an electron from an occupied orbital, χ_i , is defined as follows.

$$E_{\text{IP}}^{\text{Koopmans}} = -\varepsilon_i \quad (2.35)$$

Given the above definition, it can be seen that the Koopmans' approximation to the ionization potential can be recovered from Equation 2.33. Furthermore, upon examination of Equation 2.34, it can be observed that the poles of $\mathbf{G}_0(E)$ occur at values of E such that,

$$\det(E\mathbf{I} - \boldsymbol{\varepsilon}) = 0 \quad (2.36)$$

where $\det(E\mathbf{I} - \boldsymbol{\varepsilon})$ denotes the determinant of $E\mathbf{I} - \boldsymbol{\varepsilon}$. Therefore, the poles of $\mathbf{G}_0(E)$ occur when E is equal to Hartree-Fock orbital energies. [116] In order to prepare for the introduction of the SSE-MO method, which is the main topic of this dissertation, a pedagogical introduction to Monte Carlo integration and some select variance reduction techniques is provided in the next chapter.

Chapter 3

Background: Monte Carlo Integration

3.1 Basics of Naive Monte Carlo integration

Monte Carlo integration is a stochastic numerical integration technique that utilizes "random" sampling techniques to estimate the solution to an integral. Various techniques, which are known as variance reduction techniques, can be used to improve the efficiency and the accuracy with which the integral is computed. It is relevant to mention that for numerical integration in low dimensional spaces, such as 1D or 2D space, quadrature is a more efficient choice than Monte Carlo integration. However, for numerical integration in spaces of higher dimensions, Monte Carlo integration is the more efficient choice. As opposed to quadrature methods for which the convergence rate becomes exponentially slower as dimensionality increases, the convergence rate for Monte Carlo integration is independent of dimensionality. [54]

For the purpose of introducing the topic of Monte Carlo integration, the basics of naive Monte Carlo integration in one-dimension will be presented in this section. The naive Monte Carlo integration approach does not involve the employment of variance reduction techniques. Consider a one-dimensional integral of a continuous function, $f(x)$, on $[a, b]$.

$$I_1 = \int_a^b dx f(x) \quad (3.1)$$

Assume that we do not know how to solve I_1 analytically, but we know the functional form of $f(x)$ and can evaluate this function at values of x on $[a, b]$. Before we can estimate I_1 , we must first establish the sample space from which we can choose values of x . We define a set of N values of x , such that $a \leq x_i \leq b$ as follows.

$$X = \{x_1, x_2, x_3, \dots, x_{N-1}, x_N\} \quad (3.2)$$

This set X is our sample space from which we will randomly draw M number of values of x . We index the samples randomly chosen from X as x_i , where $i = 1, 2, 3, \dots, M$. Since we know the value of $f(x)$ for all $x \in X$, we can determine the corresponding value of $f(x)$ for each x_i randomly sampled and estimate the expectation value of $f(x)$. We denote the expectation value of $f(x)$ as $\mathbb{E}[f]$ and it is defined as follows.

$$\mathbb{E}[f] = \langle f \rangle = \frac{1}{M} \sum_{i=1}^M f(x_i) \quad (3.3)$$

In order to obtain an estimate of I_1 we multiply $\mathbb{E}[f]$ by the volume of the sample space, which for this one-dimensional example, is defined as $V = b - a$.

$$I_1 \approx J_M = V \times \mathbb{E}[f] \quad (3.4)$$

It is important to note that in [Equation 3.3](#), $\mathbb{E}[f]$ is an estimate of the mean of $f(x)$ obtained from a finite number of samples. As we increase the number of samples our estimate of the mean of $f(x)$ becomes more accurate. We define the exact mean of $f(x)$ as follows.

$$\mu_f = \lim_{M \rightarrow \infty} \frac{1}{M} \sum_{i=1}^M f(x_i) \quad (3.5)$$

If we were to sample $f(x)$ for an infinite number of x_i we would obtain the exact mean of this function of interest. In practice it is not possible for us to choose an infinite number of samples, but by estimating the variance of $f(x)$ we can determine the error in our estimate of I_1 . We can estimate in variance of $f(x)$ as follows. [\[54\]](#)

$$\mathbb{V}[f] = \frac{1}{M} \sum_{i=1}^M [f(x_i) - \langle f \rangle]^2 = \frac{1}{M} \sum_{i=1}^M f(x_i)^2 - \langle f \rangle^2 \quad (3.6)$$

Since our all possible samples of x_i are uncorrelated and have identical variance, we can estimate the variance of $\mathbb{E}[f]$ as follows. [\[6\]](#)

$$\mathbb{V}[\mathbb{E}[f]] = \mathbb{V}\left[\frac{1}{M} \sum_{i=1}^M f(x_i)\right] = \frac{1}{M^2} \sum_{i=1}^M \mathbb{V}[f(x_i)] = M \times \frac{1}{M^2} \mathbb{V}[f] = \frac{1}{M} \mathbb{V}[f] \quad (3.7)$$

By taking the square root of [Equation 3.7](#) we can determine the error in $\mathbb{E}[f]$, which is our estimate of our estimate of μ_f .

$$Z = \sqrt{\frac{1}{M} \mathbb{V}[f]} \quad (3.8)$$

Upon examination of [Equation 3.8](#), we see that the error in $\mathbb{E}[f]$ decreases with respect to the number of samples, M . The error in $\mathbb{E}[f]$ and therefore, the error in our estimate of I_1 is proportional to the number samples.

$$Z \propto \frac{1}{\sqrt{M}} \quad (3.9)$$

Therefore, by increasing the number of samples we can reduce the error in our estimate of I_1 . [\[54, 6\]](#)

3.2 Monte Carlo Numerical in Higher Dimensions

In this section, a brief description of Monte Carlo integration in higher dimensions is provided. Consider the following integral of a k -dimensional function, $f(\mathbf{x})$.

$$I_2 = \int_{\Lambda} d\mathbf{x} f(\mathbf{x}) \quad (3.10)$$

Assume that we cannot solve I_2 analytically and that we know the form of $f(\mathbf{x})$. In Equation 3.10, \mathbf{x} is a k -dimensional vector and Λ represents the bounds of integration. The volume of space in which the integration is performed is given as follows.

$$V = \int_{\Lambda} d\mathbf{x} \quad (3.11)$$

We define our sample spaces as follows.

$$\Lambda = \{\mathbf{x}_1, \mathbf{x}_2, \mathbf{x}_3, \dots, \mathbf{x}_{N-1}, \mathbf{x}_N\} \quad (3.12)$$

Next, we define the expectation value of $f(\mathbf{x})$, which is a finite estimate of the exact mean of $f(\mathbf{x})$.

$$\mathbb{E}[f] = \langle f \rangle = \frac{1}{M} \sum_{i=1}^M f(\mathbf{x}^i) \quad (3.13)$$

In Equation 3.13, \mathbf{x}^i are sampled from Λ and M is the number of samples chosen. Now we can define our approximation of I_2 as given below in Equation 3.14.

$$I_2 \approx G_M = V \times \mathbb{E}[f] \quad (3.14)$$

Similar to the one-dimensional example in the previous section, the variance of $\mathbb{E}[f]$ can be estimated as follows.

$$\mathbb{V}[f] = \frac{1}{M} \sum_{i=1}^M [f(\mathbf{x}^i) - \langle f \rangle]^2 = \frac{1}{M} \sum_{i=1}^M f(\mathbf{x}^i)^2 - \langle f \rangle^2 \quad (3.15)$$

Since we are assuming that the sampling process produces uncorrelated samples and that all possible samples of \mathbf{x}^i have identical variance, the error in our estimate of $\mathbb{E}[f]$ can be calculated as,

$$Z = \sqrt{\frac{1}{M} \mathbb{V}[f]} \quad (3.16)$$

therefore, we again observe the following relationship between the number of samples, M , and the error in our estimate of $\mathbb{E}[f]$. [54, 6]

$$Z \propto \frac{1}{\sqrt{M}} \quad (3.17)$$

Although we are integrating over some k -dimensional space, where k can be arbitrarily large, the error in our estimate of I_2 still displays the same scaling with respect to the number of samples as we observed for the one-dimensional example. [54] Although this particular property generally makes Monte Carlo integration the best choice for doing numerical integration in higher dimensions, in practice variance reduction techniques, such as stratified sampling, control variate, and common random number sampling, are typically employed. Variance reduction techniques, when employed properly, enable a greater reduction in error more efficiently than can be achieved using naive Monte Carlo integration. The remainder of this chapter will be devoted to discussing various variance reduction techniques.

3.3 Stratified Sampling

Stratified sampling is a variance reduction technique that utilizes informed sampling. First, the integration domain is divided into non-overlapping segments. Then sample points are strategically allocated such that more sampling points are allocated to segments that display greater variance compared to segments that display lower variance. When the number of sampling points in each segment is directly proportional to the variance in each segment a significant reduction in the error in the estimate of an integral of interest can be achieved. [54, 6, 98] For the purpose of briefly introducing stratified sampling in the context of Monte Carlo numerical integration, we will continue with our k-dimensional example from the previous section. Again, suppose we want to solve the following k-dimensional integral and that we do not know the analytical solution, but we do know the form of $f(\mathbf{x})$.

$$I_2 = \int_{\Lambda} d\mathbf{x} f(\mathbf{x}) \quad (3.18)$$

The total volume of space in which the integration is performed is given as,

$$V = \int_{\Lambda} d\mathbf{x} \quad (3.19)$$

and our total sample space is defined as follows.

$$\Lambda = \{\mathbf{x}_1, \mathbf{x}_2, \mathbf{x}_3, \dots, \mathbf{x}_{N-1}, \mathbf{x}_N\} \quad (3.20)$$

Instead of sampling directly from Λ , we will divide this total sample space into a set of N_{seg} non-overlapping regions with identical volumes such that,

$$\Lambda_{\text{space}} = \sum_{J=1}^{N_{\text{seg}}} \Lambda_J \quad (3.21)$$

and the volume of each region is related to the total volume over which the integration is performed is given as follows.

$$V_{\text{space}} = \sum_{J=1}^{N_{\text{seg}}} V_{\text{seg}}^J = V_{\text{seg}}^J \times N_{\text{seg}} \quad (3.22)$$

The expectation value of $f(\mathbf{x})$, in segment Λ_J (denoted as J) of the sample space is given as follows.

$$\mathbb{E}[f_J] = \langle f_J \rangle = \frac{1}{M_J} \sum_{i=1, i \in J}^{M_J} f(\mathbf{x}^i) \quad (3.23)$$

In order to determine the expectation value of $f(\mathbf{x})$ over the entire sample space, we can calculate the average of the expectation values of $f(\mathbf{x})$ over all of the segments of the sample space.

$$\mathbb{E}[f] = \langle f \rangle = \frac{1}{N_{\text{seg}}} \sum_{J=1}^{N_{\text{seg}}} \mathbb{E}[f_J] \quad (3.24)$$

The variance in the expectation value of $f(\mathbf{x})$ in segment J can be determined as follows.

$$\mathbb{V}[f_J] = \frac{1}{M_J} \sum_{i=1, i \in J}^{M_J} [f(\mathbf{x}^i) - \langle f_J \rangle]^2 = \frac{1}{M_J} \sum_{i=1, i \in J}^{M_J} f(\mathbf{x}^i)^2 - \langle f_J \rangle^2 \quad (3.25)$$

For this example, the sampling in any given segment is uncorrelated with respect to the sampling in all other segments. Therefore, we do not need to consider the covariance between the random variables sampled from different segments. As a result, the total variance in $\mathbb{E}[f]$ is given as follows. [6]

$$\mathbb{V}[f] = \mathbb{V}\left[\frac{1}{N_{\text{seg}}} \sum_{J=1}^{N_{\text{seg}}} \mathbb{E}[f_J]\right] = \frac{1}{N_{\text{seg}}^2} \sum_{J=1}^{N_{\text{seg}}} \mathbb{V}[\mathbb{E}[f_J]] \quad (3.26)$$

In Equation 3.26, it can be observed that the variance in our estimate of $\mathbb{E}[f]$, and consequently the error in our estimate, decreases as the number of segments into which the sample space is divided increases. Additionally, we see that the total variance in $\mathbb{E}[f]$ depends on the sum of the variances for each segment. Therefore, in order to significantly reduce the error in our estimate of $\mathbb{E}[f]$, the variance in each segment should be minimized. A reasonable strategy for minimizing the variance in each segment is to distribute the sampling points so that the number of sampling points for a given segment is directly proportional to the variance observed for that given segment. [6]

$$M_J \propto \mathbb{V}[f_J] \quad (3.27)$$

Finally, an estimate of I_2 , using stratified sampling can be obtained as demonstrated below.

$$I_2 \approx G_M = \frac{1}{N_{\text{seg}}} \sum_{J=1}^{N_{\text{seg}}} V_{\text{seg}}^J \times \mathbb{E}[f_J] \quad (3.28)$$

Compared to naive Monte Carlo, the use of stratified sampling enables significant variance reduction due to the strategic allocation sampling points according to the variance observed in regions of the total sample space. [6, 98] Another variance reduction technique, the control variate technique, will be introduced in the next section.

3.4 Control Variate Technique with Common Random Number Sampling

In this section a brief introduction to the control variate technique is provided. First consider the difference between two random variables, X and Y .

$$Z = X - Y \quad (3.29)$$

In order to achieve variance reduction, the control variate technique leverages the following property of the variance of differences between the two random variables. [54, 6]

$$\mathbb{V}[Z] = \mathbb{V}[X] + \mathbb{V}[Y] - \text{Cov}[X, Y] \quad (3.30)$$

In the above equation, $\mathbb{V}[X]$ and $\mathbb{V}[Y]$ are the variances of the random variables, X and Y , respectively. The covariance of X and Y is denoted as $\text{Cov}[X, Y]$. Upon examination of [Equation 3.30](#), it can be observed that if the covariance of X and Y is positive ($\text{Cov}[X, Y] > 0$), then $\mathbb{V}[Z] < \mathbb{V}[X] + \mathbb{V}[Y]$. The utility of this particular property will become apparent as the details of the control variate technique is presented. [\[54, 6\]](#)

In order to illustrate the fundamentals of the control variate technique, we will again use the previous example from section 2.2, of the integral of some k -dimensional function, $f(\mathbf{x})$, with bounds defined by Λ . Suppose we are able to find some k -dimensional function, $g(\mathbf{x})$, such that the analytical solution of the integral of $g(\mathbf{x})$ over Λ is known.

$$I_g = \int_{\Lambda} d\mathbf{x} g(\mathbf{x}) \quad (3.31)$$

Using [Equation 3.31](#), we can construct the following.

$$h(\mathbf{x}) = f(\mathbf{x}) - cg(\mathbf{x}) + cI_g \quad (3.32)$$

In [Equation 3.32](#), $g(\mathbf{x})$ is our control variate function, I_g is defined in [Equation 3.31](#), and c is an optimization coefficient that can be chosen to minimize the variance in our estimate of the expectation value of $h(\mathbf{x})$. We define our estimate in the expectation value of $h(\mathbf{x})$ as given below.

$$\mathbb{E}[h] = \langle h \rangle = \frac{1}{M} \sum_{i=1}^M (f(\mathbf{x}^i) - cg(\mathbf{x}^i)) + cI_g \quad (3.33)$$

Here \mathbf{x}^i are sampled from Λ , which is the sample space defined in [Equation 3.12](#), and M is the number of samples chosen. It is imperative to note, that when sampling, only one \mathbf{x}^i is chosen each time a sample is drawn from the sample space, and both $f(\mathbf{x})$ and $g(\mathbf{x})$ are evaluated at that same \mathbf{x}^i , for any single term contributing to the summation in [Equation 3.33](#). This sampling technique is referred to as common random number sampling and the purpose of employing this sampling technique, in conjunction with the control variate technique, will become clear by the end of this section. [\[54\]](#) It is also relevant to highlight that I_g is a known quantity and does not depend on the random variable, \mathbf{x}^i .

Using [Equation 3.33](#), we can estimate the solution to the integral of $f(\mathbf{x})$ as follows.

$$I_2 = \int_{\Lambda} d\mathbf{x} f(\mathbf{x}) \approx \left[V \times \frac{1}{M} \sum_{i=1}^M (f(\mathbf{x}^i) - cg(\mathbf{x}^i)) \right] + cI_g \quad (3.34)$$

In the above equation, V is defined in [Equation 3.11](#) and it is imperative to highlight that the integral of the following difference term,

$$d(\mathbf{x}) = f(\mathbf{x}) - cg(\mathbf{x}) \quad (3.35)$$

is calculated numerically using Monte Carlo integration, while cI_g is known exactly. In order to determine the error in our estimate of the integral of $f(\mathbf{x})$, we must calculate the variance in our estimate of $\mathbb{E}[h]$.

$$\mathbb{V}[\mathbb{E}[h]] = \frac{1}{M} (\mathbb{V}[f] + c^2 \mathbb{V}[g] - 2c \text{Cov}[f, g]) \quad (3.36)$$

In Equation 3.36, $\mathbb{V}[f]$ and $\mathbb{V}[g]$ are the variances in $f(\mathbf{x})$ and $g(\mathbf{x})$, respectively. The covariance of $f(\mathbf{x})$ and $g(\mathbf{x})$ is denoted as $\text{Cov}[f, g]$ and is defined as follows.

$$\text{Cov}[f, g] = \mathbb{E}[(f(\mathbf{x}) - \mathbb{E}[f(\mathbf{x})])(g(\mathbf{x}) - \mathbb{E}[g(\mathbf{x})])] = \mathbb{E}[f(\mathbf{x})g(\mathbf{x})] - \mathbb{E}[f(\mathbf{x})]\mathbb{E}[g(\mathbf{x})] \quad (3.37)$$

The covariance provides a metric of the joint variability of $f(\mathbf{x})$ and $g(\mathbf{x})$. For example, if the values of $f(\mathbf{x})$ and $g(\mathbf{x})$ are very similar for most of the \mathbf{x}^i sampled from Λ , then $f(\mathbf{x})$ and $g(\mathbf{x})$ are positively correlated and $\text{Cov}[f, g]$ will be positive. Conversely, if the value of $f(\mathbf{x})$ is very large at values of \mathbf{x}^i for which the value of $g(\mathbf{x})$ is very small, then $f(\mathbf{x})$ and $g(\mathbf{x})$ are negatively correlated and $\text{Cov}[f, g]$ will be negative. If $f(\mathbf{x})$ and $g(\mathbf{x})$ are either strongly positively correlated or strongly negatively correlated, significant variance reduction can be achieved. [98] If $f(\mathbf{x})$ and $g(\mathbf{x})$ are negatively correlated the expression in Equation 3.32 can be modified as follows.

$$h(\mathbf{x}) = f(\mathbf{x}) + cg(\mathbf{x}) - cI_g \quad (3.38)$$

It is worth pointing out, that with the exception of Equation 3.38, we have been assuming that $f(\mathbf{x})$ and $g(\mathbf{x})$ are positively correlated. Now we will briefly discuss how the optimal coefficient, c , can be determined in order to minimize that variance in our estimate of $\mathbb{E}[h]$, as given in Equation 3.36. The variance in $h(\mathbf{x})$ is defined as

$$\mathbb{V}[h] = \mathbb{V}[f] + c^2\mathbb{V}[g] - 2c\text{Cov}[f, g] \quad (3.39)$$

and by taking the first derivative of Equation 3.39, with respect to c , we obtain the following.

$$\frac{d}{dc}\mathbb{V}[h] = 2c\mathbb{V}[g] - 2\text{Cov}[f, g] \quad (3.40)$$

By setting the expression in Equation 3.40 equal to zero and rearranging, we find the following expression for the optimal choice of c .

$$c = \frac{\text{Cov}[f, g]}{\mathbb{V}[g]} \quad (3.41)$$

By substituting Equation 3.41 into Equation 3.39 and rearranging we obtain the following.

$$\mathbb{V}[h] = \mathbb{V}[f] - \frac{(\text{Cov}[f, g])^2}{\mathbb{V}[g]} = \mathbb{V}[f] \left(1 - \frac{(\text{Cov}[f, g])^2}{\mathbb{V}[f]\mathbb{V}[g]} \right) \quad (3.42)$$

Upon examination of Equation 3.42, it can be observed that

$$\frac{(\text{Cov}[f, g])^2}{\mathbb{V}[f]\mathbb{V}[g]} = \rho_{f,g}^2 \quad (3.43)$$

, where $\rho_{f,g}^2$ is the Pearson correlation coefficient. The substitution of Equation 3.43 into Equation 3.42 yields the following.

$$\mathbb{V}[h] = \mathbb{V}[f] \left(1 - \rho_{f,g}^2 \right) \quad (3.44)$$

It can be observed that if $\rho_{f,g}^2 > 0$ the error in our estimate of the integral of $f(\mathbf{x})$, using the control variate technique, will be less than the error in our estimate of this integral obtained from naive Monte Carlo integration. [98]

3.5 Ratio estimator with Common Random Number Sampling

Common random number (CRN) sampling, which is also known as correlated sampling, enhances variance reduction by introducing correlation between random variables. to reduce sampling error. [11] Here, we briefly provide a simple one-dimensional example of how CRN sampling can be applied for ratio estimation, in order to highlight its utility for achieving variance reduction. Consider the following ratio estimator, R , of two one-dimensional functions $f(x)$ and $g(x)$.

$$R = \frac{\langle f(x) \rangle}{\langle g(x) \rangle} = \frac{\sum_i f(x_i)}{\sum_i g(x_i)} \quad (3.45)$$

Notice that although the quantities in the numerator and denominator are averages, the number By adding and subtracting 1 one to the Equation 3.45, we obtain the following.

$$R = 1 + \left[\frac{\sum_i f(x_i)}{\sum_i g(x_i)} - 1 \right] \quad (3.46)$$

$$R = 1 + \frac{\sum_i [f(x_i) - g(x_i)]}{\sum_i g(x_i)} \quad (3.47)$$

By substituting of $X = f(x_i)$ and $Y = g(x_i)$ (Equation 3.29), we see that if $f(x)$ and $g(x)$ are positively correlated, then the variance in the ratio, R , can be reduced using CRN sampling.

$$R = 1 + \frac{\sum_i [f(x_i^{\text{CRN}}) - g(x_i^{\text{CRN}})]}{\sum_i g(x_i^{\text{CRN}})} \quad \text{for } \text{Cov}[f, g] \geq 0 \quad (3.48)$$

Conversely, if $f(x)$ and $g(x)$ are negatively correlated, we can achieve variance reduction simply by implementing a sign switch.

$$R = -1 + \frac{\sum_i [f(x_i^{\text{CRN}}) + g(x_i^{\text{CRN}})]}{\sum_i g(x_i^{\text{CRN}})} \quad \text{for } \text{Cov}[f, g] < 0 \quad (3.49)$$

Common random number (CRN) sampling is a powerful sampling technique that can be used in concert with other a variety of variance reduction techniques, such as the ratio-estimator and control-variate techniques. More information on common random number sampling can be found in Ref [11].

Chapter 4

Introduction to Summation by Stochastic Enumeration and Stratified Stochastic Enumeration

4.1 Stochastic Enumeration for Computing Sums

In this section, an introduction to summation by stochastic enumeration is provided. Consider the sum below in [Equation 4.1](#). Assume that the computation of f_{sum} , requires the evaluation and summation of an intractable number of terms (f_i). Also, assume that the evaluation of each f_i is non-trivial, such as it is for the scenario in which the f_i are multi-dimensional integrals that must be computed numerically.

$$f_{\text{sum}} = \sum_{i=1}^{10^{10}} f_i \approx 10^{10} \times \frac{1}{N_{\text{sample}}} \sum_{i \in \Omega}^{N_{\text{sample}}} f_i \quad (4.1)$$

Note that on the left-hand side (LHS) of [Equation 4.1](#), a sequential summation is performed. This means that every single term (f_i) is evaluated using equivalent computational effort and then summed. For an extremely large number of f_i , computing f_{sum} by way of sequential summation becomes computationally intractable, especially if evaluating each f_i is non-trivial and requires significant computational effort, in and of itself. Here we use the integer index, i , to index the terms composing the summation. Now, notice that on the right-hand side (RHS) of [Equation 4.1](#), f_{sum} is computed using stochastic enumeration. Here a subset of the integer indices, i , which can be thought of as a unique identifier for each term in the sum, is randomly sampled from the sample space, Ω . The number of i sampled from Ω is denoted as N_{sample} . Note that Ω does contain all of the indices or unique identifiers for all of the terms in the summation, but when using stochastic enumeration not all of the terms are included in the sum. More formally, $N_{\text{sample}} < N_{\text{max}}$, where the total number of terms composing f_{sum} is denoted as N_{max} . Notice that on the RHS of [Equation 4.1](#) the result obtained from the stochastic sum is divided by N_{sample} . Therefore, in order to estimate f_{sum} , instead of just computing the average value of the f_i , we multiply by the total number of terms that compose the complete sum, as given on the LHS of [Equation 4.1](#). Clearly, this approach of stochastic enumeration is extremely efficient, but it is also clear that the accuracy in the result obtained for our estimate of f_{sum} may not be up to par.

4.2 Stratified Stochastic Enumeration for Computing Sums

In order to obtain a more accurate estimate of f_{sum} , we can combine stochastic enumeration with stratified sampling. We refer to this combination technique as stratified stochastic enumeration (SSE). In order to introduce stratified sampling, we first divide our sample space, Ω , into M non-overlapping subspaces or "segments".

$$\Omega^{f_i, M} \cap \Omega^{f_i, M'} = \emptyset \quad \text{for } M \neq M' \quad (4.2)$$

In Equation 4.2, we formally express the condition that the segments, into which the sample space is divided, must not overlap. Once Ω is divided into M non-overlapping segments, we can perform sampling within each segment, such that the sampling within segment M is completely uncorrelated from the sampling process within all other segments. Next, the average value of f_i in segment M is determined and then subsequently multiplied by the maximum number of terms that could possibly be sampled from segment M . Performing this process for each segment allows us to obtain an estimate of the contribution of each segment to the overall sum (f_{sum}). These contributions from each segment are then summed in order to obtain an estimate of f_{sum} . This process is formally defined in Equation 4.3.

$$f_{\text{sum}} = \sum_{i=1}^{10^{10}} f_i \approx \sum_{M=1}^{N_{\text{seg}}} \frac{N_{\text{max}}^M}{N_{\text{sample}}^M} \sum_{i \in \Omega_M}^{N_{\text{sample}}^M} f_{i_M} \quad (4.3)$$

In Equation 4.3, N_{sample}^M indicates the number of terms sampled from segment M and N_{max}^M is the maximum number of terms that could possibly be sampled from segment M . As hinted at earlier, the incorporation of stratified sampling can be used to improve upon the accuracy achieved when using only stochastic enumeration to estimate a sum. The stratification of the sample space enables us to distribute our sampling effort in an efficient and informed manner. For example, if we notice that the variance and average value of f_{i_M} is greater in segment $M = 2$, relative to all of the other segments, then more sampling effort can be allocated to segment $M = 2$ compared to the sampling effort used for sampling within the rest of the segments. In essence, the number of samples drawn from segment M , is proportional to the variance and average value of f_{i_M} in segment M .

$$N_{\text{sample}}^M \propto \mathbb{V}[f_{i_M}] \quad (4.4)$$

$$N_{\text{sample}}^M \propto \frac{1}{N_{\text{sample}}^M} \sum_{i \in \Omega_M}^{N_{\text{sample}}^M} f_{i_M} \quad (4.5)$$

Due to the incorporation of stratified sampling, not only is this approach very efficient, but it also enables reduction of the error in our estimate of f_{sum} . Greater detail about stratified sampling, and its utility as a variance reduction technique, can be found section 3.3 of the previous chapter.

Chapter 5

Stratified Stochastic Enumeration of Molecular Orbitals method: Applied for Investigation of Ionization Potential in Quantum Dots

5.1 Scope of Chapter Content

This chapter presents the theoretical details of the Stratified Stochastic Enumeration of Molecular Orbitals (SSE-MO) method, in the context of its application for constructing the frequency-dependent self-energy operator. Here, we demonstrate that the SSE-MO method can be applied for the purpose of efficiently and accurately calculating ionization potentials, by constructing the diagonal second-order frequency-dependent self-energy operator and then subsequently, solving the associated Dyson equation. The SSE-MO method was used to calculate the ionization potential, for ionization from the highest-occupied molecular orbital, for PbS and CdS clusters and quantum dots using both single-shot and iterative procedures for solving the Dyson equation. Furthermore, the frequency-dependent spectral functions were constructed for the PbS and CdS systems. The ionization potentials of quantum dots provide critical information about the energies of occupied states, which can then be used to quantify the electron-removal characteristics of quantum dots. In particular, the energy of the highest-occupied molecular orbital (HOMO) is used to understand electron-transfer processes by investigating the energy-level alignment between quantum dots and electron-accepting ligands. [114]

The accurate first-principles calculation of ionization potentials continues to be challenging due to the computational cost associated with the construction of the frequency-dependent self-energy operator and the numerical solution of the associated Dyson equation. The computational cost becomes prohibitive as the system size increases because of the large number of 2particle-1hole (2p1h) and 1particle-2hole (1p2h) terms that must be computed. The SSE-MO method is a real-space method and the central strategy of this method is to use stochastically enumerated sampling of molecular orbitals and molecular-orbital indices for the construction of the 2p1h and 1p2h terms of the self-energy operator. This is achieved by first creating a composite MO-index Cartesian coordinate space, followed by transformation of the frequency-dependent self-energy operator to this composite space. The evaluation of both the real and imaginary components of the self-energy operator was performed using a stratified Monte Carlo technique. [114]

5.2 Introduction

Ionization potential (IP) ω (or ionization energy) is defined as the energy needed to remove an electron from a chemical system.



$$\omega_{\text{IP}} = E^{N-1} - E^N \quad (5.2)$$

The ejection of the electron can be facilitated using incident photons, scattering by high-energy electrons, or applying a strong electric field. As one of the fundamental properties of a material, IP has relevance to the areas of photovoltaics, mass spectroscopy, photoelectron spectroscopy, electrochemistry, photocatalysis, and light-induced electron-transfer processes. The IP of atoms, molecules, and various chemical compounds is a quantity of interest when performing X-ray spectroscopy. Recently, it has been found that small gas-phase polyatomic molecules with a heavy atom, such as iodomethane, bombarded with hard X-ray pulses display surprisingly enhanced ionization relative to an individual heavy atom with the same absorption cross-section.[100] Following the excitation of an electron from an inner orbital of one atom, another electron from a higher energy orbital of the same atom can occupy this inner orbital. Instead of undergoing de-excitation, the newly excited electron can transfer energy via photon emission by ionizing an electron from an outer orbital of a neighboring atom. This process is called interatomic Coulombic decay (ICD).[49, 3] The IP of both inner and outer orbitals of molecules, dimers, and clusters influences which de-excitation mechanism occurs in a highly excited neutral or a highly excited ionized state of these types of systems. Knowledge of the IP of these systems' inner and outer orbitals can assist in the prediction of which de-excitation mechanism is likely to occur in a system of interest.[72, 102, 51, 4, 79, 18] High-precision IP in atoms and molecules provides important information about electron-electron correlation and serves as a benchmark for development and testing of theories. Ionization potential also is a quantity of interest in biological systems. For example, ionizing radiation causes permanent heritable DNA damage, [120] and the IP of nucleic acid tautomers are quantities of interest, due to the role of these molecules in cancer. [112]

In quantum dots (QDs) and nanomaterials, knowledge of IP from the highest-occupied molecular orbital (HOMO) serves as an important metric for quantifying electron-transfer rates.[19, 57, 117, 130, 24, 103, 56] Photo-ejection of electrons by X-ray and UV radiations has been used to study valence-band states in QDs [89]. The combined information from X-ray and fluorescence spectroscopy has been used to calculate the exciton binding energies in CdSe QDs. Cyclic voltammetry has also been used to calculate HOMO energies in QDs and IPs.[26] Transient photo-emission in two-photon experiments has provided information on the energy levels of unoccupied energy levels.[32] Knowledge of the relative position of the HOMO and lowest unoccupied molecular orbital (LUMO) levels of a QD with respect to the surface ligands is an important factor in extraction of a hot carrier from the QD. [89]

In molecular quantum chemistry, the simplest approximation of IP (denoted as ω_i^0) is given by the Koopmans' approximation, where the exact IP is approximated as the negative of the orbital energies.

$$\omega_p^0 = -\epsilon_p = \langle \Phi_{\text{HF}}^N | \hat{p}^\dagger H \hat{p} | \Phi_{\text{HF}}^N \rangle - \langle \Phi_{\text{HF}}^N | H | \Phi_{\text{HF}}^N \rangle \quad \text{for } \chi_p \in \Phi_{\text{HF}}^N \quad (5.3)$$

Koopmans' treatment utilizes the Hartree-Fock (HF) approximation to obtain a single N-electron Slater determinant from which an electron from one of the occupied states is annihilated as

shown in Equation 5.3. Although Koopmans’ theorem is limited by the use of single Slater determinants and does not account for orbital relaxation and electron-electron correlation effects, it still provides an acceptable first approximation for the IP of a system of interest.[116] Going beyond Koopmans’ approximation by including electron-electron correlation effect can be achieved in a variety of different ways such as with electron-propagator methods,[23, 27, 30][110, 43, 42, 38, 20, 111] algebraic diagrammatic construction (ADC),[104, 17] equation-of-motion coupled-cluster (IP-EOM-CCSD),[83, 82, 95, 55, 45, 91] many-body perturbation theory (MBPT) [86, 46], GW method,[39] correlated-orbital theory (COT)[5], and time-dependent density functional theory (TDDFT).[70, 15, 101] The IP of the HOMO energy-level has a special significance in DFT because of Janak’s theorem and plays a prominent role in development and testing of DFT functionals. [33] Without loss of generality, the many-body correction to the IP can always be written as,

$$\omega_p = \omega_p^0 + \Delta\omega_p \quad (5.4)$$

where $\Delta\omega_p$ accounts for all of the correction terms missing from the Koopmans’ approximation; post-HF methods mentioned earlier offer different approximations and formulations for calculating $\Delta\omega_p$. However, efficient first-principles calculation of $\Delta\omega_p$ for large chemical systems continues to be challenging and is an active field of research. Using the electron-propagator method, Ortiz and coworkers developed a series of approximations that offer an order-by-order treatment of electron correlation to the many-body correction for IPs. [23, 59, 87, 27, 30] Open-shell systems possess additional complexities compared to their closed-shell counterparts, and the spin-flip EOM-IP approach has been used to treat open-shell systems. [93] In the GW formulation, the projective eigendecomposition of the dielectric screening (PDEP) algorithm has been used for calculating the quasiparticle gap of QDs.[39] In recent works, methods using stochastic techniques have been demonstrated to achieve the low-scaling needed for applications to large chemical systems. Specifically, the use of stochastic orbitals in the stochastic Green’s function method developed by R. Baer can be used for calculation of IPs.[119] A different strategy of combining Laplace-transformed expression of the self-energy operator with real-space Monte Carlo integration scheme developed by Hirata and co-workers has been used for calculation of IPs at the second-order MP2 level. [124] The approach was recently extended for ground-state MP4 level. [31] In a related work by Li et al., the Laplace-transformed MP2 has been combined with the density-of-states approach to reduce the overall computational cost of the MP2 calculation. [66] This approach demonstrated the effectiveness of the intrinsic degeneracies present in chemical systems to reduce the overall cost of MP2 calculations.

In this work, we present the stratified stochastic enumeration of molecular orbitals (SSE-MO) method and its application for the efficient computation of the IP through solution of the Dyson equation. The SSE-MO method was originally inspired by the 2013 paper, “*Stochastic Enumeration Method for Counting NP-Hard Problems*” by Rubinstein. [99] The original stochastic enumeration by Rubinstein was based on the importance sampling scheme. In the field of computer science, the stochastic enumeration technique has been applied to traversing deep tree structures and implementing backtracking algorithms. [99] To the best of our knowledge the paper, *Investigation of Ionization Potential in Quantum Dots Using the Stratified Stochastic Enumeration of Molecular Orbitals Method*, provides the first presentation in literature, of the use of stochastic enumeration combined with stratified sampling. For the SSE-MO method, we have combined stochastic enumeration with stratified sampling to perform the necessary summations over a direct-product space of molecular orbital indices and 6D Cartesian coordinate space. The reduced computational cost of

the SSE-MO method allowed us to investigate the full frequency-dependent pole structure of the 1-particle Green's function by an iterative solution of the Dyson equation. In this work, the SSE-MO method was used to investigate IPs of PbS and CdS QDs. Furthermore, the frequency-dependent spectral functions were constructed for the PbS and CdS systems. [114] The motivation for the

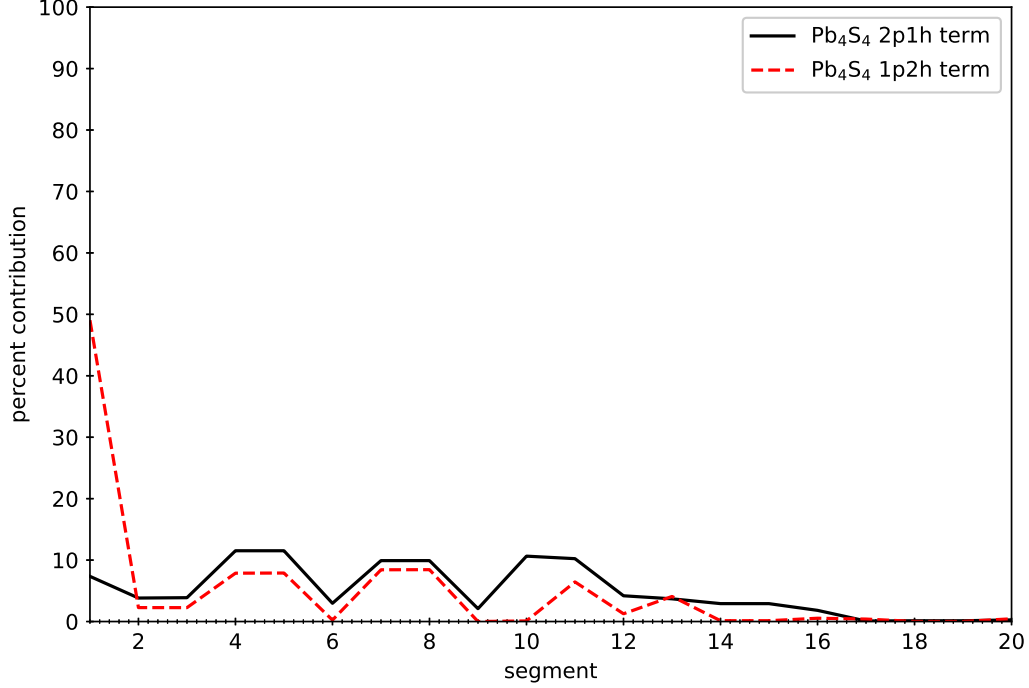


Figure 5.1: The percent contribution of terms A_i^{2p1h} and A_i^{1p2h} (defined in Equation 5.5) to the total self-energy as a function of hole index (i) for Pb₄S₄.

SSE-MO method comes from the fact that not all terms contribute equally to the overall self-energy operator. A similar observation has also been made for the density-of-state MP2 method. [66] For example, for the Pb₄S₄ system, the contribution for each term as a function of the hole-index, (i), is presented in Figure 5.1. Without loss of generality, the self-energy operator can be written as the sum of 2-particle 1-hole (2p1h) and 1-particle 2-hole (1p2h) terms as shown in Equation 5.5.

$$\Sigma^{(2)}(\omega) = \sum_{i=1}^{N_{\text{occ}}} A_i^{2p1h}(\omega) + \sum_{i=1}^{N_{\text{occ}}} A_i^{1p2h}(\omega) \quad (5.5)$$

It is seen that some terms contribute more than other terms. The SSE-MO method aims to distribute the computation effort used to calculate of the overall self-energy operator in proportion to the contribution of each of the terms and their associated errors. [114]

5.3 Theory

Stratified Stochastic Enumerated Tensor Contraction

As an introduction to the application of SSE for the calculation of the self-energy operator, we present the SSE approach for performing a general N -index tensor contraction. We start by considering the following general tensor contraction $S = \text{Tr}\{\mathbf{ABCD}\}$.

$$S = \sum_{i_1=1}^N \sum_{i_2=1}^N \cdots \sum_{i_{12}=1}^N A_{i_1 i_2 i_3} B_{i_4 i_5 i_6} C_{i_7 i_8 i_9} D_{i_{10} i_{11} i_{12}} G_{i_1 i_2 \dots i_{12}} \quad (5.6)$$

One situation for which this type of tensor contraction is encountered is when the integration of a 4-point kernel in real space $\langle A(\mathbf{r}_1)B(\mathbf{r}_2)C(\mathbf{r}_3)D(\mathbf{r}_4)G(\mathbf{r}_1, \mathbf{r}_2, \mathbf{r}_3, \mathbf{r}_4) \rangle$ on a spatial grid with N point per dimension is being performed. This tensor contraction has N^{12} terms and a simple sequential evaluation will require N^{12} terms. For the stratified stochastic enumeration approach, we will first define a composite index K such that $K = 1, \dots, N^{12}$. The composite index, K , uniquely maps each ordered set of indices $(i_1, i_2, i_3, \dots, i_{12})$ to an integer in $1, \dots, N^{12}$.

$$\Lambda_K \equiv A_{i_1 i_2 i_3} B_{i_4 i_5 i_6} C_{i_7 i_8 i_9} D_{i_{10} i_{11} i_{12}} G_{i_1 i_2 \dots i_{12}} \quad (5.7)$$

Using the composite index K , we can define the summation as displayed in the following equation.

$$S = \sum_{K=1}^{N^{12}} \Lambda_K \quad (5.8)$$

Next, we divide the entire range of K into N non-overlapping segments $N_{\text{seg}} = N$. The number of terms in each segment is $N_T = N^{11}$. The summation over K can be written in terms of the segmented summation.

$$S = S_1 + S_2 + S_3 + \cdots + S_N \quad (5.9)$$

$$S_1 = \sum_{K=1}^{N_T} \Lambda_K \quad (5.10)$$

$$S_2 = \sum_{K=1}^{N_T} \Lambda_{K+N_T} \quad (5.11)$$

$$S_3 = \sum_{K=1}^{N_T} \Lambda_{K+(2N_T)} \quad (5.12)$$

$$\vdots = \vdots \quad (5.13)$$

$$S_N = \sum_{K=1}^{N_T} \Lambda_{K+((N-1)N_T)} \quad (5.14)$$

The partial averages are defined as follows.

$$\bar{X}_1 = \frac{S_1}{N_T}, \bar{X}_2 = \frac{S_2}{N_T}, \dots, \bar{X}_N = \frac{S_N}{N_T} \quad (5.15)$$

The total sum can be written as displayed in the equation below.

$$S = N_T[\bar{X}_1 + \bar{X}_2 + \dots + \bar{X}_N] \quad (5.16)$$

In SSE, the sequential segment average, \bar{X} , is approximated using the stochastic average,

$$\bar{X}_1^{\text{SSE}}(M_1) = \frac{1}{M_1} \sum_{K \sim_{\text{swr}} [1, \dots, N_T]}^{M_1} \Lambda_K \quad (5.17)$$

$$\bar{X}_2^{\text{SSE}}(M_2) = \frac{1}{M_2} \sum_{K \sim_{\text{swr}} [1, \dots, N_T]}^{M_2} \Lambda_{K+(2N_T)} \quad (5.18)$$

$$\vdots = \vdots \quad (5.19)$$

$$\bar{X}_N^{\text{SSE}}(M_N) = \frac{1}{M_N} \sum_{K \sim_{\text{swr}} [1, \dots, N_T]}^{M_N} \Lambda_{K+((N-1)N_T)} \quad (5.20)$$

where the subscript in $K \sim_{\text{swr}} [1, \dots, N_T]$ denotes ‘‘sampling-without-replacement’’. For any segment ‘‘ p ’’, the SSE average approaches the sequential average as $M_p \rightarrow N_T$.

$$\lim_{M_p \rightarrow N_T} \bar{X}_p^{\text{SSE}}(M_p) = \bar{X}_p \quad (5.21)$$

The SSE estimate of the total summation is presented in the equation below.

$$S^{\text{SSE}} = N_T \sum_{p=1}^N \bar{X}_p^{\text{SSE}}(M_p) \quad (5.22)$$

The allocation of the sampling points for each segment is proportional to the variance in the SSE segment average \bar{X}_p^{SSE} .

$$M_p \propto \bar{X}_p^{\text{SSE}} \quad (5.23)$$

$$\propto \mathbb{V}[\bar{X}_p^{\text{SSE}}] \quad (5.24)$$

The SSE approach is based on stratified sampling, which has been used extensively for reducing sampling error in Monte Carlo calculations[94, 64, 65] and a brief description stratified sampling is presented in the supporting information. The SSE method is not restricted to square tensors and can be applied to rectangular tensors as well. We recommend a row-major composite indexing scheme. For an index vector $(i_1, i_2, i_3, \dots, i_D)$, where D is the dimension of the tensor and each index $(i_d, d = 1, D)$ is in the range $(i_d = 1, \dots, N_d)$, the row-major composite index K can be calculated using the following expression.

$$K = 1 + \sum_{d=1}^D \left[\left(\prod_{j=1}^{d-1} N_j \right) (i_d - 1) \right] \quad (5.25)$$

Second-order Dyson Equation

In this work we are interested in calculating the IPs of chemical systems. The component of the 1-particle Green's function, $\mathbf{G}(\omega)$, that contains information about the IPs can be expressed in the Lehman representation as follows. [37]

$$G_{pq}(\omega) = \lim_{\eta \rightarrow 0^+} \langle \Psi_0^N | a_q^\dagger \frac{1}{\omega - (E_0^N - H) - i\eta} a_p | \Psi_0^N \rangle \quad (5.26)$$

where, G_{pq} is the matrix element of the matrix representation of the operator in canonical Hartree-Fock (HF) orbital basis $\{\chi_p\}$,

$$f|p\rangle = \epsilon_p|p\rangle, \quad (5.27)$$

$\{a_q^\dagger, a_p\}$ are creation and annihilation operators defined with respect to the HF orbitals, $\{E_0^N, \Psi_0^N\}$ are the exact ground state energies and wave function, and H is the electronic Hamiltonian. By inserting a complete set of projectors, $1 = \sum_m |\Psi_m^{N-1}\rangle \langle \Psi_m^{N-1}|$, we obtain the following equation.

$$G_{pq}(\omega) = \lim_{\eta \rightarrow 0^+} \sum_m \frac{A_{mq}^* A_{mp}}{\omega - (E_0^N - E_m^{N-1}) - i\eta} \quad (5.28)$$

As shown in Equation 5.28, the Green's function's poles correspond to the vertical IPs of a many-electron system.

$$\omega_{\text{pole}} = E_{\text{IP}} \quad (5.29)$$

The quantity $|A_{mp}|^2$ is the residue of the pole and is known as the pole strength.

$$A_{mp} = \langle \Psi_m^{N-1} | a_p | \Psi_0^N \rangle \quad (5.30)$$

The limit $\eta \rightarrow 0^+$ in Equation 5.28 is traditionally associated with this expression because of its use in performing the Fourier transform from the time-domain to frequency-domain and will be suppressed in the rest of the derivation. Analogous to the many-body Green's function, the uncorrelated HF Green's function \mathbf{G}^0 is given by the following expression. [37]

$$G_{pq}^0(\omega) = \langle \Phi_0^N | a_q^\dagger \frac{1}{\omega - (E_{\text{HF}}^N - H_0)} a_p | \Phi_0^N \rangle \quad (5.31)$$

which immediately simplifies to following diagonal representation. [37]

$$G_{ij}^0(\omega) = \frac{\delta_{ij}}{\omega - \epsilon_i} \quad (5.32)$$

where $i, j = 1, N_{\text{occ}}$ are indices for occupied orbitals and ϵ_i is the orbital energy. The above equation recovers the Koopmans' approximation to the IPs, which is defined as $E_{\text{IP}}^{\text{Koopmans}} = -\epsilon_i$.

In the frequency representation, the relationship between the correlated 1-particle Green's function, G , and the uncorrelated Green's function G_0 is given by the well-known Dyson equation. [28]

$$\mathbf{G}(\omega) = \mathbf{G}^0(\omega) + \mathbf{G}^0(\omega) \mathbf{\Sigma}(\omega) \mathbf{G}(\omega) \quad (5.33)$$

Here, Σ is the self-energy operator. The relationship between the correlated and uncorrelated Green's function can be derived using various techniques including time-dependent perturbation theory, time-independent perturbation theory, coupled-cluster theory, the configuration interaction method, and electron-propagator methods. [37, 110, 83, 84, 16] The above operator equation can also be presented in various representations such as plane-waves, real-space grids, and canonical HF orbitals. [92, 39, 62] In this work, we use canonical HF orbitals to represent the Dyson equation.[28] To facilitate the calculation of the poles, it is useful to express Equation 5.33 in terms of inverse operators by multiplying $G^{-1}(\omega)$ from left and $G_0^{-1}(\omega)$ from the right.

$$\mathbf{G}^{-1}(\omega) = \mathbf{G}_0^{-1}(\omega) - \Sigma(\omega) \quad (5.34)$$

Once $\mathbf{G}(\omega)$ is determined for an appropriate set of values of ω , the poles can be observed by constructing a plot of $\mathbf{G}(\omega)$ versus ω . Approximating the total self-energy operator by diagonal representation,

$$\Sigma(\omega) \approx \text{diag}[\Sigma(\omega)] \quad (5.35)$$

allows for analytical inversion of the Dyson equation into the following simplified expression,[28]

$$\omega_i^0 + \Sigma_{ii}(\omega) = \omega \quad (5.36)$$

where ω_i^0 is the orbital energy of occupied orbital (i) and $\omega = -E_{\text{IP}}$. We have used the second-order approximation to the self-energy operators, which in the canonical MO basis is defined as,[28]

$$\begin{aligned} \Sigma_{ii} \approx \Sigma_{ii}^{(2)}(\omega) &= \frac{1}{2} \sum_{jab} \frac{\langle ij | r_{12}^{-1} | ab \rangle_A \langle ab | r_{12}^{-1} | ij \rangle_A}{\omega + \epsilon_j - \epsilon_a - \epsilon_b} \\ &+ \frac{1}{2} \sum_{jak} \frac{\langle ia | r_{12}^{-1} | jk \rangle_A \langle jk | r_{12}^{-1} | ia \rangle_A}{\omega + \epsilon_a - \epsilon_j - \epsilon_k} \end{aligned} \quad (5.37)$$

where i, j , and k indicate occupied spin orbitals and a and b indicate virtual spin orbitals.

Using the restricted Hartree-Fock (RHF) formulation, the correction to the orbital energies using the second-order self-energy expression can be written as,

$$\epsilon_p^{(2)} = \epsilon_p + \Sigma_p^{(C)}(\omega) + \Sigma_p^{(D)}(\omega) + \Sigma_p^{(E)}(\omega) + \Sigma_p^{(F)}(\omega) \quad (5.38)$$

where the RHF expressions for the self-energy terms are defined as,

$$\Sigma_p^{(C)}(\omega) = 2 \sum_{iab} \frac{V_{iapb} V_{iapb}}{E_{iab}^{2\text{p1h}}(\omega)} \quad (5.39)$$

$$\Sigma_p^{(D)}(\omega) = - \sum_{iab} \frac{V_{iapb} V_{ibpa}}{E_{iab}^{2\text{p1h}}(\omega)} \quad (5.40)$$

$$\Sigma_p^{(E)}(\omega) = -2 \sum_{ija} \frac{V_{ipja} V_{ipja}}{E_{ija}^{1\text{p2h}}(\omega)} \quad (5.41)$$

$$\Sigma_p^{(F)}(\omega) = \sum_{ija} \frac{V_{ipja}V_{iajp}}{E_{ija}^{1p2h}(\omega)} \quad (5.42)$$

Here, we have used the following compact notation for the energy denominators,

$$E_{iab}^{2p1h}(\omega) = \omega + \epsilon_i - \epsilon_a - \epsilon_b \quad (5.43)$$

$$E_{ija}^{1p2h}(\omega) = \epsilon_i + \epsilon_j - \omega - \epsilon_a \quad (5.44)$$

and the r_{12}^{-1} matrix elements are defined using the chemist's notation for the indices.

$$V_{pqst} = \int_{-\infty}^{+\infty} d\mathbf{r}_1 d\mathbf{r}_2 \psi_p(\mathbf{r}_1) \psi_q(\mathbf{r}_1) r_{12}^{-1} \psi_s(\mathbf{r}_2) \psi_t(\mathbf{r}_2) \quad (5.45)$$

Next, we will develop the SSE-MO approach for evaluating the self-energy operator.

Stratified Stochastic Enumeration of Self-energy

We begin by defining a set \mathcal{S}^{2p1h} of ordered integers (i, a, b) ,

$$\mathcal{S}^{2p1h} = \{(i, a, b)\} \quad i = 1, \dots, N_{\text{occ}}; (a, b) = 1, \dots, N_{\text{vir}} \quad (5.46)$$

which contains all the possible combinations of indices that occur in 2p1h self-energy expression. We will use the composite index $K = (i, a, b)$ to enumerate this ordered set of integers. The size of set \mathcal{S}^{2p1h} is given as,

$$K_{\text{max}}^{2p1h} = |\mathcal{S}^{2p1h}| = N_{\text{occ}} \times N_{\text{vir}}^2 \quad (5.47)$$

Using this notation, we can define a general form of the 2p1h self-energy term as follows.

$$X_p^{2p1h} = \sum_{K=1}^{K_{\text{max}}^{2p1h}} \frac{A_{pK} B_{pK}}{E_K^{2p1h}} \quad (5.48)$$

where,

$$A_{pK} \equiv V_{iapb} \quad (5.49)$$

$$B_{pK} \equiv V_{iapb} \quad \text{for } \Sigma_p^{(C)} \quad (5.50)$$

$$B_{pK} \equiv V_{ibpa} \quad \text{for } \Sigma_p^{(D)} \quad (5.51)$$

In [Equation 5.48](#) the summation is performed sequentially for all terms. In the stochastic enumeration (SE) approach the sequential sum is replaced by a stochastic summation. We define a new operator $\tilde{\Sigma}$ which is defined as follows,

$$\tilde{X}_p^{2p1h} = K_{\text{max}}^{2p1h} \times \frac{1}{N_{\text{sample}}^{\text{MO}}} \sum_{K \sim \mathcal{S}^{2p1h}}^{N_{\text{sample}}^{\text{MO}}} \frac{A_{pK} B_{pK}}{E_K^{2p1h}} \quad (5.52)$$

and where K is sampled from the set \mathcal{S}^{2p1h} . This sampling is performed without replacement and the notation $K \sim_{\text{swr}} \mathcal{S}^{2p1h}$ is used to emphasize this procedure (sample-without-replacement). The $N_{\text{sample}}^{\text{MO}}$ is sample size and bounded from above by K_{max}^{2p1h} . In the limit when the sample size approaches K_{max}^{2p1h} the following limiting condition is satisfied.

$$X_p^{2p1h}(\omega) = \lim_{N_{\text{sample}}^{\text{MO}} \rightarrow K_{\text{max}}^{2p1h}} \tilde{X}_p^{2p1h}(\omega) \quad (5.53)$$

Simple stochastic enumeration will involve performing the sampling over multiple runs and averaging the final results.

$$\tilde{X}_p^{2p1h,\text{avg}} = \frac{1}{N_{\text{runs}}} [\tilde{X}_p^{2p1h,1} + \tilde{X}_p^{2p1h,2} + \dots + \tilde{X}_p^{2p1h,N_{\text{runs}}}] \quad (5.54)$$

The variance is defined as follows.

$$\mathbb{V}[\tilde{X}_p^{2p1h}] = \sum_{L=1}^{N_{\text{runs}}} [\tilde{X}_p^{2p1h,\text{avg}} - \tilde{X}_p^{2p1h,L}]^2 \quad (5.55)$$

We expect the variance to disappear when $N_{\text{sample}}^{\text{MO}}$ approaches K_{max}^{2p1h} ,

$$\lim_{N_{\text{sample}}^{\text{MO}} \rightarrow K_{\text{max}}^{2p1h}} \mathbb{V}[\tilde{X}_p^{2p1h}] = 0 \quad (5.56)$$

To reduce the variance of the overall calculations, we introduce stratification in the sampling procedure. This is achieved in two steps. First, the set \mathcal{S}^{2p1h} is decomposed into a union of non-intersecting subsets,

$$\mathcal{S}^{2p1h} = \mathcal{S}^{2p1h,1} \cup \mathcal{S}^{2p1h,2} \cup \mathcal{S}^{2p1h,3} \dots \cup \mathcal{S}^{2p1h,N_{\text{seg}}^{\text{MO}}} \quad (5.57)$$

$$= \bigcup_{M=1}^{N_{\text{seg}}^{\text{MO}}} \mathcal{S}^{2p1h,M} \quad (5.58)$$

where the subsets are non-overlapping.

$$\mathcal{S}^{2p1h,M} \cap \mathcal{S}^{2p1h,M'} = \emptyset \quad \text{for } M \neq M' \quad (5.59)$$

The number of elements in subset M is denoted as $K_{\text{max}}^{2p1h,M}$.

$$K_{\text{max}}^{2p1h,M} = |\mathcal{S}^{2p1h,M}| \quad (5.60)$$

In the second step, \tilde{X}^{2p1h} is calculated using summation over all the subsets.

$$X_p^{2p1h} = \sum_{M=1}^{N_{\text{seg}}^{\text{MO}}} \sum_{K=1}^{K_{\text{max}}^{2p1h,M}} \frac{A_{pK} B_{pK}}{E_K^{2p1h}} \quad (5.61)$$

The stratified stochastic enumeration of the MO indices (SSE-MO), which uses stochastic enumeration for segment sampling, is described by the following equation.

$$\tilde{X}_p^{2p1h}(\omega) = \sum_{M=1}^{N_{\text{seg}}^{\text{MO}}} \frac{K_{\text{max}}^{2p1h,M}}{N_{\text{sample}}^{\text{MO},M}} \sum_{K \sim S^{2p1h,M}_{\text{swr}}}^{N_{\text{sample}}^{\text{MO},M}} \frac{A_{pK} B_{pK}}{E_K^{2p1h}(\omega)} \quad (5.62)$$

To write the expressions in compact notation, we introduce the following for stochastic summation.

$$\sum_K \boxtimes \equiv \sum_{M=1}^{N_{\text{seg}}^{\text{MO}}} \frac{K_{\text{max}}^{2p1h,M}}{N_{\text{sample}}^{\text{MO},M}} \sum_{K \sim S^{2p1h,M}_{\text{swr}}}^{N_{\text{sample}}^{\text{MO},M}} \quad (5.63)$$

Using this notation, we can write the following expression.

$$\tilde{X}_p^{2p1h}(\omega) = \sum_K \boxtimes \frac{A_{pK} B_{pK}}{E_K^{2p1h}(\omega)} \quad (5.64)$$

A similar treatment is performed for the 1p2h terms. The combined result for the total self-energy operator is given as,

$$\Sigma_p(\omega) = 2 \sum_{iab} \boxtimes \frac{V_{iapb} V_{iapb}}{E_{iab}^{2p1h}(\omega)} - \sum_{iab} \boxtimes \frac{V_{iapb} V_{ibpa}}{E_{iab}^{2p1h}(\omega)} - 2 \sum_{ija} \boxtimes \frac{V_{ipja} V_{ipja}}{E_{ija}^{1p2h}(\omega)} + \sum_{ija} \boxtimes \frac{V_{ipja} V_{iajp}}{E_{ija}^{1p2h}(\omega)} \quad (5.65)$$

Calculation of Optimal Sampling Points for MO-space Stratified Sampling

To calculate optimal sampling points, we define the segment average as,

$$\tilde{Y}_p^{2p1h,M} = \frac{1}{N_{\text{sample}}^{\text{MO},M}} \sum_{K \sim S^{2p1h,M}_{\text{swr}}}^{N_{\text{sample}}^{\text{MO},M}} \frac{A_{pK} B_{pK}}{E_K^{2p1h}(\omega)} \quad (5.66)$$

which allows us to write the following expression.

$$\tilde{X}_p^{2p1h} = \sum_{M=1}^{N_{\text{seg}}^{\text{MO}}} k_{\text{max}}^{2p1h,M} \tilde{Y}_p^{2p1h,M} \quad (5.67)$$

It is important to note that $\tilde{Y}_p^{2p1h,M}$ is a stochastic variable for which the average value, $\tilde{Y}_p^{2p1h,M,\text{avg}}$, can be obtained by sampling over multiple runs.

$$\tilde{Y}_p^{2p1h,M,\text{avg}} = \frac{1}{N_{\text{runs}}} \sum_{L=1}^{N_{\text{runs}}} \tilde{Y}_p^{2p1h,M,L} \quad (5.68)$$

The variance is defined as,

$$\mathbb{V}[\tilde{Y}_p^{2p1h,M}] = \frac{1}{N_{\text{runs}}} \sum_{L=1}^{N_{\text{runs}}} [\tilde{Y}_p^{2p1h,M,\text{avg}} - \tilde{Y}_p^{2p1h,M,L}]^2 \quad (5.69)$$

The variance of \tilde{Y} goes to zero as $N_{\text{sample}}^{\text{MO},M}$ approaches $K_{\text{max}}^{2\text{p1h},M}$,

$$\lim_{N_{\text{sample}}^{\text{MO},M} \rightarrow K_{\text{max}}^{2\text{p1h},M}} \mathbb{V}[\tilde{Y}_p^{2\text{p1h},M}] = 0 \quad (5.70)$$

To distribute the sampling points optimally, we define the following weight factor,

$$w_M^{\text{var}} = \frac{\mathbb{V}[\tilde{Y}_p^{2\text{p1h},M}]}{\sum_{M'}^{N_{\text{seg}}^{\text{MO}}} \mathbb{V}[\tilde{Y}_p^{2\text{p1h},M'}]} \quad (5.71)$$

In addition to that we also define another weight factor that depends on the magnitude of the terms,

$$w_M^{\text{mag}} = \frac{|\mathbb{E}[\tilde{Y}_p^{2\text{p1h},M}]|}{\sum_{M'}^{N_{\text{seg}}^{\text{MO}}} |\mathbb{E}[\tilde{Y}_p^{2\text{p1h},M'}]|} \quad (5.72)$$

The sampling is performed in batches, and the variance is updated after completion of a batch. The number of sampling points for each segment has the general form of,

$$N_{\text{sample}}^{\text{MO},M} = N_{\text{base}} + (w_M^{\text{var}} \times N_{\text{opt}}) + (w_M^{\text{mag}} \times N_{\text{opt}}) \quad (5.73)$$

where all segments get N_{base} sample points per batch irrespective of the segment average and variance. N_{opt} indicates the number of additional sample points that are distributed in a manner that is proportional to the normalized weights, which depend on the segment average and variance.

Low-discrepancy Sampling without Replacement Using Quasi-Monte Carlo Method

It is important to note that obtaining $K \sim \mathcal{S}_{\text{swr}}$ is a correlated sampling process. It is intrinsically non-Markovian and depends on the entire history of the string of previously generated indices. One way to achieve this in discrete integer space is by performing self-avoiding random walks. However, sampling in the self-avoiding random walker is local in nature, and therefore is not ideal for variance reduction in each segment. Here we use quasi-Monte Carlo sampling and a low-discrepancy integer sequence to perform sampling within each segment.[94, 64, 65] The linear congruent generator for low-discrepancy quasi-random numbers is modified for generation of integer sequences.[94] The sampling index for a segment M is defined as $K^{(M)}$ and can have values in the range $[1, \dots, K_{\text{max}}^{(M)}]$. The exact value of $K_{\text{max}}^{(M)}$ for each segment is known at the start of the calculation and is a consequence of the stratification procedure described in Equation 5.3. Associated with each segment are two integer random numbers which we define as $q^{(M)}$ and $r^{(M)}$. The variable $q^{(M)}$ impacts the discrepancy of the points and is an integer random number chosen randomly from the interval $q^{(M)} \sim [10, 50]$. Using $q^{(M)}$, we define the following sequence from which $r^{(M)}$ is selected randomly.

$$r^{(M)} \sim [1, 2, 3, \dots, q - 1, 0] \quad (5.74)$$

Using $q^{(M)}$ and $r^{(M)}$, the low-discrepancy sequence is defined as,

$$K^{(M)} = (n \times q^{(M)}) + r^{(M)} \quad (5.75)$$

$$n = [1, 2, 3, \dots, \lfloor K_{\text{max}}^{(M)} / q^{(M)} \rfloor] \quad (5.76)$$

where $\lfloor K_{\text{max}}^{(M)} / q^{(M)} \rfloor$ is the floor of the ratio.

Control Variate for Monte Carlo Evaluation of Two-electron Integrals

In this section, we extend the stochastic procedure developed in the previous section for numerical evaluation of the two-electron integrals. Monte Carlo evaluation of the two-electron integrals is not a requirement for implementing the SSE-MO method, and the SSE-MO procedure described in Equation 5.3 can be used whenever the two-electron repulsion integrals, V_{pqst} , are available in MO representation. However for large systems, it is computationally advantageous to avoid the AO-to-MO two-electron transformation and instead, to numerically integrate directly in the MO representation using the Monte Carlo scheme.

Associated with each MO pair function, $\psi_p(\mathbf{r})\psi_q(\mathbf{r})$, we define a control-variate function, $\psi_{pq}^{\text{cv}}(\mathbf{r})$. The control variate function must satisfy two important features. First, $\psi_{pq}^{\text{cv}}(\mathbf{r})$ must be non-factorizable as a product of functions that depend only p and q indices.

$$\psi_{pq}^{\text{cv}}(\mathbf{r}) \neq f_p(\mathbf{r}) \times f_q(\mathbf{r}) \quad (5.77)$$

Second, the two-electron integrals, $[\psi_{pq}^{\text{cv}}(\mathbf{r}_1)|r_{12}^{-1}|\psi_{st}^{\text{cv}}(\mathbf{r}_2)]$, must be known analytically. Adding and subtracting the control variate function, we express the MO product function as follows.

$$\psi_p(\mathbf{r})\psi_q(\mathbf{r}) = \alpha_{pq}\psi_{pq}^{\text{cv}}(\mathbf{r}) + [\psi_p(\mathbf{r})\psi_q(\mathbf{r}) - \alpha_{pq}\psi_{pq}^{\text{cv}}(\mathbf{r})] \quad (5.78)$$

$$= \alpha_{pq}\psi_{pq}^{\text{cv}}(\mathbf{r}) + d_{pq}(\mathbf{r}) \quad (5.79)$$

Here, α_{pq} is the control variate and $d_{pq}(\mathbf{r})$ is the difference function. Using the above expression, the two-electron integral can be expressed as,

$$V_{pqst} = V_{pqst}^{\text{cv}} + D_{pqst} \quad (5.80)$$

where,

$$V_{pqst}^{\text{cv}} = \alpha_{pq}\alpha_{st}[\psi_{pq}^{\text{cv}}(\mathbf{r}_1)|r_{12}^{-1}|\psi_{st}^{\text{cv}}(\mathbf{r}_2)] \quad (5.81)$$

and,

$$D_{pqst} = \alpha_{pq}[\psi_{pq}^{\text{cv}}(\mathbf{r}_1)|r_{12}^{-1}|d_{st}(\mathbf{r}_2)] + \alpha_{st}[d_{pq}(\mathbf{r}_1)|r_{12}^{-1}|\psi_{st}^{\text{cv}}(\mathbf{r}_2)] + [d_{pq}(\mathbf{r}_1)|r_{12}^{-1}|d_{st}(\mathbf{r}_2)] \quad (5.82)$$

The control variate, α_{pq} , is defined as the quantity that minimizes the following weighted-variance function.

$$\underset{\alpha}{\text{argmin}} \frac{\sum_{\mathbf{r} \in S^{\text{space}}} [\psi_p(\mathbf{r})\psi_q(\mathbf{r}) - \alpha\psi_{pq}^{\text{cv}}(\mathbf{r})]^2 |\psi_p(\mathbf{r})\psi_q(\mathbf{r})|^2}{\sum_{\mathbf{r} \in S^{\text{space}}} |\psi_p(\mathbf{r})\psi_q(\mathbf{r})|^2} = \alpha_{pq} \quad (5.83)$$

Here, S^{space} is a set of sampling points in 3D space from which \mathbf{r} is drawn at random. The control-variate functions, ψ_{pq}^{cv} , are represented by Gaussian functions. For $p = q$, a single Gaussian function is used and for $p \neq q$ a linear combination of two Gaussian functions is used.

$$\psi_{pp}^{\text{cv}} = \left(\frac{a_{pp}}{\pi}\right)^{3/2} e^{-a_{pp}(\mathbf{r}-\mathbf{A}_{pp})^2} \quad (5.84)$$

$$\psi_{pq}^{\text{cv}} = c_{pq} \left[\left(\frac{a_{pq}}{\pi}\right)^{3/2} e^{-a_{pq}(\mathbf{r}-\mathbf{A}_{pq})^2} - \left(\frac{b_{pq}}{\pi}\right)^{3/2} e^{-b_{pq}(\mathbf{r}-\mathbf{B}_{pq})^2} \right] \quad \text{for } (p \neq q) \quad (5.85)$$

This form of the control variate function guarantees the orthonormality conditions for the MOs.

$$\langle \psi_p | \psi_q \rangle = \langle \psi_{pq}^{cv} \rangle = \delta_{pq} \quad (5.86)$$

The widths and the centers of the Gaussian functions are determined using a moment-matching condition. The weighted moments for any pair of molecular orbitals are calculated as,

$$\mu_{pq}(m_x, m_y, m_z) = \frac{\sum_{\mathbf{r} \in S^{\text{space}}} [\psi_p(\mathbf{r})(x^{m_x} y^{m_y} z^{m_z}) \psi_q(\mathbf{r})] |\psi_p(\mathbf{r}) \psi_q(\mathbf{r})|^2}{\sum_{\mathbf{r} \in S^{\text{space}}} |\psi_p(\mathbf{r}) \psi_q(\mathbf{r})|^2} \quad (m_x, m_y, m_z = 0, \dots, 3) \quad (5.87)$$

and the moments for the control-variate functions are obtained analytically.

$$\mu_{pq}^{cv}(m_x, m_y, m_z) = \langle \psi_{pq}^{cv}(x^{m_x} y^{m_y} z^{m_z}) \rangle \quad (5.88)$$

The coefficients for the control-variate function are obtained by performing a steepest-descent search on the following loss-function.

$$\underset{a_{pq}>0, b_{pq}>0, \mathbf{A}_{pq}, \mathbf{B}_{pq}}{\text{argmin}} \sum_{m_x, m_y, m_z=0,3} [\mu_{pq} - \mu_{pq}^{cv}]^2 \quad (5.89)$$

The equations [Equation 5.83](#) and [Equation 5.89](#) completely define the control-variate function and are used to calculate the V_{pqst}^{cv} term.

Monte Carlo Evaluation of Two-electron Integrals Using Real-space Stratified Sampling

Since V_{pqst}^{cv} is analytical, only the D_{pqst} terms are calculated numerically using the stratified Monte Carlo procedure. We use a combination of ratio estimator, control variate, and stratified sampling techniques to efficiently and accurately evaluate the MO integrals. For calculating D_{pqst} we define the following two-electron kernel function,

$$D_{pqst} = \int_{-\infty}^{+\infty} d\mathbf{r}_1 d\mathbf{r}_2 T_{pqst}(\mathbf{r}_1, \mathbf{r}_2) r_{12}^{-1} \quad (5.90)$$

where,

$$T_{pqst}(\mathbf{r}_1, \mathbf{r}_2) = \alpha_{pq} [\psi_{pq}^{cv}(\mathbf{r}_1) d_{st}(\mathbf{r}_2)] + \alpha_{st} [d_{pq}(\mathbf{r}_1) \psi_{st}^{cv}(\mathbf{r}_2)] + [d_{pq}(\mathbf{r}_1) d_{st}(\mathbf{r}_2)] \quad (5.91)$$

Associated with each D_{pqst} integral, we define a control variate f_{pqst}^{cv} as,

$$f_{pqst}^{cv}(\mathbf{r}_1, \mathbf{r}_2) = \frac{1}{4} [|\psi_p(\mathbf{r}_1)|^2 + |\psi_q(\mathbf{r}_1)|^2] \times [|\psi_s(\mathbf{r}_2)|^2 + |\psi_t(\mathbf{r}_2)|^2] \quad (5.92)$$

where the integral of the control variate is 1 for all values of p, q, s, t .

$$\int_{-\infty}^{+\infty} d\mathbf{r}_1 d\mathbf{r}_2 f_{pqst}^{cv}(\mathbf{r}_1, \mathbf{r}_2) = 1 \quad (5.93)$$

The calculation of D_{pqst} requires evaluation of the six-dimensional integral over all space. Traditionally, Monte Carlo integration is performed over an N-dimensional unit cube by transforming

the integral range from $[-\infty, +\infty]$ to $[0,1]$. One approach to achieve this is by using the following transformation,

$$t = \frac{x}{1+x} \quad (5.94)$$

$$\int_{-\infty}^{+\infty} dx f(x) = \int_0^{+\infty} dx [f(x) + f(-x)] = \int_0^1 dt J(t) [f(x) + f(-x)] \quad (5.95)$$

However this procedure introduces singularity in the form of the Jacobian $J(t)$ in the integration kernel. In this work, we use a finite-grid approximation to evaluate the integral over a finite volume,

$$\int_{-a}^{+a} d\mathbf{r} f(\mathbf{r}) = V_{3D} \langle f \rangle = 1 \pm \epsilon \quad (5.96)$$

where the limits selected are large enough so that $\epsilon \leq 10^{-5}$ for all MOs. Using f_{pqst}^{cv} , we define the following ratio estimator for Monte Carlo evaluation of the D_{pqst} integral.

$$D_{pqst} = \frac{\int_{-\infty}^{+\infty} d\mathbf{r}_1 d\mathbf{r}_2 T_{pqst}(\mathbf{r}_1, \mathbf{r}_2) r_{12}^{-1}}{\int_{-\infty}^{+\infty} d\mathbf{r}_1 d\mathbf{r}_2 f_{pqst}^{cv}(\mathbf{r}_1, \mathbf{r}_2)} \approx \frac{\langle T_{pqst} r_{12}^{-1} \rangle}{\langle f_{pqst}^{cv} \rangle} \quad (5.97)$$

The averages $\langle T_{pqst} r_{12}^{-1} \rangle$ and $\langle f_{pqst}^{cv} \rangle$ are defined as follows.

$$\langle T_{pqst} r_{12}^{-1} \rangle = \frac{1}{N_{\text{sample}}^{\text{space}}} \sum_{\mathbf{r}_1, \mathbf{r}_2 \in \mathcal{S}_{\text{space}}} T_{pqst}(\mathbf{r}_1, \mathbf{r}_2) r_{12}^{-1} \quad (5.98)$$

$$\langle f_{pqst}^{cv} \rangle = \frac{1}{N_{\text{sample}}^{\text{space}}} \sum_{\mathbf{r}_1, \mathbf{r}_2 \in \mathcal{S}_{\text{space}}} f_{pqst}^{cv}(\mathbf{r}_1, \mathbf{r}_2) \quad (5.99)$$

We introduce stratification in the sampling of points in real-space by dividing the entire space into a set of $N_{\text{seg}}^{\text{space}}$ non-overlapping regions with identical volumes.

$$\mathcal{S}_{\text{space}} = \sum_{M=1}^{N_{\text{seg}}^{\text{space}}} \mathcal{S}_{\text{space}}^{(M)} \quad (5.100)$$

$$V_{6D} = \sum_{M=1}^{N_{\text{seg}}^{\text{space}}} V_{\text{seg}}^{(M)} = N_{\text{seg}}^{\text{space}} \times V_{\text{seg}} \quad (5.101)$$

The stratified sampling estimate of the averages is then defined as,

$$\langle T_{pqst} r_{12}^{-1} \rangle = \sum_{M=1}^{N_{\text{seg}}^{\text{space}}} \frac{V_{\text{seg}}}{V_{6D}} \frac{1}{N_{\text{sample}}^{\text{space}, M, pqst}} \sum_{\mathbf{r}_1, \mathbf{r}_2 \in \mathcal{S}_{\text{space}}^{(M)}} T_{pqst}(\mathbf{r}_1, \mathbf{r}_2) r_{12}^{-1} \quad (5.102)$$

$N_{\text{sample}}^{\text{space}, M, \text{pqst}}$ is the number of sampling points associated with the spatial segment, M for indices p, q, s, t . Similar to the stratification strategy in Equation 5.73, the sampling points for each segment are proportional to the variance of the integral kernel in that segment.

$$N_{\text{sample}}^{\text{space}, M, \text{pqst}} \propto \mathbb{V}_M [T_{pqst}(\mathbf{r}_1, \mathbf{r}_2) r_{12}^{-1}] \quad (5.103)$$

$$\propto \mathbb{E}_M [|T_{pqst}(\mathbf{r}_1, \mathbf{r}_2) r_{12}^{-1}|] \quad (5.104)$$

We use common-random-number (CRN) sampling for sampling within a segment. The CRN method has been used extensively for reducing variance[94, 64, 65] and a brief summary of the method is presented in [115]. In the evaluation of the integral, this means that at any point in time, if a random number η_1 is used in the evaluation of T_{pqst} , then that same random number is used for evaluation of f_{pqst}^{cv} in the same segment. To emphasize this usage, we use superscript ‘‘CRN’’ (common random number) in the following expression.

$$D_{pqst} = \frac{\langle T_{pqst} r_{12}^{-1} \rangle}{\langle f_{pqst}^{\text{cv}} \rangle} = \frac{\sum_{M=1}^{N_{\text{seg}}^{\text{space}}} \frac{1}{N_{\text{sample}}^{\text{space}, M, \text{pqst}}} \sum_{\mathbf{r}_1, \mathbf{r}_2 \in \mathcal{S}_{\text{space}}^{(M)}} T_{pqst}(\mathbf{r}_1^{\text{CRN}}, \mathbf{r}_2^{\text{CRN}}) r_{12}^{-1}}{\sum_{M=1}^{N_{\text{seg}}^{\text{space}}} \frac{1}{N_{\text{sample}}^{\text{space}, M, \text{pqst}}} \sum_{\mathbf{r}_1, \mathbf{r}_2 \in \mathcal{S}_{\text{space}}^{(M)}} f_{pqst}^{\text{cv}}(\mathbf{r}_1^{\text{CRN}}, \mathbf{r}_2^{\text{CRN}})} \quad (5.105)$$

Iterative Solution of the Dyson Equation

Combining the results from Equation 5.3 and Equation 5.3, we can express the full self-energy operator as the sum of two terms,

$$\Sigma_p(\omega) = \Sigma_p^{\text{cv}}(\omega) + \Delta \Sigma_p(\omega) \quad (5.106)$$

The first term $\Sigma_p^{\text{cv}}(\omega)$ depends only on control-variate functions and is evaluated analytically.

$$\Sigma_p^{\text{cv}}(\omega) = 2 \sum_{iab}^{\boxtimes} \frac{V_{iapb}^{\text{cv}} V_{iapb}^{\text{cv}}}{E_{iab}^{2\text{p1h}}(\omega)} - \sum_{iab}^{\boxtimes} \frac{V_{iapb}^{\text{cv}} V_{ibpa}^{\text{cv}}}{E_{iab}^{2\text{p1h}}(\omega)} - 2 \sum_{ija}^{\boxtimes} \frac{V_{ipja}^{\text{cv}} V_{ipja}^{\text{cv}}}{E_{ija}^{1\text{p2h}}(\omega)} + \sum_{ija}^{\boxtimes} \frac{V_{ipja}^{\text{cv}} V_{iajp}^{\text{cv}}}{E_{ija}^{1\text{p2h}}(\omega)} \quad (5.107)$$

The second term contains the different terms and is defined as follows.

$$\begin{aligned} \Delta \Sigma_p(\omega) = & 2 \sum_{iab}^{\boxtimes} \frac{D_{iapb} V_{iapb}^{\text{cv}}}{E_{iab}^{2\text{p1h}}(\omega)} - \sum_{iab}^{\boxtimes} \frac{D_{iapb} V_{ibpa}^{\text{cv}}}{E_{iab}^{2\text{p1h}}(\omega)} - 2 \sum_{ija}^{\boxtimes} \frac{D_{ipja} V_{ipja}^{\text{cv}}}{E_{ija}^{1\text{p2h}}(\omega)} + \sum_{ija}^{\boxtimes} \frac{D_{ipja} V_{iajp}^{\text{cv}}}{E_{ija}^{1\text{p2h}}(\omega)} \\ & + 2 \sum_{iab}^{\boxtimes} \frac{V_{iapb}^{\text{cv}} D_{iapb}}{E_{iab}^{2\text{p1h}}(\omega)} - \sum_{iab}^{\boxtimes} \frac{V_{iapb}^{\text{cv}} D_{ibpa}}{E_{iab}^{2\text{p1h}}(\omega)} - 2 \sum_{ija}^{\boxtimes} \frac{V_{ipja}^{\text{cv}} D_{ipja}}{E_{ija}^{1\text{p2h}}(\omega)} + \sum_{ija}^{\boxtimes} \frac{V_{ipja}^{\text{cv}} D_{iajp}}{E_{ija}^{1\text{p2h}}(\omega)} \\ & + 2 \sum_{iab}^{\boxtimes} \frac{D_{iapb} D_{iapb}}{E_{iab}^{2\text{p1h}}(\omega)} - \sum_{iab}^{\boxtimes} \frac{D_{iapb} D_{ibpa}}{E_{iab}^{2\text{p1h}}(\omega)} - 2 \sum_{ija}^{\boxtimes} \frac{D_{ipja} D_{ipja}}{E_{ija}^{1\text{p2h}}(\omega)} + \sum_{ija}^{\boxtimes} \frac{D_{ipja} D_{iajp}}{E_{ija}^{1\text{p2h}}(\omega)} \end{aligned} \quad (5.108)$$

The single-shot determination of the self-energy operator is performed by evaluating the self-energy at the HOMO energy.

$$\omega_{\text{Koopmans}} = \epsilon_{\text{HOMO}} \quad (5.109)$$

$$\omega_{\text{one-shot}} = \epsilon_{\text{HOMO}} + \Sigma_p(\epsilon_{\text{HOMO}}) \quad (\text{with } \psi_p = \psi_{\text{HOMO}}) \quad (5.110)$$

The full iterative solution of the Dyson equation is obtained by evaluating $\Sigma_p(\omega)$ for a range of ω and then finding the point where,

$$\omega_{\text{iter}} = \epsilon_{\text{HOMO}} + \Sigma_p(\omega_{\text{iter}}) \quad (\text{with } \psi_p = \psi_{\text{HOMO}}) \quad (5.111)$$

The SSE-MO method allows for a third approximation for ω . We can solve the Dyson equation iteratively using $\Sigma_p^{\text{cv}}(\omega)$

$$\omega^* = \epsilon_{\text{HOMO}} + \Sigma_p^{\text{cv}}(\omega^*) \quad (\text{with } \psi_p = \psi_{\text{HOMO}}) \quad (5.112)$$

and then include the correction from $\Delta\Sigma_p$.

$$\omega_{\text{iter,cv}} = \epsilon_{\text{HOMO}} + \Sigma_p^{\text{cv}}(\omega^*) + \Delta\Sigma_p(\omega^*) \quad (\text{with } \psi_p = \psi_{\text{HOMO}}) \quad (5.113)$$

Calculation of Derivatives

The first derivative of the self-energy, with respect to ω , is useful for locating the poles of $\mathbf{G}(\omega)$, and is defined as follows.

$$\frac{d\Sigma_{pp}(\omega)}{d\omega} = -\frac{1}{2} \sum_{j,a,b} \frac{\langle ij||ab \rangle \langle ab||ij \rangle}{(\omega + \epsilon_j - \epsilon_a - \epsilon_b)^2} - \frac{1}{2} \sum_{a,j,k} \frac{\langle ia||jk \rangle \langle jk||ia \rangle}{(\omega + \epsilon_a - \epsilon_j - \epsilon_k)^2}. \quad (5.114)$$

The higher-order derivatives of the self-energy operator can then be obtained from the higher-order powers of the denominator.

$$\frac{d^n}{dx^n} \left[\frac{1}{E_{iab}^{2p1h}(\omega)} \right] = \frac{(-1)^n n!}{(\omega + \epsilon_i - \epsilon_a - \epsilon_b)^{n+1}} \quad (5.115)$$

$$\frac{d^n}{dx^n} \left[\frac{1}{E_{ija}^{1p2h}(\omega)} \right] = \frac{n!}{(\epsilon_i + \epsilon_j - \omega - \epsilon_a)^{n+1}} \quad (5.116)$$

In the SSE-MO method, the derivative of Σ_p is obtained by replacing the energy denominator with the higher powers of the denominator,

$$\frac{1}{E_{iab}^{2p1h}(\omega)} \longrightarrow \frac{(-1)^n n!}{(\omega + \epsilon_i - \epsilon_a - \epsilon_b)^{n+1}} \quad (5.117)$$

$$\frac{1}{E_{ija}^{1p2h}(\omega)} \longrightarrow \frac{n!}{(\epsilon_i + \epsilon_j - \omega - \epsilon_a)^{n+1}} \quad (5.118)$$

The contributions from Σ_p^{cv} are obtained analytically, and the contributions from the $\Delta\Sigma_p$ are obtained from the stochastic enumeration procedure described above. Because the derivative does not impact r_{12}^{-1} , which is present in expression for the self-energy, the calculation of the derivatives can be performed concurrently while the calculation of $\Delta\Sigma_p$ is being performed. This approach was used for the construction of the spectral function and is presented in [Table 5.4](#).

Computational Details

The SSE-MO method was applied in order to investigate the ionization potentials of PbS and CdS QDs. In addition, benchmark calculations for Ne, H₂O, and CH₄ were also performed. The single-particle states and energies were obtained from HF calculations using the 6-31G* basis for Ne, H₂O, and CH₄ and the LANL-2DZ ECP basis for the quantum dots. These HF calculations were performed using the TERACHEM electronic structure package. The SSE-MO calculations were performed by dividing the MO-index space into N_{occ} number of segments. The 6D Cartesian space was divided into 100 non-overlapping regions. A total of $N_{\text{sample}} \sim 10^9$ sampling points were used for calculating the self-energy at each value of ω and the sampling points were distributed using the stratification strategy described earlier. We used the relative standard deviation, σ_{rel} , also known as coefficient of variance for defining the convergence criteria for the calculated IPs (Equation 5.119).

$$\sigma_{\text{rel}} = \frac{\sigma}{\mu} \quad (5.119)$$

In this work, we enforced $\sigma_{\text{rel}} < 10^{-2}$ to be the criteria for convergence for each segment.

5.4 Results

10-electron System

For benchmarking and testing, the SSE-MO method was used to calculate the IPs of Ne, H₂O, and CH₄. The results for these chemical systems are presented in Table 5.1. The IPs were calculated using both single-shot and iterative solution of the Dyson equation and the results between the two approaches were found to be very similar with a maximum difference of 0.17 eV. In all cases, the SSE-MO results were found to be in good agreement with the previously reported results. For CH₄ and H₂O, the IPs obtained using the SSE-MO method were compared to IPs calculated using the MC-MP2 method. The MC-MP2 method is a stochastic method which has been used to construct the self-energy operator. [123] Since the SSE-MO method is also a stochastic method, when possible, it would be ideal to compare the IPs obtained from the SSE-MO method to another stochastic method. The IP of Ne obtained using the SSE-MO method was compared to an IP value obtained from a conventional MP2 calculation. [50] Additionally, the IPs of the 10-electron systems, obtained using the SSE-MO method, were compared to IPs calculated using the IP-EOM-CCSD(T) method. This comparison was made because IP-EOM-CCSD(T) is a highly accurate method and is generally considered to be the gold standard for testing the accuracy of IPs obtained from newly developed first-principles quantum chemistry methods. [96]

Table 5.1: Ionization potentials (eV) of ten electron systems: comparison with benchmark literature values

System	Koopmans'	Single-shot solution	Iterative solution	Lit. value	IP-EOM-CCSD(T)[50]
CH ₄	14.86	13.94 ±0.03	13.95 ±0.03	13.91	12.76
Ne	22.59	21.47 ±0.06	21.38 ±0.07	21.13	20.98
H ₂ O	13.56	10.44 ±0.13	10.61 ±0.08	10.74	11.37

Ionization Potential of PbS and CdS Quantum Dots

The SSE-MO method was applied for calculating the IPs of Pb_4S_4 , $\text{Pb}_{44}\text{S}_{44}$, $\text{Pb}_{140}\text{S}_{140}$, Cd_6S_6 , $\text{Cd}_{24}\text{S}_{24}$, and $\text{Cd}_{45}\text{S}_{45}$, by way of both single-shot and iterative solution of the Dyson equation. The IPs from the single-shot solution and from the iterative solution of the Dyson equation are presented in Table 5.2 and Table 5.3, respectively. We note that the calculated IPs are vertical ionization potentials and do not include contributions from the quantum mechanical treatment of nuclear degrees of freedom. Figure 5.2 illustrates the graphical verification of the self-consistency of the iterative procedure for $\text{Pb}_{140}\text{S}_{140}$. We observe that the curve for $\Sigma(\omega) + \omega_0$ versus ω intersects with the curve for ω versus ω at that the value of ω for which the diagonal approximation to the Dyson equation converges. To highlight the efficiency of the SSE-MO method, the computational time associated with the use of the SSE-MO method, which employs stratified stochastic enumeration for summation, is compared to the estimated computational time for constructing the self-energy, using sequential enumeration. This comparison is presented for the PbS systems in Table 5.4.

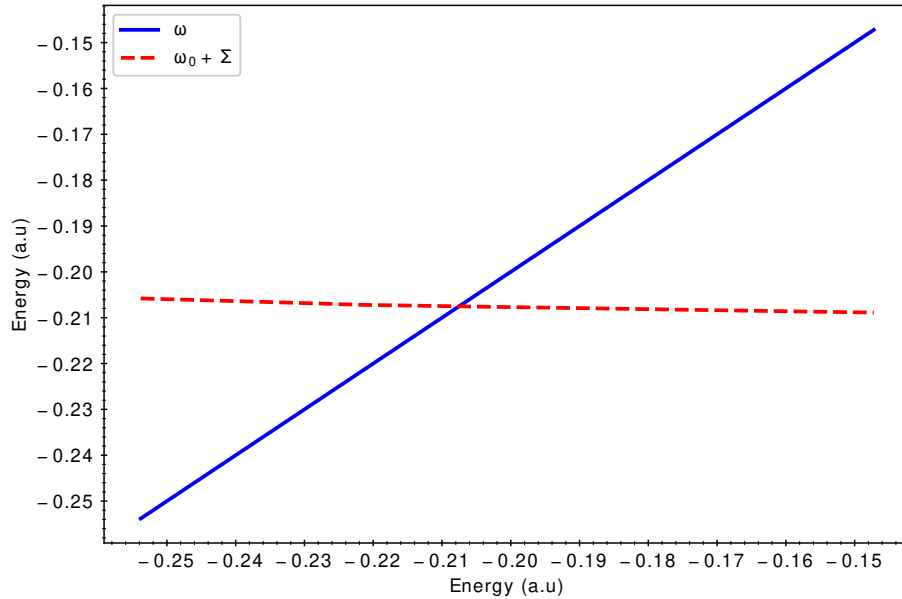


Figure 5.2: Curve labeled ω intersects with the curve labeled $\omega_0 + \Sigma$ at the value of ω for which the diagonal approximation to the Dyson equation converges, for $\text{Pb}_{140}\text{S}_{140}$.

The frequency dependence of the 1-particle Green's function was evaluated near the poles and is presented in Figure 5.3, Figure 5.4, and Figure 5.5.

When compared to $G_0(\omega)$, the poles of $G(\omega)$ were found to have higher values of ω indicating that for these systems, inclusion of electron correlation effects resulted in a lower IP than Koopmans' IP values. Comparison between G and G_0 shows that inclusion of electron correlation in IPs becomes more important for larger dots. Comparison between the single-shot versus iterative solution of Dyson equation also exhibits similar trends, where the need for iterative solutions become more important for larger dots. Upon examination of Table 5.2 and Table 5.3, it can

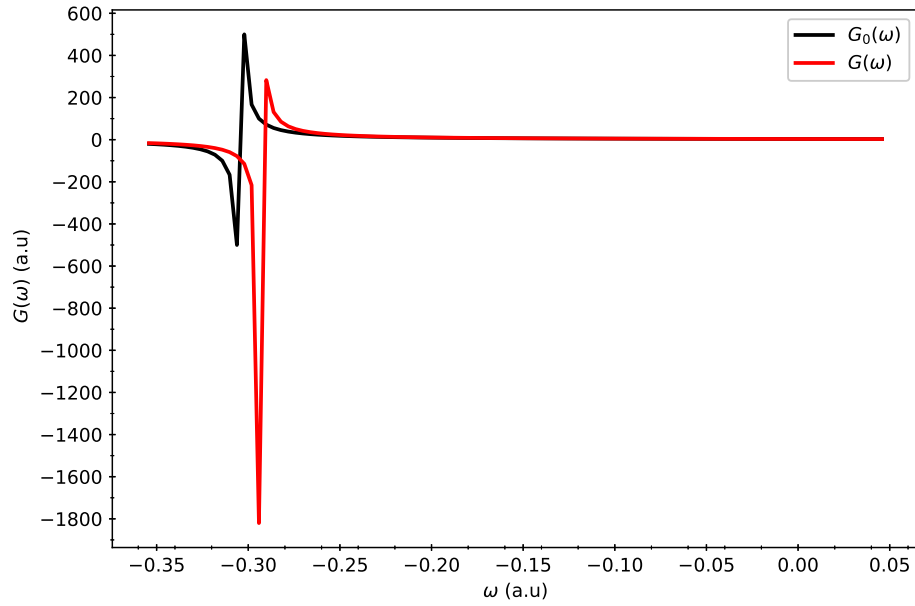


Figure 5.3: Poles of $G_0(\omega)$ and $G(\omega)$ for Pb_4S_4 .

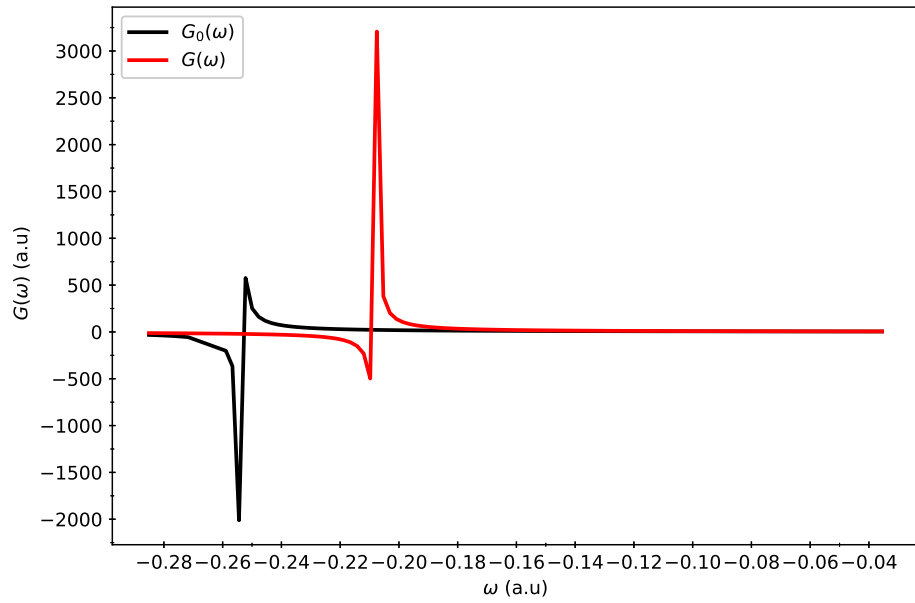


Figure 5.4: Poles of $G_0(\omega)$ and $G(\omega)$ for $\text{Pb}_{44}\text{S}_{44}$.

be observed for both the single-shot and iterative solution of the Dyson equation, the ionization potentials of the PbS dots monotonically decrease with increasing dot size. This particular trend in the IPs with respect to dot size is generally expected. [74] In contrast, for the CdS dots, the trend in IP with respect to dot size was observed to be non-monotonic. Although the optical and

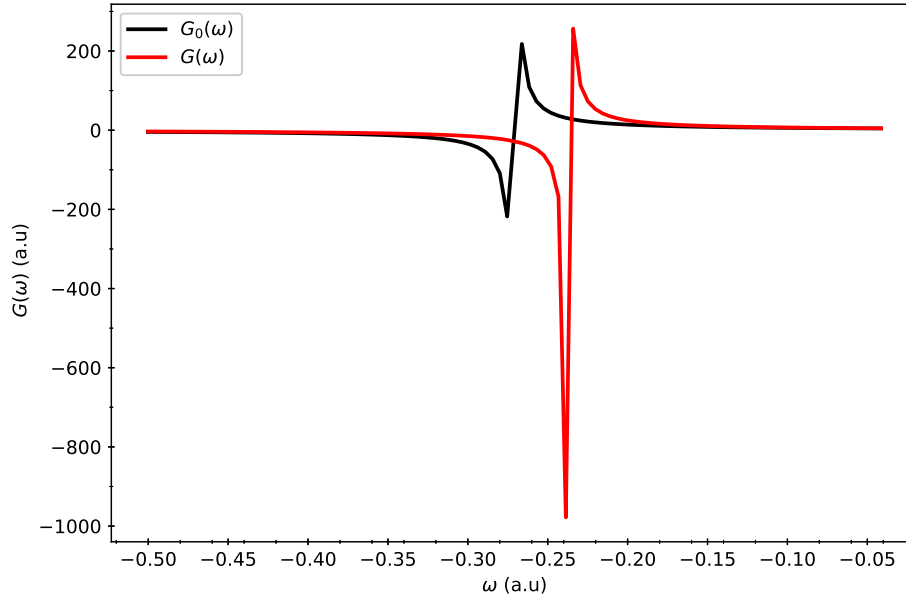


Figure 5.5: Poles of $G_0(\omega)$ and $G(\omega)$ for $\text{Pb}_{140}\text{S}_{140}$.

Table 5.2: Self-energy and Ionization Potentials (eV) of PbS and CdS Quantum Dots from Single-shot Solution

System	Koopmans'	Self-energy from single-shot solution	IP from single-shot solution
Pb_4S_4	8.28	0.65	7.63 ± 0.05
$\text{Pb}_{44}\text{S}_{44}$	7.13	0.22	6.91 ± 0.04
$\text{Pb}_{140}\text{S}_{140}$	6.91	0.09	6.82 ± 0.05
Cd_6S_6	5.25	0.42	4.837 ± 0.04
$\text{Cd}_{24}\text{S}_{24}$	6.25	0.09	$6.16 \pm \epsilon < 0.01$
$\text{Cd}_{45}\text{S}_{45}$	6.09	0.23	5.86 ± 0.02

electronic properties of quantum dots are often thought to display well-defined monotonic trends with respect to system size, these trends may not always be purely monotonic. For example, it has been demonstrated that the first excitation energies of CdS quantum dots may not always display a purely monotonic trend, with respect to dot size. [73]

For each PbS system, the required computational time for the construction of the self-energy, using sequential enumeration (Table 5.4), was estimated using the time required for the evaluation and summation of the first 1000 terms of both 2p1h and 1p2h components of the self-energy for Pb_4S_4 . In general, the estimated time ($t_2^{2\text{p1h}}$) required for constructing the 2p1h term of a given system can be calculated as given below in Equation 5.120.

$$t_2^{2\text{p1h}} = N_2^{2\text{p1h}} \times \left(\frac{t_1^{2\text{p1h}}}{N_1^{2\text{p1h}}} \right) \quad (5.120)$$

Table 5.3: Self-energy and Ionization Potentials (eV) of PbS and CdS Quantum Dots from Iterative Solution

System	Koopmans'	Self-energy from iterative solution	IP from iterative solution
Pb ₄ S ₄	8.28	0.61	7.66 ± 0.01
Pb ₄₄ S ₄₄	7.13	0.17	6.96 ± 0.01
Pb ₁₄₀ S ₁₄₀	6.91	0.28	6.71 ± 0.08
Cd ₆ S ₆	5.25	0.41	4.84 ± 0.01
Cd ₂₄ S ₂₄	6.25	0.08	6.16 ± ϵ < 0.01
Cd ₄₅ S ₄₅	6.09	0.22	5.87 ± 0.01

Table 5.4: Computational time for constructing self-energy: SSE-MO vs. Sequential Enumeration

System	Sequential enumeration time	SSE-MO time
Pb ₄ S ₄	1.07 hours	1.96 minutes
Pb ₄₄ S ₄₄	59.24 days	17.04 minutes
Pb ₁₄₀ S ₁₄₀	1438.24 days	66.93 minutes

In Equation 5.120, N_1^{2p1h} represents the number of terms of the 2p1h component of the self-energy for Pb₄S₄, which were evaluated and subsequently summed, using sequential enumeration. In this work, N_1^{2p1h} was chosen to be equal to 1000, which accounts for the terms of the 2p1h component of the self-energy for the MO-indices $j = 1, \dots, 10$ and $a, b = 1, \dots, 10$. N_2^{2p1h} represents the total number of terms that would need to be evaluated and then summed when constructing the 2p1h term of the self-energy for any given system, using sequential enumeration. In this work, t_1^{2p1h} represents the time that was required to evaluate and then sum the first 1000 terms of the 2p1h component of the self-energy for Pb₄S₄. t_2^{2p1h} represents the estimated time required for the construction of the 2p1h term, using sequential enumeration, for any given system.

In the second column of Table 5.4, the sequential enumeration time represents the estimated computational time required for the construction of the total self energy (2p1h + 1p2h), using sequential enumeration. The SSE-MO time is the measured computational time required for the construction of the total self energy, using the SSE-MO method, which employs stratified stochastic enumeration. Upon examination of Table 5.4 it can be observed that the use of the SSE-MO method results in a drastic decrease in the computational time for construction of the self-energy for all of the PbS systems investigated. It is relevant to point out that due to the adaptive nature of the SSE-MO method, the efficiency of the method is independent of the system investigated.

Single-pole Approximation to the Spectral Function

We define the single-pole approximation to the spectral function as,

$$A_{sp}(\omega) = \frac{\text{Im}\Sigma(\omega)}{(\omega - \epsilon_p)^2 + (\text{Im}\Sigma(\omega))^2} \quad (5.121)$$

where the subscript ‘sp’ in A_{sp} denotes that we are looking at the form of the spectral function near the pole ($\omega = \epsilon_p$). The imaginary part of the self-energy operator can be approximated from the first derivative of the self-energy, with respect to ω , as described in Equation 5.3. For example, the imaginary part of the following quantity $I(\omega)$,

$$I(\omega) = \sum_n \frac{x_n}{y_n(\omega) + ib} = \sum_n \frac{x_n(y_b - ib)}{y_n^2(\omega) + b^2} \quad (5.122)$$

is given by,

$$\text{Im}[I(\omega)] = -b \sum_n \frac{x_n}{y_n^2(\omega) + b^2} \quad (5.123)$$

In Figure 5.6, the ratio A_{wp}/A_{wp}^{\max} is plotted as a function of $\omega/\omega_{\text{opt}}$ for the three PbS QDs. The

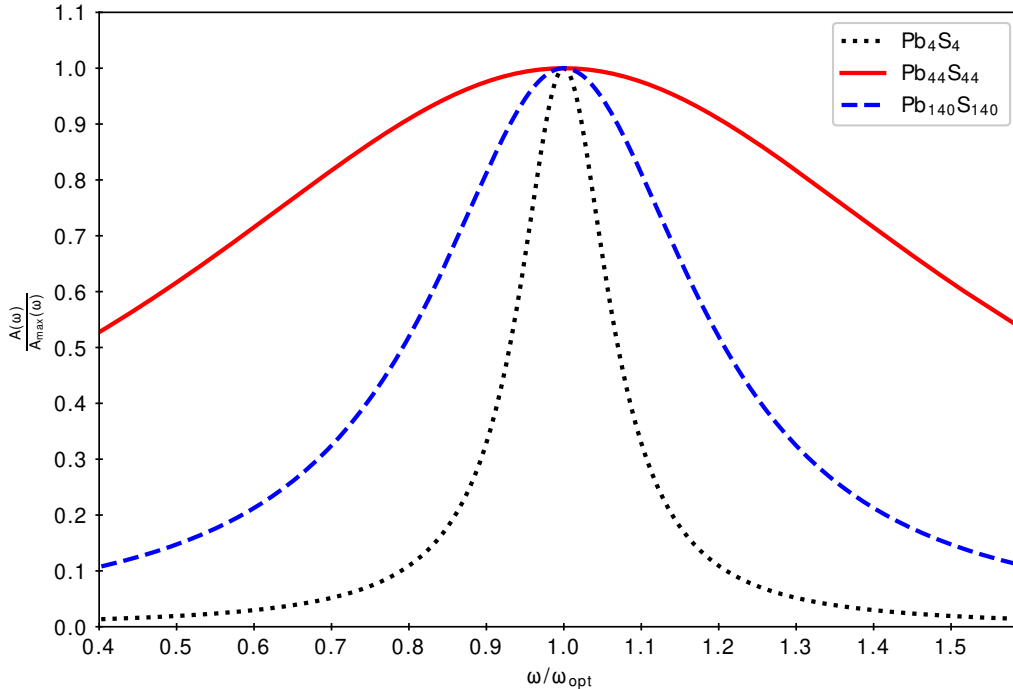


Figure 5.6: A_{wp}/A_{wp}^{\max} (ordinate) plotted as a function of $\omega/\omega_{\text{opt}}$ (abscissa) for PbS systems. A_{wp}/A_{wp}^{\max} is the ratio of $A_{sp}(\omega)$ and the maximum value of $A_{sp}(\omega)$. ω_{opt} is the value of ω at which diagonal approximation to the Dyson equation converges.

linewidth of the plot was found to be narrowest for the Pb4S4 and broadest for Pb44S44. This feature indicates that the relative lifetime of the quasi-hole in (Pb4S4) is longer than the other dots in the series. Similar analysis for the CdS QDs in Figure 5.7 revealed that the line-width is smallest for Cd₂₄S₂₄. decreases with increasing dot size. The results from the spectral analysis highlight the importance of including frequency dependency in the self-energy operator. The plots also demonstrate the impact of many-body correlations in these systems. Specifically, in the absence of electron-electron correlation, the limit $\sigma \rightarrow 0$ will reduce the plots to a Dirac delta function.

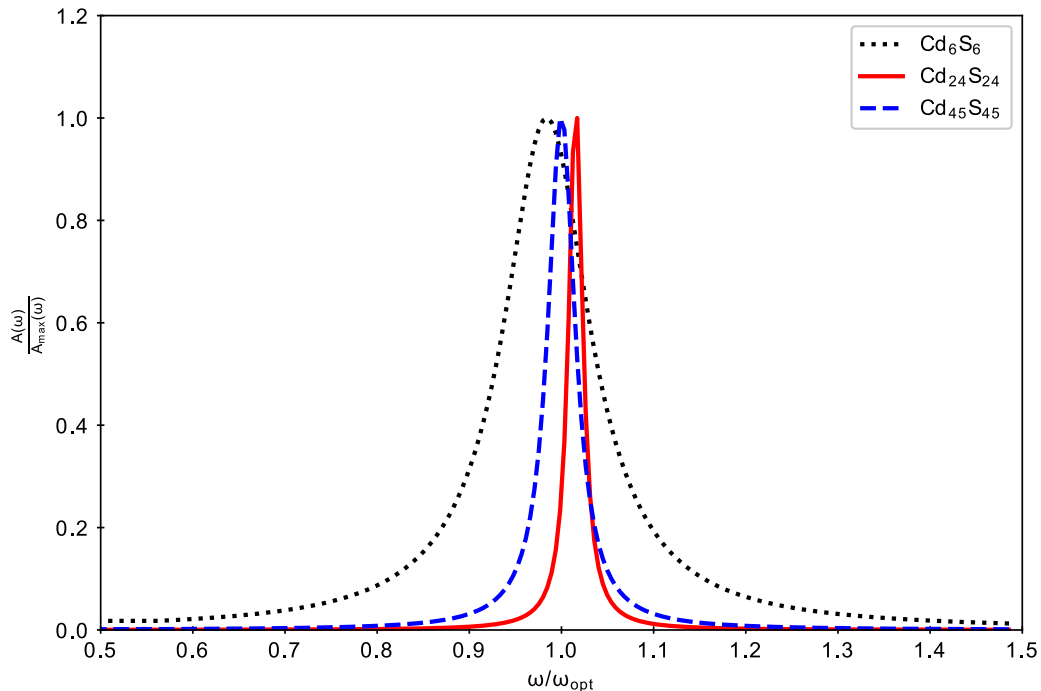


Figure 5.7: $A_{\text{wp}}/A_{\text{wp}}^{\text{max}}$ (ordinate) plotted as a function of $\omega/\omega_{\text{opt}}$ (abscissa) for CdS systems. $A_{\text{wp}}/A_{\text{wp}}^{\text{max}}$ is the ratio of $A_{\text{sp}}(\omega)$ and the maximum value of $A_{\text{sp}}(\omega)$. ω_{opt} is the value of ω at which diagonal approximation to the Dyson equation converges.

5.5 Discussion

Correlated Sampling in the Combined Cartesian and Molecular Orbital Index Space

The main philosophy of the SSE-MO method is to perform correlated sampling in a joint real-space and occupation-number space (Table 5.5). Assuming a discretization of 100 points per Cartesian coordinate, the total number of points needed for exhaustive sampling is in the range of $10^{16} - 10^{20}$ as shown in Table 5.5. However, not all spatial components of all the molecular orbitals contribute equally and uniformly to the calculation of the self-energy. There are certain combinations of MOs whose form in specific regions of the Cartesian space correlate strongly with the error in the self-energy calculations. Through the use of a two-step stratified sampling scheme in both Cartesian and MO space, the SSE-MO method provides a systematic and adaptive procedure to identify the important contributors. We have used a combination of ratio estimator, control-variate, and stratified sampling techniques for the efficient and accurate evaluation of the MO integrals. The key quantity that implements and controls this concept is the $N_{\text{sample}}^{\text{space}, \text{M}, \text{pqst}}$ term. This term represents the number of spatial sampling points for the Mth spatial segment for the correction term D_{pqrs} associated with indices p, q, r, s and depends on both the spatial and MO indices. The total

Table 5.5: Total number of sampling points in the combined MO-Cartesian space assuming 100 points per Cartesian coordinate.

System	N_{2p1h}	N_{1p2h}	N_{space}^{MO}	$N_{space}^{MO} \times N_{space}^{6D}$
Pb ₄ S ₄	3.87×10^4	1.76×10^4	5.63×10^4	5.63×10^{16}
Pb ₄₄ S ₄₄	5.15×10^7	2.34×10^7	7.50×10^7	7.50×10^{19}
Pb ₁₄₀ S ₁₄₀	1.18×10^9	6.37×10^8	1.82×10^9	1.82×10^{21}
Cd ₆ S ₆	7.02×10^5	3.32×10^5	1.03×10^6	1.03×10^{18}
Cd ₂₄ S ₂₄	4.50×10^7	2.13×10^7	6.62×10^7	6.62×10^{19}
Cd ₄₅ S ₄₅	2.96×10^8	1.40×10^8	4.36×10^8	4.36×10^{20}

number of sampling points is given by the following expression.

$$N_{sample}^{total} = \sum_{M=1}^{N_{seg}^{MO}} \sum_{L=1}^{N_{seg}^{space}} N_{sample}^{MO,M} \times N_{sample}^{space,M,L} \approx 10^9 \quad (5.124)$$

As shown in Equation 5.103, this number was directly obtained from the variance of the integral kernel, which also includes the contribution from the r_{12}^{-1} operator. Note that these sampling points were not used to evaluate the full r12-integral kernel, but instead were used to evaluate only the component of the full r12-integral kernel not included in the control-variate expression. The Cartesian space sampling for each spatial segment was performed using simple Monte Carlo sampling. This process can be enhanced by using low-discrepancy random numbers, which is a quasi-Monte Carlo approach. We expect that using the quasi-Monte Carlo approach will accelerate the overall calculation process.

Segment-based Analysis of Sampling Error

The error in the calculated IP using the SSE-MO method originates from the sampling error associated with sampling the integral kernel in the combined Cartesian-MO space. However, not all segments contribute equally to the numerical error. The goal of SSE-MO is to distribute the computational effort in proportion to the contributions from each segment. One insight generated from the SSE-MO calculation is information about the contribution of each segment to the total self-energy operator. We define the cumulative percent contribution for the segments as,

$$C(M) = 100 \times \frac{\sum_{i=1}^M S(i)}{\sum_{i=1}^{N_{seg}} S(i)} \quad (5.125)$$

where $S(i)$ is the contribution to the self-energy for each segment. The cumulative percent contribution of the segments to the total self-energy operator is denoted as $C(M)$ and is presented for the PbS and CdS quantum dots in Figure 5.8 and Figure 5.9, respectively. Analysis of the results revealed that the 2p1h and 1p2h terms show very different behavior. In all cases it was found that only few segments, typically ≤ 50 , had significant contributions to the 1p2h component of the self-energy operator. In contrast, for the 2p1h component, the cumulative sum of the percent

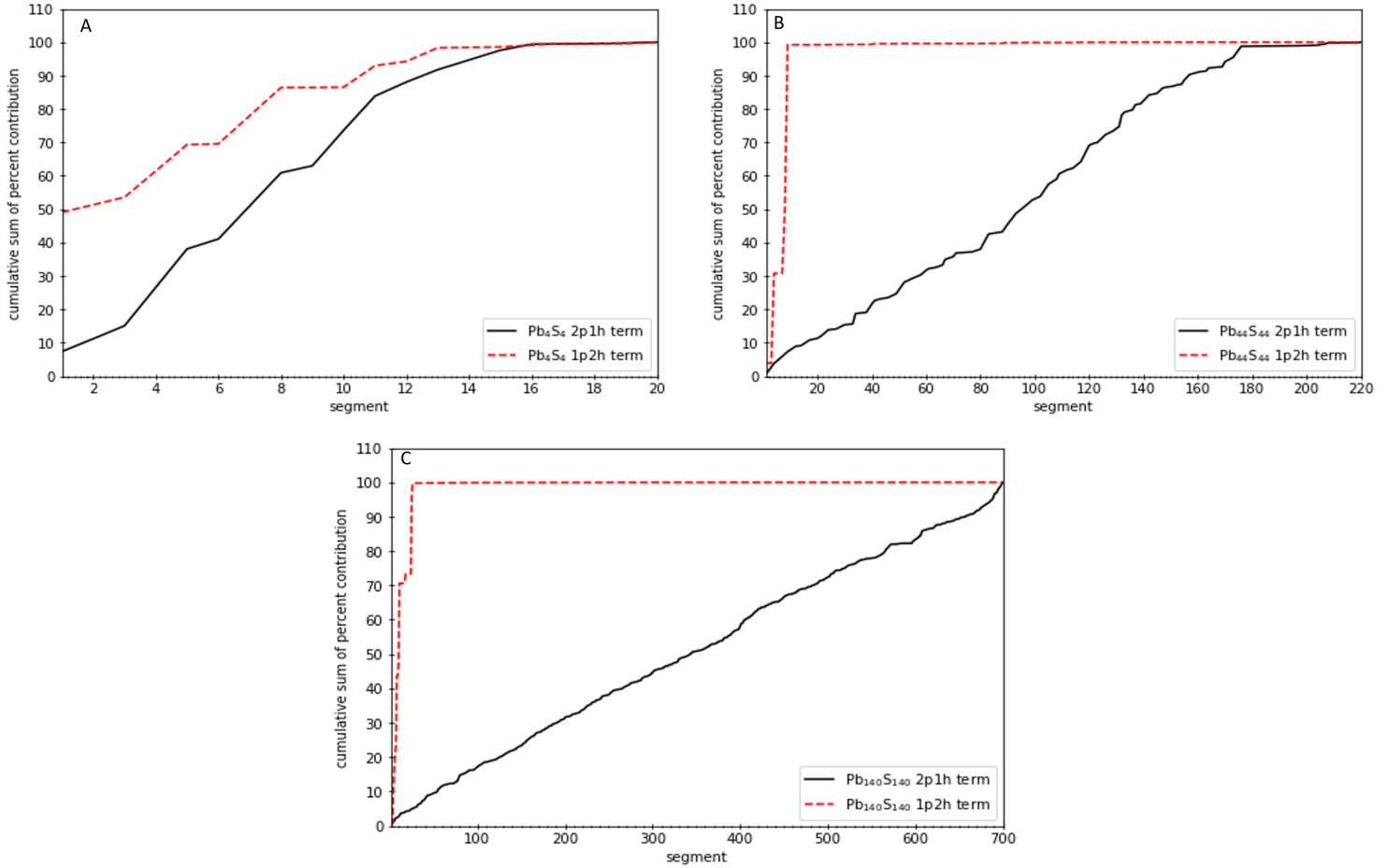


Figure 5.8: Cumulative sum of the percent contributions of the segments composing the sample space for the 2p1h and 1p2h terms of the self-energy (ordinate) versus the segment index (abscissa) for Pb₄S₄ (Figure A), Pb₄₄S₄₄ (Figure B), and Pb₁₄₀S₁₄₀ (Figure C).

contribution increased in a much more gradual manner. The distributions of the standard deviations associated with the segments for the 2p1h and 1p2h terms of the self-energy for the two largest quantum dots, (Pb₁₄₀S₁₄₀ and Cd₄₅S₄₅), are presented in Figure 5.10 and Figure 5.11, respectively. Analysis of the distributions reveals that the sampling error in the 2p1h term is significantly smaller than the sampling error in the 1p2h term for the two largest quantum dots. These plots also show that the overall sampling error in the calculated IP is dominated by the sampling error in the 1p2h term. The advantage of the SSE-MO method is that, by construction, the SSE-MO scheme is able to extract this information dynamically during the course of the calculation and then allocate more sampling points to segments that have high sampling errors. Because SSE-MO is based on stratified sampling, the conventional stratified sampling error analysis[109] is applicable for the sampling

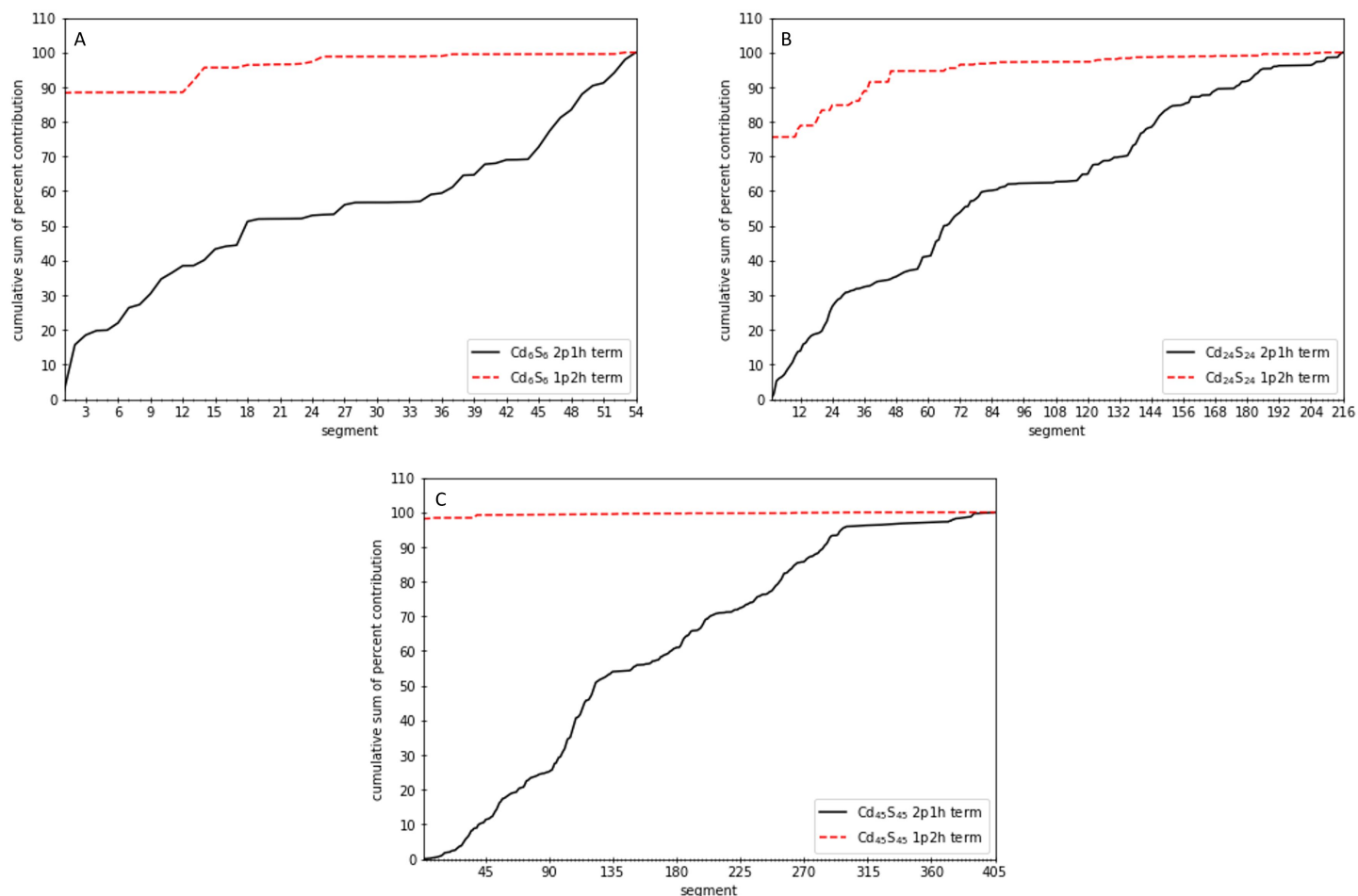


Figure 5.9: Cumulative sum of the percent contributions of the segments composing the sample space for the 2p1h and 1p2h terms of the self-energy (ordinate) versus the segment index (abscissa) for Cd_6S_6 (Figure A), $\text{Cd}_{24}\text{S}_{24}$ (Figure B), and $\text{Cd}_{45}\text{S}_{45}$ (Figure C).

error in the IP calculations. In addition to this segment-based analysis, the overall sampling error in the calculated IPs as a function of the number of sampling points used to construct the self-energy for $\text{Pb}_{140}\text{S}_{140}$ quantum dot is presented in [Figure 5.12](#).

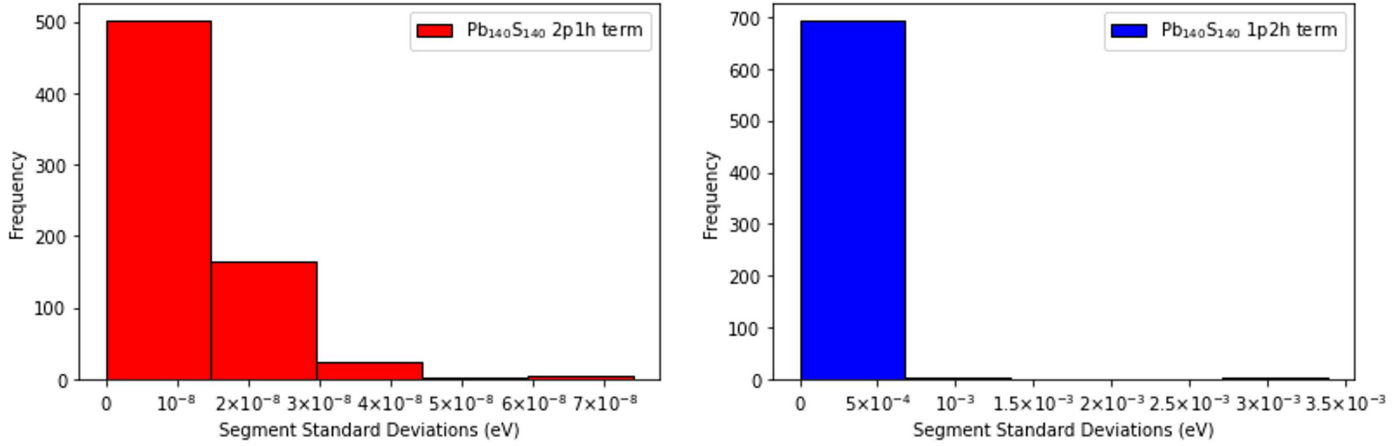


Figure 5.10: Frequency distributions of the standard deviations (units of eV) for the segments that compose the sample space of the 2p1h and 1p2h terms of the self-energy operator for Pb₁₄₀S₁₄₀.

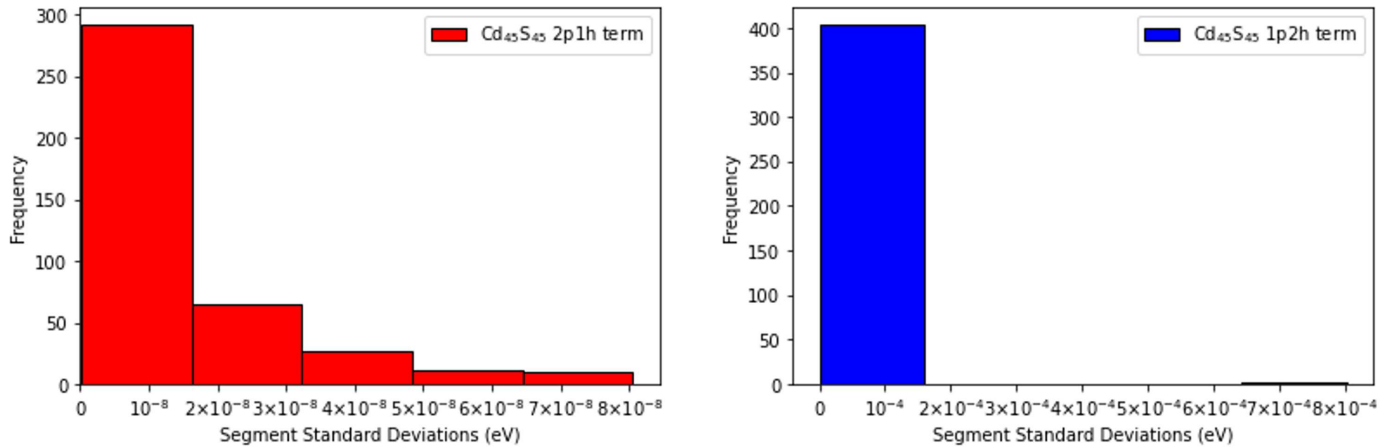


Figure 5.11: Frequency distributions of the standard deviations (units of eV) for the segments that compose the sample space of the 2p1h and 1p2h terms of the self-energy operator for Cd₄₅S₄₅.

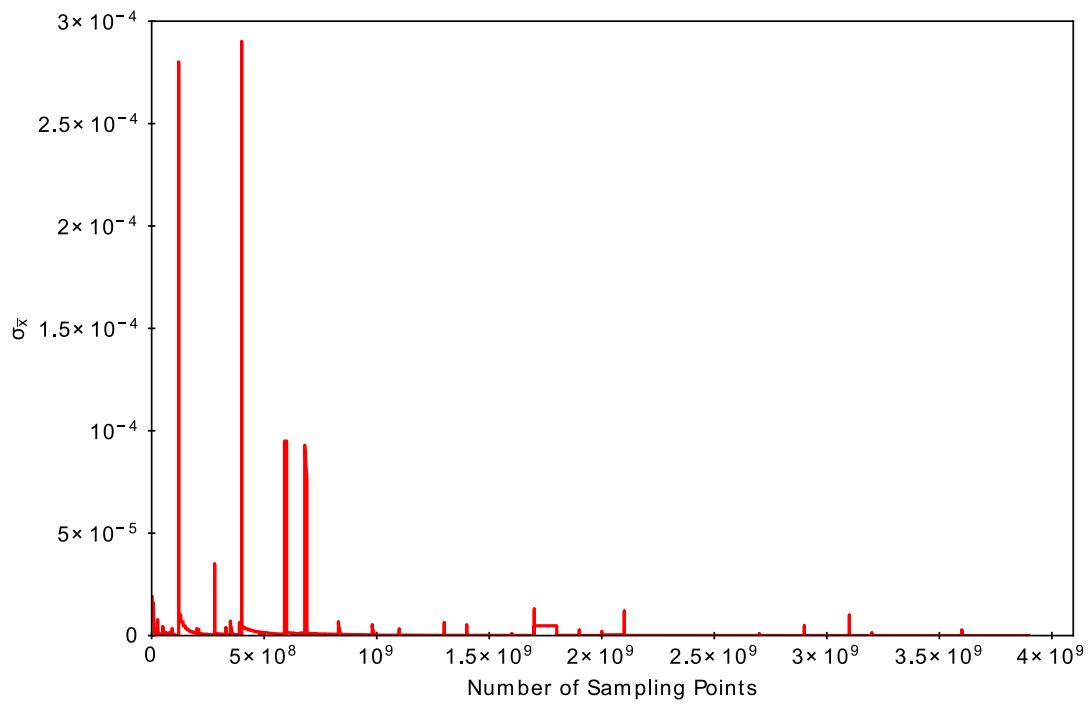


Figure 5.12: Sample standard deviation ($\sigma_{\bar{x}}$) in ionization potential (units of eV) versus the number of sampling points used to construct the self-energy for $\text{Pb}_{140}\text{S}_{140}$.

Connection with Diagrammatic Monte Carlo

The SSE-MO method is conceptually similar to diagrammatic MC (diagMC), where terms are evaluated stochastically. However, there are key differences between the two methods. SSE-MO is not diagram-based and the relative importance of the terms are not evaluated using topological connectivity of the vertices. Also, the SSE-MO method uses stratified sampling as opposed to importance sampling, where emphasis is placed on reducing numerical error through variance minimization and numerical effort is predominantly spent on computing the correction term to the self-energy operator. As an intrinsically adaptive approach, the calculation puts more points where they are needed in order to achieve reduction of numerical error.

Comparison with Laplace-transformed approach: The SSE-MO method does not perform Laplace-transformation, but instead relies on stochastic enumeration to reduce the computational cost. Consequently, only 3D and 6D spatial integrals are solved numerically. As a consequence, higher-order derivatives of the self-energy operator ($d^n \Sigma / d\omega^n$) can be obtained with relative ease and with very little additional computational cost during the self-energy calculation. This not only allows for calculation of the imaginary component of the self-energy operator, but also open doors for iterative solution of the Dyson equation by Taylor-series expansion of the self-energy operator.

$$\omega_p^0 + \Sigma(\omega_p^0) + \left(\frac{\partial \Sigma(\omega)}{\partial \omega} \right)_{\omega_p^0} (\omega - \omega_p^0) + \left(\frac{\partial^2 \Sigma(\omega)}{\partial \omega^2} \right)_{\omega_p^0} (\omega - \omega_p^0)^2 + \dots = \omega \quad (5.126)$$

Because we are not using a Laplace transformation, the SSE-MO method is well-suited to extending the self-energy calculation to $\Sigma^{(3)}$, using the P3 correction developed by Ortiz and co-workers.[88] For example, the Laplace transformation of the following term in the P3 expression

$$\sum_{abcij} \frac{\langle pa||ij \rangle \langle qa||bc \rangle \langle bc||ij \rangle}{(\omega + \epsilon_a - \epsilon_i - \epsilon_j)(\epsilon_i + \epsilon_j - \epsilon_b - \epsilon_c)} = \int d\mathbf{r}_1 \dots d\mathbf{r}_6 \int dt dt' K(x_1, y_1, z_1, \dots, x_6, y_6, z_6, t, t') \quad (5.127)$$

will involve the Monte Carlo numerical integration of a 20-dimensional integral. In the SSE-MO implementation, the dimensionality of the spatial integral will still be six and the MO index will be sampled from the 3p-2h space.

$$\sum_{abcij} \approx \sum_{\mathbf{k}} \quad \text{with} \quad \mathbf{k} \in \{N_{\text{vir}}^3 \times N_{\text{occ}}^2\} \quad (5.128)$$

Equation 5.128 can be viewed as the stochastic tensor contraction over the MO indices and can potentially be applied to other branches of quantum mechanics.

Selection of Control-variate Functions

The use of moment-based fitting ensures that the integral of the Mth-order multinomial comes out to be exact. For this work, a maximum of two Gaussian functions were used and was found to be adequate. For more challenging systems, the number of Gaussian functions can be systematically increased. In addition, metrics other than the moments can be used as criteria for the selection of the Gaussian functions. The choice of the control-variate functions is not restricted to Gaussian functions. For QDs, it is possible to take advantage of the approximate spherical symmetry of

the system and construct the control-variate functions from the hydrogenic wavefunctions with effective hole and particle masses.

$$\psi_i^{\text{cv}}(\mathbf{r}) = R_{nl}(r, \mu_{\text{eff}}^{\text{hole}}) Y_{lm}(\theta, \phi) \quad \text{for hole states} \quad (5.129)$$

$$\psi_a^{\text{cv}}(\mathbf{r}) = R_{nl}(r, \mu_{\text{eff}}^{\text{elec}}) Y_{lm}(\theta, \phi) \quad \text{for particle states} \quad (5.130)$$

Although both density fitting[53] and the control variate schemes use Gaussian functions, their purpose and implementation are very different. When using the control variate scheme, the goal is to reduce numerical error. When using density fitting, the goal is to approximate it. Specifically in the control variate, the integral of f_{pq} is expressed as:

$$\text{Control variate: } \langle f_{pq} \rangle = \alpha \langle f_{pq}^0 \rangle + \langle (f_{pq} - \alpha f_{pq}^0) \rangle \quad (5.131)$$

$$\langle f_{pq}^0 \rangle \rightarrow \text{Calculate analytically} \quad (5.132)$$

$$\langle (f_{pq} - \alpha f_{pq}^0) \rangle \rightarrow \text{Calculate numerically} \quad (5.133)$$

$$\text{Density fitting: } \langle f_{pq} \rangle \approx \langle f_{pq}^0 \rangle \quad (5.134)$$

There are two main differences between control variate and density fitting:

1. When using the control variate scheme, the error in fitting the integral is always calculated. The error in the estimation of the integral comes from the numerical approximation to the analytical fitting error. If we were to replace the numerical integral, $\langle (f - f_0) \rangle$, by an analytical integral, we would recover the exact integral. The origin of error in density fitting comes from the finite expansion of the auxiliary basis. While in the control variate the error is from the numerical approximation to the residue-error integral, $\langle (f - f_0) \rangle$.

$$\langle (f - f_0) \rangle_{\text{analytical}} \approx \langle (f - f_0) \rangle_{\text{MonteCarlo}} \quad (5.135)$$

2. Unlike density-fitting's attribute of fit-once-use-everywhere, the control variate approach is kernel dependent. This means that the integrals $\langle f_{pq} K_A \rangle$ and $\langle f_{pq} K_B \rangle$ will have different control variate parameters α_A and α_B , respectively. These parameters are obtained by minimizing the variance as shown below:

$$\min_{\alpha} \langle [(f_{pq} - \alpha f_{pq}^0) K_A]^2 \rangle \rightarrow \alpha_A \quad (5.136)$$

$$\min_{\alpha} \langle [(f_{pq} - \alpha f_{pq}^0) K_B]^2 \rangle \rightarrow \alpha_B \quad (5.137)$$

One approach to do the above integrals efficiently is to first expand the square term and then perform the α -independent integrals separately as shown below.

$$I_A(\alpha) = \langle [(f_{pq} - \alpha f_{pq}^0) K_A]^2 \rangle \quad (5.138)$$

$$= \alpha^2 \langle (f_{pq}^0 K_A)^2 \rangle + 2\alpha \langle f_{pq}^0 f_{pq} K_A^2 \rangle + \langle (f_{pq} K_A)^2 \rangle \quad (5.139)$$

5.6 Conclusions

This work presents the development and implementation of the stratified stochastic enumeration of molecular orbitals (SSE-MO) method for construction of the self-energy operator. The central idea of this method is to express the self-energy operator in a composite space, which is generated by combining the 3D Cartesian space of molecular orbitals with the discrete integer space of the molecular orbital indices. In conjunction, a stratified sampling Monte Carlo scheme was also developed for the efficient evaluation of the complex self-energy operator and its frequency derivatives. The SSE-MO method was applied to a series of CdS and PbS QDs, and the IPs of these QDs were obtained from both single-shot and iterative solution of the second order diagonal approximation to the Dyson equation. The results from these calculations showed that the IPs decreased with increasing dot size. The imaginary component of the self-energy operator was used to construct the single-pole frequency-dependent spectral functions of the quantum dots. The quantum dots with the longest relative lifetimes of the quasi-hole state were identified. Although it is known that the results obtained from calculations of the self-energy are basis set dependent[27, 22], the performance of the SSE-MO method itself is independent of the choice of basis set. The adaptive nature of the SSE-MO method enables the identification of the important contributors to the overall self-energy, in any given basis, and subsequently enables the optimal allocation of sampling effort, regardless of the size of the chosen basis set. The strategy of stochastic enumeration used in the SSE-MO method can also be interpreted in the broader context of stochastic tensor contraction methods and can be applied to other areas of quantum mechanics, where the sequential enumeration of summations is computationally prohibitive. [114]

Chapter 6

Background: Time-Dependent Schrödinger Equation and Time-dependent Perturbation Theory

6.1 Scope of Chapter Content

This chapter provides a basic introduction to first-order time-dependent perturbation theory (TDPT). Light-matter interactions are central to many chemically relevant processes, such as photoemission and inverse photoemission processes. Experimentally, processes involving light-matter interactions are often probed using spectroscopic techniques. It is relevant to mention that there are some non-trivial disadvantages when using experimental techniques for initial screening or identification of materials for specific applications of interest. For example, one of these disadvantages is that in order to investigate light-matter interaction induced processes in materials, the material must first either be procured or synthesized. Either the procurement or synthesis of the material can become inefficient, in terms of both monetary cost and time. This is especially true if many of the initially investigated materials prove to be ineffective or inadequate for the specific application of interest. Before introducing TDPT, the Time-dependent Schrödinger equation (TDSE) is discussed. From a theoretical perspective, TDPT is a very useful tool for formally describing light-matter interactions in chemical systems and materials.

6.2 Time-Dependent Schrödinger Equation

To begin this discussion about the TDSE, we will first consider the following time-independent Schrödinger equation (TISE).

$$H\psi_n = E_n\psi_n \quad (6.1)$$

In Equation 6.1, the Hamiltonian does not depend on time and is defined as follows.

$$H = H_0 + W \quad (6.2)$$

In Equation 6.2, W is a time-independent potential. Assume that we know the solutions to Equation 6.1. We will refer to these solutions as $\psi_n(t = 0)$.

Now consider the TDSE, which is given as follows.

$$i\hbar \frac{d}{dt} |\Psi(t)\rangle = H |\Psi(t)\rangle \quad (6.3)$$

Given that the solutions to Equation 6.2 are known, the solutions to Equation 6.3 can be expressed as follows.

$$|\Psi_n(t)\rangle = e^{-iE_n t/\hbar} |\psi_n(t=0)\rangle \quad (6.4)$$

Suppose that we are interested in determining the expectation value of some operator, A , for this time dependent state. This can be achieved as outlined in Equation 6.5.

$$A(t) = \langle \Psi_n(t) | A | \Psi_n(t) \rangle = \langle \Psi_n(0) | e^{+itE_n/\hbar} A e^{-itE_n/\hbar} | \Psi_n(0) \rangle = \langle \Psi_n(0) | A | \Psi_n(0) \rangle = A(0) \quad (6.5)$$

Although the solution provided in Equation 6.4 does indeed describe the time evolution of our system, upon examination of Equation 6.5 we observe that the expectation value of A does not depend on time. Therefore, the states, $\Psi_n(t)$, are referred to as stationary states. [107, 2]

6.3 Introduction to Time-dependent Perturbation Theory: First-Order

Consider the following time-dependent Hamiltonian.

$$H(t) = H_0 + W(t) \quad (6.6)$$

In Equation 6.6, $W(t)$ is a time-dependent potential and H_0 is time-independent and has known eigenfunctions and eigenvalues (ψ_n and E_n). We now write the TDSE as follows.

$$i\hbar \frac{d}{dt} |\Psi(t)\rangle = H(t) |\Psi(t)\rangle \quad (6.7)$$

Next we use Equation 6.4 to expand $\Psi(t)$ as follows.

$$|\Psi(t)\rangle = \sum_n b_n(t) e^{-iE_n t/\hbar} |\psi_n(t=0)\rangle = \sum_n b_n(t) e^{-iE_n t/\hbar} |\psi_n(0)\rangle \quad (6.8)$$

Note that in Equation 6.8, the coefficients, $b_n(t)$, are time dependent. Next, we substitute Equation 6.8 into Equation 6.7 and obtain the following.

$$i\hbar \frac{d}{dt} \sum_n b_n(t) e^{-iE_n t/\hbar} |\psi_n(0)\rangle = H(t) \sum_n b_n(t) e^{-iE_n t/\hbar} |\psi_n(0)\rangle \quad (6.9)$$

By substituting $H_0 + W(t)$ for $H(t)$ we obtain the following expression.

$$H_0 \sum_n b_n(t) e^{-iE_n t/\hbar} |\psi_n(0)\rangle + W(t) \sum_n b_n(t) e^{-iE_n t/\hbar} |\psi_n(0)\rangle = i\hbar \frac{d}{dt} \sum_n b_n(t) e^{-iE_n t/\hbar} |\psi_n(0)\rangle \quad (6.10)$$

Next, we left multiply by $\langle \psi_k(0) | e^{iE_k t/\hbar}$ and obtain the following.

$$E_k b_k(t) e^{-iE_k t/\hbar} + \sum_n b_n(t) e^{iE_k t/\hbar} e^{-iE_n t/\hbar} \langle \psi_k(0) | W(t) | \psi_n(0) \rangle = i\hbar \frac{d}{dt} b_k(t) e^{-iE_k t/\hbar} \quad (6.11)$$

By setting $\omega_{kn} = (E_k - E_n)/\hbar$ and taking the first derivative of the right-hand side of Equation 6.11 we observe following.

$$i\hbar \frac{d}{dt} b_k(t) = \sum_n b_n(t) e^{i\omega_{kn}t} W_{kn}(t) \quad (6.12)$$

In Equation 6.12, $W_{kn}(t)$ is defined as given below.

$$W_{kn}(t) = \langle \psi_k(0) | W(t) | \psi_n(0) \rangle \quad (6.13)$$

Let us assume that we know that at $t = 0$ the system is in some state, which we will denote as j . We will also assume that at time, t , the perturbation is small so that the change in the coefficients is negligible. At $t = 0$, these assumptions impose the following conditions on the coefficients. [107, 2]

$$b_j(t = 0) = b_j(0) = 1 \quad (6.14)$$

$$b_n(t = 0) = b_n(0) = 0 \quad \text{for } n \neq j \quad (6.15)$$

At time, t , the conditions imposed on the coefficients are as follows.

$$b_j(t) \simeq 1 \quad (6.16)$$

$$b_n(t) \simeq 0 \quad \text{for } n \neq j \quad (6.17)$$

By integrating both sides of Equation 6.12 from 0 to t and applying the above conditions, we can obtain $b_k(t)$ using the following expression. [107, 2]

$$b_k(t) - b_k(0) = \frac{1}{i\hbar} \int_0^t dt' e^{i\omega_{kj}t'} W_{kj}(t') \quad (6.18)$$

Since k is the final state of our system, we can set $b_k(0) = 0$ and re-write Equation 6.18 as follows.

$$b_k(t) = \frac{1}{i\hbar} \int_0^t dt' e^{i\omega_{kj}t'} W_{kj}(t') \quad (6.19)$$

The expression in Equation 6.19, provides the first-order approximation to the coefficients, $b_k(t)$, from time-dependent perturbation theory. Using Equation 6.19, the transition probability, for transition from the initial state (j) to the final state (k), can be obtained as follows. [107, 2]

$$P_{jk}(t) = |b_k(t)|^2 = \left| \frac{1}{i\hbar} \int_0^t dt' e^{i\omega_{kj}t'} W_{kj}(t') \right|^2 \quad (6.20)$$

It is important to highlight that the validity of Equation 6.18, Equation 6.19, and Equation 6.20 is contingent upon the assumption that the time-dependent perturbation, $W(t)$, is small. Additionally, within this frame-work, knowledge of the eigenfunctions and eigenvalues of H_0 is required. [107, 2]

Chapter 7

Enhancement of Spontaneous Photon Emission in Inverse Photoemission Transitions in Semiconductor Quantum Dots

7.1 Scope of Chapter Content

This chapter presents a computational and theoretical investigation into the inverse photoemission processes in a variety of quantum dots (CdS, CdSe, PbS, and PbSe). Inverse photoemission occurs when an incident electron is captured by a material in one of the high energy unoccupied states. This captured electron then subsequently de-excites to a lower energy unoccupied state, resulting in the emission of a photon. We investigated the inverse photoemission (IPE) processes in these dots, both in the absence of an external electric field and when the dots are in the presence of a Stark field. Furthermore, we studied the effect of field direction and magnitude on the inverse photoemission transition probabilities and the energies of the emitted photons. In order to construct the spectra for the CdS, CdSe, PbS, and PbSe dots, we combined the Frequency-Dependent Geminal-Screened interaction kernel method (FD-GSIK) [73] with time-dependent perturbation theory.

The reason we are interested in the inverse photoemission processes in quantum dots is because insight into the IPE processes in quantum dots can provide insight that is valuable for a variety of applications such as, the development of scintillators and for achieving a greater understanding of the surface chemistry of these materials by studying their unoccupied states. Additionally, investigation into the effect an external electric field on the IPE processes in these materials can provide important information that can aid in the identification of materials that are useful for electroluminescence applications and for the development of new highly controllable photon sources. It is essential to highlight that investigating the effects of the direction and magnitude of an external electric field on the IPE spectra of these materials can provide insight into information that can be used to systematically enhance the inverse photoemission processes in materials or alter the energy of the emitted photon. Here, we present evidence of field-induced enhancement of IPE intensities, field-dependent control of emitted photon frequencies, and enhancement of light-matter interaction using directed Stark fields.

7.2 Introduction

Inverse photoemission (IPE) occurs when a material captures an incident electron in one of the high-energy unoccupied states, which then can subsequently de-excite to a lower-energy unoccupied state by spontaneous emission of a photon. One can infer information about the unoccupied states using the kinetic energy of the incident electron and the energy of the emitted photon. IPE, which is also referred to as radiative electron capture, has been previously used for studying electron–ion radiative recombination in electron scattering events. [25, 80]

IPE spectroscopy has been used to investigate the unoccupied states of various chemical systems and materials,[113, 21, 40, 68] for example, the LUMO energies of various π -conjugated organic molecules and molecular organic semiconductors. [44, 29, 129] In conjunction with other techniques, IPE spectroscopy has been used to investigate the band structure of spatially aligned graphene nanoribbons on stepped Au(788) surfaces and has also been used to probe the conduction bands of solar cell components and PbS quantum dots in thin films. [77, 105, 76] IPE spectroscopy has also been used to investigate the effects of ion bombardment on the unoccupied electronic surface states of Ni(110). [127] A newer technique, low-energy inverse photoemission spectroscopy (LEIPS), was developed to circumvent the damaging effects of IPE spectroscopy on organic semiconductors. [126] It has been shown that the signal intensity for LEIPS can be enhanced by exploiting the occurrence of surface plasmon resonance in Ag nanoparticles. [118]

The IPE process has also been theoretically and computationally investigated for some chemical systems. For example, the inverse photoemission and photoemission processes in NiO have been simulated by the use of complete active space self-consistent field theory and periodic many-body G_0W_0 calculations. [1] In another work, the density of states of the valence and conduction bands of metal halide perovskites were theoretically investigated using density functional theory and experimentally investigated using IPE spectroscopy, along with ultraviolet photoemission spectroscopy. [35]

IPE spectroscopy enables the investigation of states that cannot be accessed using single-photon photoemission spectroscopy.[113] Additionally, IPE spectroscopy is an alternative to two-photon photoemission spectroscopy and near-edge X-ray absorption fine structure (NEXAFS), which can provide direct and clear information about the unoccupied states in materials. [121, 14, 13, 81, 113] IPE spectroscopy allows for the investigation of unoccupied states while avoiding the complications that arise due to the formation of a core hole. As a result, electron–hole interactions do not need to be considered. [81, 113, 14]

The quantum chemical investigation of the IPE process introduces additional challenges compared to charge-neutral electronic excitations due to the unbound nature of the incoming electron. Consequently, one has to deal with not only bound states with $E < 0$ but also scattering states with $E > 0$. The computational investigation of IPE processes in quantum dots (QDs) introduces additional difficulties not encountered for small molecules. Specifically, quantum dots have a high density of states which dramatically increase the number of possible virtual-to-virtual transitions. For example, in the case of $\text{Pb}_{140}\text{S}_{140}$, which is the largest system studied in this work, the total number of possible transitions, that can take part in the IPE process is in excess of 1 million. Additionally, due to the large number of molecular orbitals and basis functions, the treatment of electron–electron correlation becomes challenging because of the computationally expensive AO-to-MO transformation of the required two-electron integrals.

In this study, we demonstrate that the judicious selection of external static electric field strengths

and directions (henceforth referred to as the Stark fields) can significantly enhance spontaneous photon emission from the IPE transitions. We present a new theoretical approach, developed by combining the frequency-dependent geminal-screened interaction kernel method (FD-GSIK)[73] with time-dependent perturbation theory, for investigating IPE transitions in CdS, CdSe, PbS, and PbSe QDs. The central quantity of interest for the IPE process is the lineshape function, $g(\omega)$, and the ratio, $g(\omega_2)/g(\omega_1)$, which can be used to quantify the relative transition probability of photon emission as a function of the emitted photon frequency (ω). The presence of a Stark field modifies the molecular orbitals and the molecular orbital energies $\{\epsilon_p^{\text{field-on}}, \chi_p^{\text{field-on}}\}$ (Figure 7.1). Consequently, this changes both the QD–electron and QD–light interaction terms and modifies

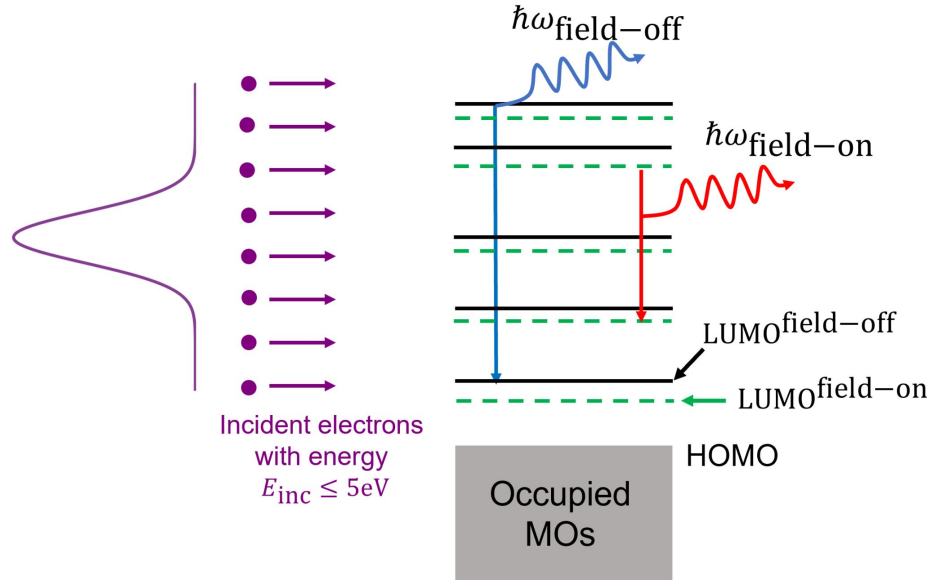


Figure 7.1: Impact of Stark field on IPE process. Incoming electrons have a distribution of kinetic energies (shown in purple). Application of external electric field changes the molecular orbital energies (shown in green) and the frequency of the emitted photon ($\hbar\omega_{\text{field-on}}$, shown in red).

the ability of the QD to capture the incoming electron and spontaneously emit a photon with a given frequency. We quantify the change in the IPE transitions by defining the three critical metrics associated with the IPE lineshape ($g(\omega)$). The first is $I_{\text{enhancement}}$ (Equation 7.1), which quantifies the change in the most prominent transition (denoted by g_{max}) in the IPE spectra due to the application of the Stark field. We define $I_{\text{enhancement}}$ as

$$I_{\text{enhancement}} = \frac{g_{\text{max}}^{\text{field-on}}(\omega) - g_{\text{max}}^{\text{field-off}}(\omega)}{g_{\text{max}}^{\text{field-off}}(\omega)}. \quad (7.1)$$

Second, $\Delta\omega_{\text{Stark}}$ quantifies the effect of the Stark field on the frequency of the dominant transition

in the IPE spectra (Equation 7.2). Formally $\Delta\omega_{\text{Stark}}$ is defined as

$$\Delta\omega_{\text{Stark}} = \omega^{\text{field-on}} - \omega^{\text{field-off}}. \quad (7.2)$$

Finally, the overall impact of the Stark fields on light–matter interactions is quantified by $\Delta g_{\text{lineshape}}$, which is defined as the cumulative change in the lineshape over the frequency range of $[\omega_1, \omega_2]$ and is given by

$$\Delta g_{\text{lineshape}} = \frac{1}{\omega_2 - \omega_1} \int_{\omega_1}^{\omega_2} d\omega \frac{|g_{\text{lineshape}}^{\text{field-on}}(\omega) - g_{\text{lineshape}}^{\text{field-off}}(\omega)|}{g_{\text{lineshape}}^{\text{field-off}}(\omega) + |\eta|}. \quad (7.3)$$

7.3 Theory

First-order propagator for spontaneous emission

$$i\hbar \frac{d}{dt} U_{\text{rad}}(t, t_0) = [H + W^{\text{rad}}(\omega, t)] U_{\text{rad}}(t, t_0) \quad (7.4)$$

The first-order approximation to the exact propagator in the eigenbasis of H ($U_{\text{rad}}^{(1)}(t)$) is known from time-dependent perturbation theory.

$$\langle \Psi_n | U_{\text{rad}}^{(1)}(t, t_0) | \Psi_m \rangle = \frac{1}{i\hbar} \int_0^t d\tau e^{i\omega_{nm}\tau/\hbar} \langle \Psi_n | W^{\text{rad}}(\omega, \tau) | \Psi_m \rangle \quad (7.5)$$

The light-matter interaction is treated using the electric-dipole approximation and the time-dependence of the field is treated as sine wave, as demonstrated in Equation 7.6.

$$\langle \Psi_n | W^{\text{rad}}(\tau, \omega) | \Psi_m \rangle = \frac{1}{2i} W_{nm}^{\text{dipole}} (e^{i\omega\tau} - e^{-i\omega\tau}) \quad (7.6)$$

Substituting Equation 7.6 into Equation 7.5, the first-order propagator can be expressed as,

$$\langle \Psi_n | U_{\text{rad}}^{(1)}(t, t_0) | \Psi_m \rangle = \frac{-W_{nm}^{\text{dipole}}}{2\hbar} \int_0^t d\tau e^{i(\omega_{nm}+\omega)\tau/\hbar} - e^{i(\omega_{nm}-\omega)\tau/\hbar} \quad (7.7)$$

and after integration we obtain,

$$\langle \Psi_n | U_{\text{rad}}^{(1)}(t, t_0) | \Psi_m \rangle = \frac{W_{nm}^{\text{dipole}}}{2i\hbar} \left[\frac{1 - e^{i(\omega_{nm}+\omega)t/\hbar}}{\omega_{nm} + \omega} - \frac{1 - e^{i(\omega_{nm}-\omega)t/\hbar}}{\omega_{nm} - \omega} \right] \quad (7.8)$$

which can then be simplified to the sine function line-shape as follows.

$$\langle \Psi_n | U_{\text{rad}}^{(1)}(t, t_0) | \Psi_m \rangle = \frac{W_{nm}^{\text{dipole}}}{2i\hbar} \left[i e^{i(\omega_{nm}+\omega)t/\hbar} \frac{\sin[(\omega_{nm} + \omega)t/2]}{(\omega_{nm} + \omega)/2} - i e^{i(\omega_{nm}-\omega)t/\hbar} \frac{\sin[(\omega_{nm} - \omega)t/2]}{(\omega_{nm} - \omega)/2} \right] \quad (7.9)$$

$$\langle \Psi_n | U_{\text{rad}}^{(1)}(t, t_0) | \Psi_m \rangle = \frac{W_{nm}^{\text{dipole}}}{2\hbar} \frac{\sin[(\omega_{nm} - \omega)t/2]}{(\omega_{nm} - \omega)/2} e^{i(\omega_{nm} + \omega)t/\hbar} \quad (7.10)$$

The final result shows that,

$$|\Psi(t)\rangle = U_{\text{rad}}(t, 0) |\Psi_{\text{in}}\rangle \quad (7.11)$$

and the probability of transition to the final state is given as

$$P_f(t) = |\langle \Psi_f | \Psi(t) \rangle|^2 \quad (7.12)$$

We define the transition rate per unit time Γ_f as,

$$P_f(t) = t\Gamma_f \quad (7.13)$$

where Γ_f is obtained using numerical approximation to first-order derivative,

$$\Gamma_f = \frac{P_f(t + \Delta t) - P_f(t)}{\Delta t} \quad (7.14)$$

The initial state preparation is defined as:

$$|\Psi_{\text{in}}\rangle = \Omega_+ |\Psi_0^N\rangle \quad (7.15)$$

The expression for the Möller operator in the eigenket of H is given as

$$\langle \Psi_n^{N+1} | \Omega_+ | \Psi_0^N \rangle = \sum_b \int_{-\infty}^{+\infty} d\mathbf{k} \rho_{\text{inc}}(\mathbf{k}) \langle \mathbf{k} | w^{\text{e-dot}} | b \rangle \langle \Psi_n^{N+1} | b^\dagger | \Psi_0^N \rangle \quad (7.16)$$

The probability density $\rho_{\text{inc}}(\mathbf{k})$ is defined as,

$$\rho_{\text{inc}}(\mathbf{k}) = C \theta(E_{\text{inc}} - \frac{\hbar^2 k^2}{2m}) \quad (7.17)$$

and the proportionality constant C is obtained from the normalization condition. Integrating over k-space we get,

$$C^{-1} = \int_{-\infty}^{+\infty} d\mathbf{k} \theta(E_{\text{inc}} - \frac{\hbar^2 k^2}{2m}) \quad (7.18)$$

Transforming into spherical polar coordinates and integrating over the angular coordinates,

$$C^{-1} = 4\pi \int_0^{+\infty} dk k^2 \theta(E_{\text{inc}} - \frac{\hbar^2 k^2}{2m}) \quad (7.19)$$

which can be written as,

$$C^{-1} = 4\pi \int_0^{k_{\text{max}}} dk k^2 = \frac{4}{3} \pi k_{\text{max}}^3 \quad (7.20)$$

where,

$$E_{\text{inc}} = \frac{\hbar^2 k_{\text{max}}^2}{2m} \quad (7.21)$$

The interaction between the incoming electron and the QD is given by,

$$\langle \mathbf{k} | w^{\text{e-dot}} | b \rangle = \langle \mathbf{k} | v^{\text{ext}} | b \rangle + \sum_{i=1}^N \langle \mathbf{k} i | r_{12}^{-1} (1 - P_{12}) | b i \rangle \quad (7.22)$$

Substituting,

$$\langle \Psi_f | \Psi(t) \rangle = \langle \Psi_f | U_{\text{rad}}(t, 0) \Omega_+ | \Psi_0^N \rangle \quad (7.23)$$

Inserting a complete set of eigenkets of the H ,

$$\langle \Psi_f | \Psi(t) \rangle = \sum_m \langle \Psi_f | U_{\text{rad}}(t, \omega) | \Psi_m \rangle \langle \Psi_m | \Omega_+ | \Psi_0^N \rangle \quad (7.24)$$

which implies,

$$\langle \Psi_f | \Psi(t) \rangle = \sum_b \sum_m \int_{-\infty}^{+\infty} d\mathbf{k} \theta(E_{\text{inc}} - \frac{\hbar^2 k^2}{2m}) \langle \Psi_f | U_{\text{rad}}(t, \omega) | \Psi_m \rangle \langle \mathbf{k} | w^{\text{e-dot}} | b \rangle \langle \Psi_m^{N+1} | b^\dagger | \Psi_0^N \rangle \quad (7.25)$$

Defining the pole-strength A_{mb} as,

$$A_{mb} = \langle \Psi_m^{N+1} | b^\dagger | \Psi_0^N \rangle \quad (7.26)$$

and the matrix element $w_{\mathbf{k}b}^{\text{e-dot}}$ as,

$$w_{\mathbf{k}b}^{\text{e-dot}} = \langle \mathbf{k} | w^{\text{e-dot}} | b \rangle \quad (7.27)$$

The probability amplitude can be expressed as follows.

$$\langle \Psi_a | \Psi(t) \rangle = \frac{1}{2\hbar} \sum_b \sum_m \int_{-\infty}^{+\infty} d\mathbf{k} \rho_{\text{inc}}(\mathbf{k}) W_{am}^{\text{dipole}} w_{\mathbf{k}b}^{\text{e-dot}} A_{mb} \frac{\sin[(\omega_{am} - \omega)t/2]}{(\omega_{am} - \omega)/2} e^{i(\omega_{nm} + \omega)t/\hbar} \quad (7.28)$$

Calculation of zero-field inverse photoemission spectra

The electron capture process and subsequent spontaneous emission of the photon were calculated using time-dependent perturbation theory (TDPT). The TDPT formulation had been derived earlier for treating radiative electron capture in electron-ion and electron-atom scattering. Using TDPT, it can be shown that up to first-order, the contribution to the IPE transition probability amplitude, $T_{\mathbf{k}a}$, is given by the Feynmann-Goldstone diagram shown in [Figure 7.2](#). The incoming electron beam was described using a plane wave basis, $|\mathbf{k}\rangle$, with a distribution function of $\rho_{\text{inc}}(\mathbf{k})$. The distribution function was constructed such that the kinetic energy of the incoming electron is uniformly distributed in the range of 0–5 eV and is given by $\rho_{\text{inc}}(\mathbf{k}) \propto \theta(E_{\text{inc}} - \frac{\hbar^2 k^2}{2m})$, where the

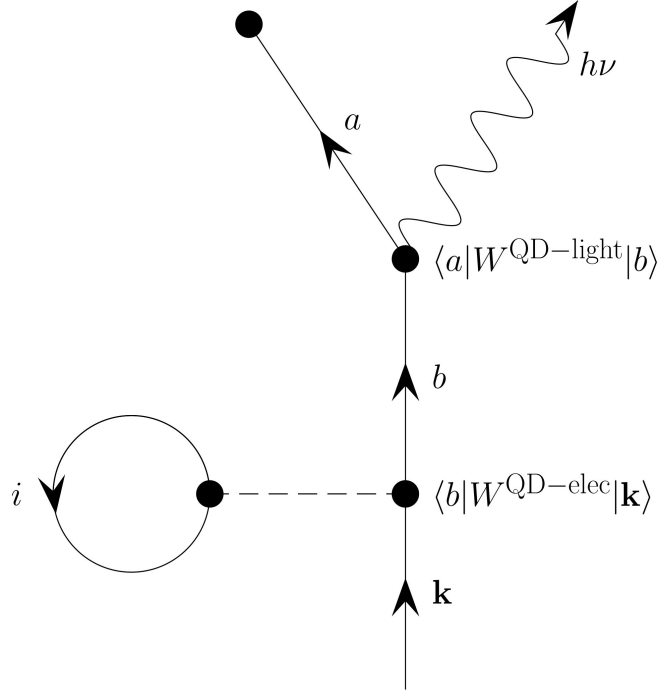


Figure 7.2: Feynman–Goldstone diagram for the first-order approximation to the inverse photoemission transition amplitude.

proportionality constant was obtained by enforcing that $\langle \rho_{\text{inc}}(\mathbf{k}) \rangle = 1$. The electron–QD interaction (vertex 1 in Figure 7.2) includes both one-body (v_{ext}) and two-body interactions (r_{12}^{-1} Coulomb and exchange). The field–matter interaction is treated semiclassically where the radiative de-excitation process between states $|b\rangle$ and $|a\rangle$ is treated using the electric dipole approximation (vertex 2 in Figure 7.2), and the EM field was treated as a time-dependent periodic field with frequency ω . Using Figure 7.2, the first-order approximation to the $(|\mathbf{k}\rangle \rightarrow |a\rangle)$ IPE transition amplitude is given as

$$T_{\mathbf{k}a}(\omega, t) = \frac{1}{2\hbar} \sum_b^{N_{\text{vir}}} W_{\mathbf{k}b}^{\text{QD-elec}} W_{ba}^{\text{QD-light}} \theta(b - a) \times \frac{\sin[(\omega_{ab} - \omega)t/2]}{(\omega_{ab} - \omega)t/2} e^{i(\omega_{ab} + \omega)t/\hbar}, \quad (7.29)$$

where $W_{\mathbf{k}b}^{\text{QD-elec}}$ and $W_{ab}^{\text{QD-light}}$ are the coupling matrix elements for QD–electron and QD–light interactions, and $\theta(b - a)$ ensures that the transitions are de-excitations. The sine term in Equation 7.29 is the resonance contribution to transition amplitude, and the corresponding anti-resonance term, with $\omega_{ab} + \omega$, was ignored. The lineshape function, $g(\omega)$, was obtained by integrating over the

distribution of incoming k-vectors and all de-excitation channels and is given as

$$g(\omega) = \lim_{t \rightarrow +\infty} \sum_a \int_{-\infty}^{+\infty} d\mathbf{k} \rho_{\text{inc}}(\mathbf{k}) |T_{\mathbf{k}a}(t)|^2. \quad (7.30)$$

The $t \rightarrow +\infty$ limit of $\sin(\theta t)/(\theta t)$ results in the delta function $\delta(\omega_{ab} - \omega)$. The IPE spectra were obtained by numerically calculating the long-time limit of Equation 7.30, and the value of t_{max} was obtained by setting $t_{\text{max}}\omega_{ab} = 1000$ for the transition with the highest oscillator strength.

The first-order correction to the IPE transition amplitudes due to electron–electron correlation was obtained using the frequency-dependent geminal-screened interaction kernel (FD-GSIK) method.[7, 8, 9, 73] The FD-GSIK method was used to obtain accurate de-excitation energies $\omega_{ab}^{\text{FD-GSIK}}$, which were then used in Equation 7.29. In addition to FD-GSIK, electron–electron correlation effects can also be included using the vertex correction derived from MBPT.[61, 60] We compare the IPE spectrum, obtained using the FD-GSIK method, with the spectrum obtained using vertex-corrected MBPT [61, 60]. We restricted the energy of the incoming electron, which initiates the inverse photoemission event, to be less than or equal to 5 eV. We calculated the relative transition probabilities of observing the spontaneous emission of a photon in the range of 3 to 6 eV for all of the dots. For each spectrum, the relative transition probability (ordinate) was obtained by dividing the transition probability, at each value of ω (abscissa), by the maximum transition probability value. In all cases, the results from the FD-GSIK method were tested against the MBPT vertex correction method [61], and both methods were found to be in good agreement with each other.

The structures for the dots were obtained from their respective bulk lattices. The Hartree–Fock calculations were performed using the LANL2DZ basis with the LANL2DZ ECP potential using the TERACHEM electronic structure package. The integration over the plane-wave basis was performed stochastically where the incident energy E_{inc} was used to fix the magnitude of the k-vector and was sampled with 1 meV spacing in the range 0 to 5 eV. The direction of the k-vector was sampled uniformly by picking unit vectors on a unit sphere using the Marsaglia algorithm. [71, 78]

Calculation of Stark effect on IPE spectra:

The effect of the external DC Stark field was included as the one-body potential to the field-free Fock operator,

$$\hat{f}^{\text{field-on}} = \hat{f}^{\text{field-off}} - E_{\text{Stark}}(\hat{\mathbf{n}}_{\text{Stark}} \cdot \mathbf{r}). \quad (7.31)$$

The field-free Fock operator was diagonalized to obtain the field-dependent dressed molecular orbital and energies [10] $\{\epsilon_p^{\text{field-on}}, \chi_p^{\text{field-on}}\}$, which were then used for the calculation of the $g^{\text{field-on}}(\omega)$ lineshape function (Equation 7.30). The direction of the Stark field was selected to be along the Cartesian directions ($\hat{\mathbf{n}}_{\text{Stark}} = \text{x,y,z}$) for a range of E_{Stark} , and the resultant increase in IPE transition probability is presented in Table 7.3. The maximally coupled electric field directions were determined by fixing the $E_{\text{Stark}} = 1$ and searching over $\hat{\mathbf{n}}$ directions such that $\Delta g_{\text{lineshape}}$ is maximized. The maximally coupled electric field directions are formally defined as

$$\hat{\mathbf{n}}_{\text{Stark}}^{\text{max-coupled}} = \arg \max_{E_{\text{Stark}}=1, \hat{\mathbf{n}}_{\text{Stark}} \in \text{unit sphere}} \Delta g_{\text{lineshape}}. \quad (7.32)$$

In this work, we restricted the set of the directions to be composed of 26 unique directions on the unit sphere, where each component of these vectors was restricted such that they can only take on values of either -1, 0, or +1. This resulted in a set of 27 vectors, out of which the $[0, 0, 0]$ vector was discarded, and the remaining vectors were normalized to one.

7.4 Results

Zero-field inverse photoemission spectra

In subplot A of Figure 7.3, we see that there are two prominent peaks of the inverse PE spectra of $\text{Cd}_{24}\text{S}_{24}$, while in subplot B we see that there are four prominent peaks of the Inverse PE spectrum of $\text{Cd}_{45}\text{S}_{45}$. The peak with the greatest intensity for $\text{Cd}_{24}\text{S}_{24}$ occurs at 3.091 eV. The second most prominent peak of this spectrum occurs at approximately 3.65 eV. The peak with the greatest intensity for $\text{Cd}_{45}\text{S}_{45}$ occurs at 3.030 eV. The second largest peak of this spectrum occurs at approximately 3.85 eV while the third and fourth largest peaks occur at approximately 3.65 and 3.25 eV, respectively. As can be observed from interpreting Figure 7.3, the most probable energy of the emitted photon, due to the occurrence of an inverse PE event, is very close to 3 eV for both of the CdS dots. In subplot A of Figure 7.4, we see that there are four prominent peaks of the inverse

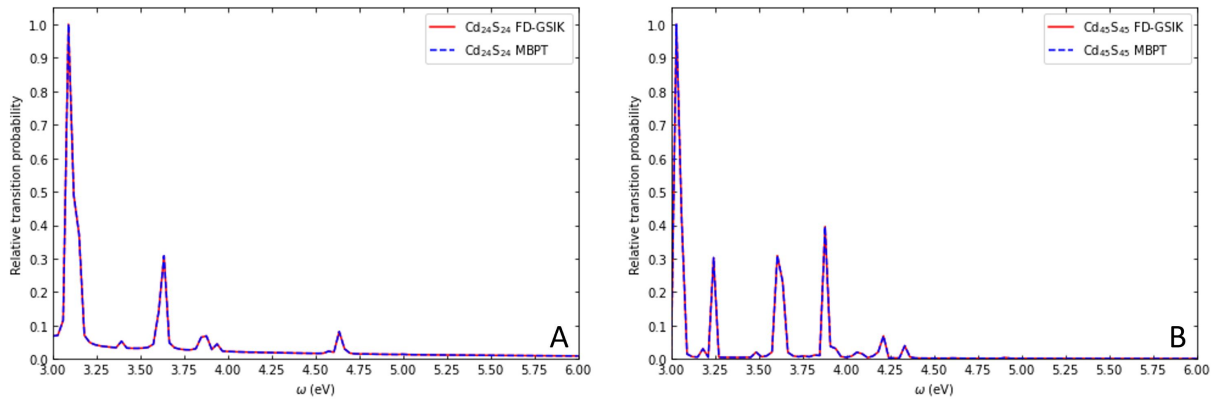


Figure 7.3: Subplots A and B (relative transition probability versus ω) display the inverse photoemission spectra obtained using the FD-GSIK method and MBPT for the $\text{Cd}_{24}\text{S}_{24}$ and $\text{Cd}_{45}\text{S}_{45}$ quantum dot, respectively.

PE spectra of $\text{Cd}_{24}\text{Se}_{24}$, while in subplot B we see that there are three prominent peaks of the Inverse PE spectrum of $\text{Cd}_{54}\text{Se}_{54}$. The peak with the greatest intensity for $\text{Cd}_{24}\text{Se}_{24}$ occurs at 3.333 eV. The second most prominent peak of this spectrum occurs at approximately 3.15 eV, while the third and fourth largest peaks occur at approximately 4.50 and 3.50 eV, respectively. The peak with the greatest intensity for $\text{Cd}_{54}\text{Se}_{54}$ occurs at 3.273 eV. The second and third largest peaks of this spectrum occur at approximately 3.80 eV and 4.00 eV, respectively. In subplot A of Figure 7.5, we see that there are four prominent peaks of the inverse PE spectra of $\text{Pb}_{44}\text{S}_{44}$, while in subplot B we see that there are six prominent peaks of the Inverse PE spectrum of $\text{Pb}_{140}\text{S}_{140}$. The peak with the

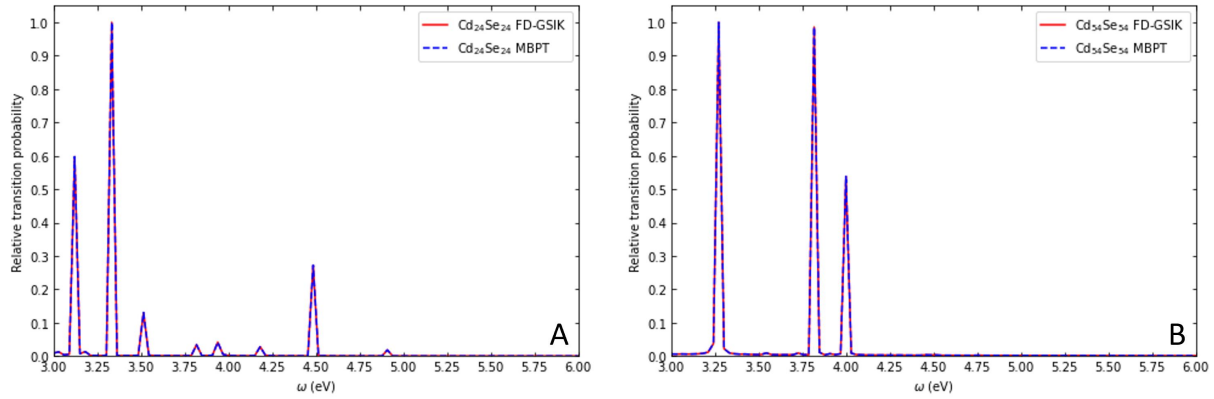


Figure 7.4: Subplots A and B (relative transition probability versus ω) display the inverse photoemission spectra obtained using the FD-GSIK method and MBPT for the $\text{Cd}_{24}\text{Se}_{24}$ and $\text{Cd}_{54}\text{Se}_{54}$ quantum dots, respectively.

greatest intensity for $\text{Pb}_{44}\text{S}_{44}$ occurs at 3.091 eV. The second most prominent peak of this spectrum occurs at approximately 3.40 eV, while the third and fourth largest peaks occur at approximately 3.50 and 3.25 eV, respectively. The peak with the greatest intensity for $\text{Pb}_{140}\text{S}_{140}$ occurs at 3.788 eV. The second and third largest peaks of this spectrum occur at approximately 3.65 eV and 3.20 eV, respectively, while the fourth, fifth, and sixth largest peaks occur at approximately 4.15 eV, 4.10 eV and 3.05 eV, respectively. In subplot A of Figure 7.6, we see that there are five prominent peaks

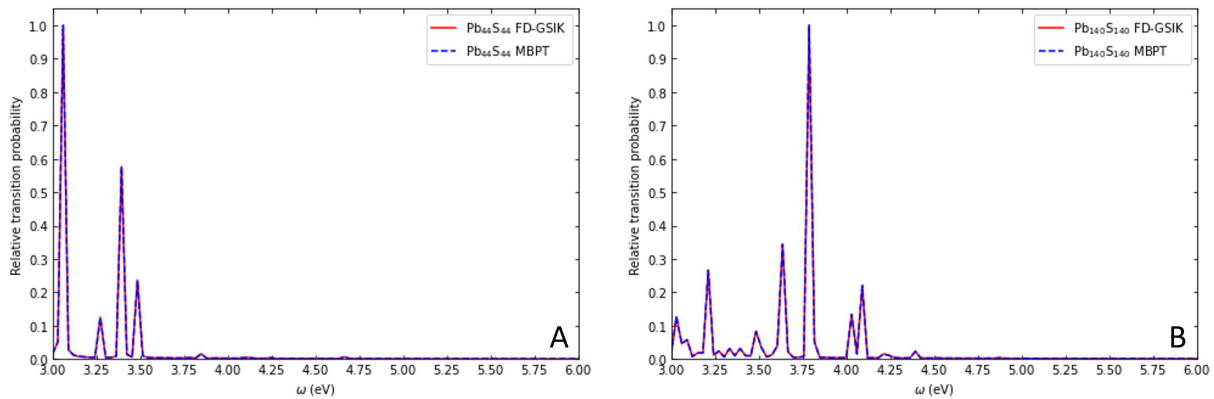


Figure 7.5: Subplots A and B (relative transition probability versus ω) display the inverse photoemission spectra obtained using the FD-GSIK method and MBPT for the $\text{Pb}_{44}\text{S}_{44}$ and $\text{Pb}_{140}\text{S}_{140}$ quantum dots, respectively.

of the inverse PE spectra of $\text{Pb}_{29}\text{Se}_{29}$, while in subplot B we see that there are two prominent peaks

of the Inverse PE spectrum of $\text{Pb}_{52}\text{Se}_{52}$. The peak with the greatest intensity for $\text{Pb}_{29}\text{Se}_{29}$ occurs at 0.909 eV. The second and third largest peaks of this spectrum occur at approximately 1.10 eV and 0.60 eV, respectively, while the fourth and fifth largest peaks occur at approximately 0.10 eV and 2.00 eV, respectively. The peak with the greatest intensity for $\text{Pb}_{52}\text{Se}_{52}$ occurs at 3.212 eV, while the second most prominent peak of this spectrum occurs at approximately 3.15 eV.

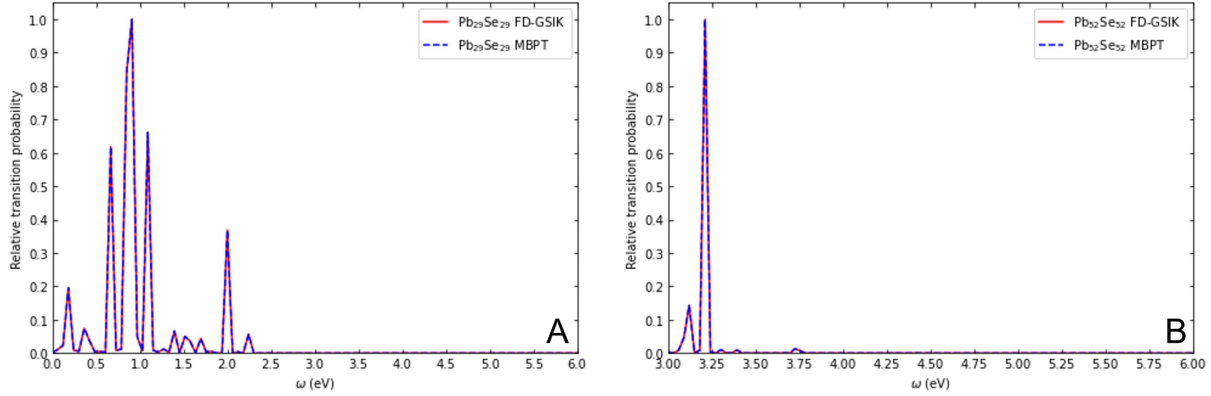


Figure 7.6: Subplots A and B (relative transition probability versus ω) display the inverse photoemission spectra obtained using the FD-GSIK method and MBPT for the $\text{Pb}_{29}\text{Se}_{29}$ and $\text{Pb}_{52}\text{Se}_{52}$ quantum dots, respectively.

Field-induced increase of IPE transition probability

In this work, the energies of the incoming electrons, which initiated the IPE transitions, were restricted to be less than or equal to 5 eV. The impact of the external static electric field on QDs was investigated for five different electric field strengths (denoted as $E_{\text{Stark}} = E_1, \dots, E_5$) with values $[-2, -1, 0, +1, +2] \times 10^{-5} E_{\text{au}}$ along three Cartesian (x,y,z) directions. The field strengths were selected to be weak and non-ionizing for all the QDs studied with $ea_0 E_{\text{Stark}}/E_{\text{IP}} \leq 10^{-5}$, where E_{au} is the electric field in atomic units, e is the charge of the electron, a_0 is the Bohr radius, and E_{IP} is the ionization potential. For each electric field, the value of ω at which the maximum relative transition probability occurs corresponds to the most probable energy of the photon that is emitted as a result of an inverse photoemission event, under the conditions previously described. In order to effectively visualize the spectra for all of the electric fields on a single plot for each direction, we shifted the values of the relative transition probabilities for each spectrum by adding a unique constant. The E1 spectrum was shifted upwards by adding 12 to each value of the relative transition probability and the E2 spectrum was shifted upwards by adding 9 to each value of the relative transition probability. The E3 and E4 spectra were shifted upwards by adding 6 and 3 to each value of the relative transition probabilities, respectively. The values of the relative transition probability were not shifted for the E5 spectrum. In Table 7.1, descriptions of the electric fields, E1, E2, E3, E4, and E5, are provided. The greatest enhancement of the IPE transition probabilities for $\text{Cd}_{24}\text{S}_{24}$ and $\text{Cd}_{45}\text{S}_{45}$ was achieved with an electric field aligned with these dots along the x-axis, while

Table 7.1: Electric Field Vector Information

field	x-component	y-component	z-component
E1x	-2.0×10^{-5}	0.0	0.0
E2x	-1.0×10^{-5}	0.0	0.0
E3x	0.0	0.0	0.0
E4x	1.0×10^{-5}	0.0	0.0
E5x	2.0×10^{-5}	0.0	0.0
E1y	0.00	-2.0×10^{-5}	0.0
E2y	0.00	-1.0×10^{-5}	0.0
E3y	0.0	0.0	0.0
E4y	0.00	1.0×10^{-5}	0.0
E5y	0.00	2.0×10^{-5}	0.0
E1z	0.00	0.00	-2.0×10^{-5}
E2z	0.00	0.00	-1.0×10^{-5}
E3z	0.0	0.0	0.0
E4z	0.00	0.00	1.0×10^{-5}
E5z	0.00	0.00	2.0×10^{-5}

Table 7.2: Percent change in maximum relative transition probabilities for electric fields along x, y, and z directions (Equation 7.1).

Chemical System	$I_{\text{enh.}}^x$	$I_{\text{enh.}}^y$	$I_{\text{enh.}}^z$
Cd ₂₄ S ₂₄	156%	-5%	152%
Cd ₄₅ S ₄₅	205%	200%	168%
Cd ₂₄ Se ₂₄	33%	56%	117%
Cd ₅₄ Se ₅₄	161%	35%	188%
Pb ₄₄ S ₄₄	15%	15%	25%
Pb ₁₄₀ S ₁₄₀	94%	19%	94%
Pb ₂₉ Se ₂₉	268%	98%	279%
Pb ₅₂ Se ₅₂	24%	-14%	-14%

for Cd₂₄Se₂₄ and Cd₅₄Se₅₄ the greatest enhancement occurred in the presence of an electric field aligned along the z-axis (Table 7.2). Out of all the QDs, the most significant enhancement of the IPE transition probability was observed for Pb₂₉Se₂₉ when the field was aligned along the z-axis. The Stark field also suppresses the IPE transition probability for some systems. For example, for Pb₅₂Se₅₂ we observed a decrease in the IPE transition probability for the fields aligned along the y- and z-axes (Table 7.2). Figures 7.7-7.14 contain plots of the relative transition probability (ordinate) versus ω (abscissa) for CdS, CdSe, PbS, and PbSe quantum dots, in the presence of electric fields of differing strengths (E1, E2, E3, E4, and E5), aligned with the dots along either the x, y, or z axis. For each spectrum in figures 7.7-7.14, the relative transition probability was obtained by dividing the transition probability at each value of ω by the maximum value of the transition probability for

the E3 spectrum. It is relevant to note that the spectrum labeled E3, was obtained for the quantum dots in the absence of an electric field. For the plots subplots A in each figure, the electric fields are aligned with the quantum dots along the x-direction. For subplots B and C, the electric fields are aligned with the quantum dots along the y-direction and z-direction, respectively.

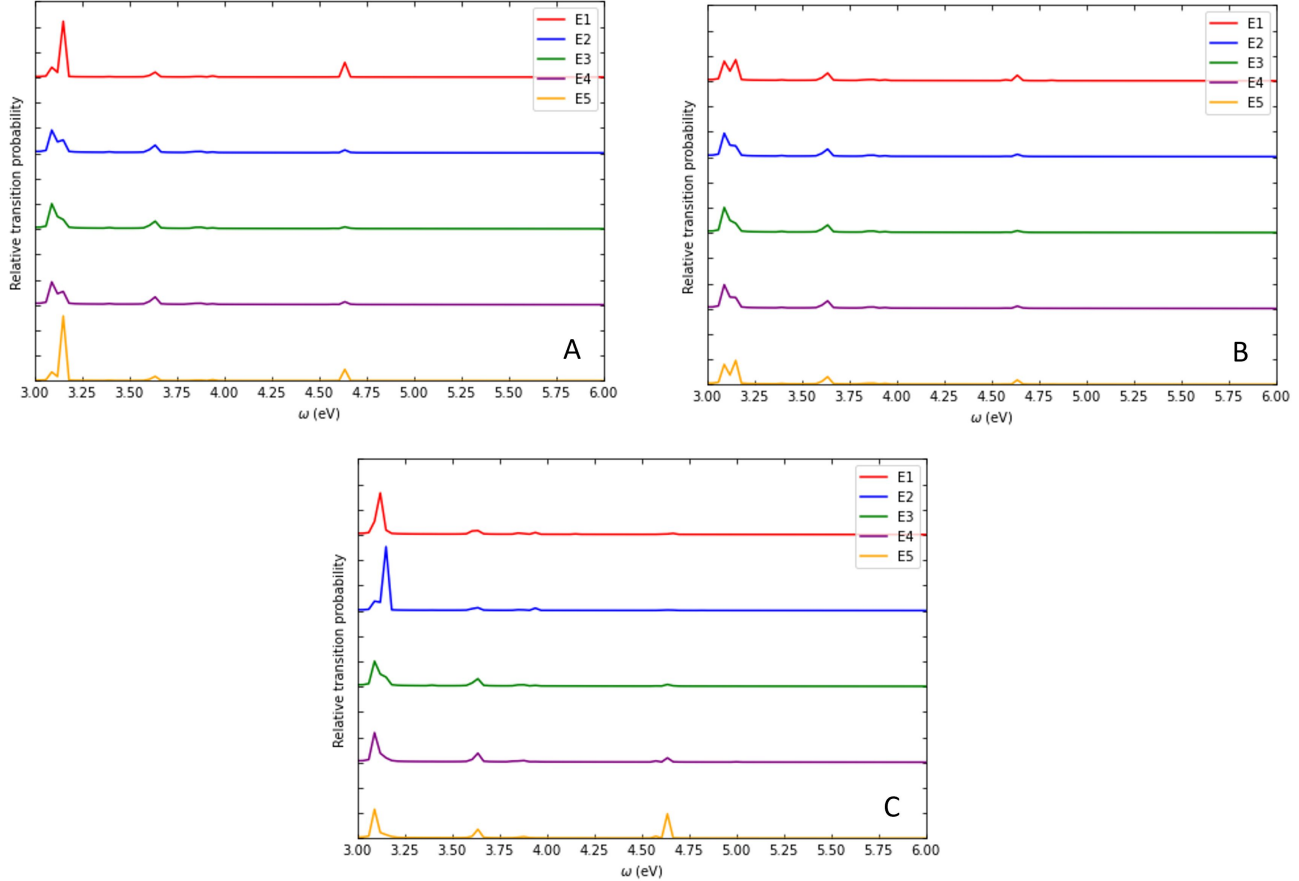


Figure 7.7: Relative transition probability (ordinate) versus ω (abscissa) for $\text{Cd}_{24}\text{S}_{24}$ in the presence of electric fields aligned along the x-direction (Subplot A), y-direction (Subplot B), and z-direction (Subplot C).

Field-induced shift in frequency of spontaneously emitted photon

The frequency of the emitted photons at maximum intensity depended strongly on the direction of the Stark field. For example, in the case of $\text{Cd}_{54}\text{Se}_{54}$, in the presence of the E_2 field aligned along the z-axis, the energy of the emitted photon was found to be blue-shifted by 0.727 eV. However, for fields E_4 and E_5 , no shift in the emitted frequency was observed. The Stark shift in the emitted frequency (defined in Equation 7.2) was found to be blue-shifted for all the QDs (Table 7.3) except for $\text{Cd}_{24}\text{Se}_{24}$ and $\text{Pb}_{29}\text{Se}_{29}$, both of which exhibited a red-shift. These field-dependent IPE calculations demonstrate (Table 7.3) that the non-ionizing weak Stark fields studied here are capable of generating a shift in the emitted photon frequency in the range of $[-0.8, +0.8]$ eV.

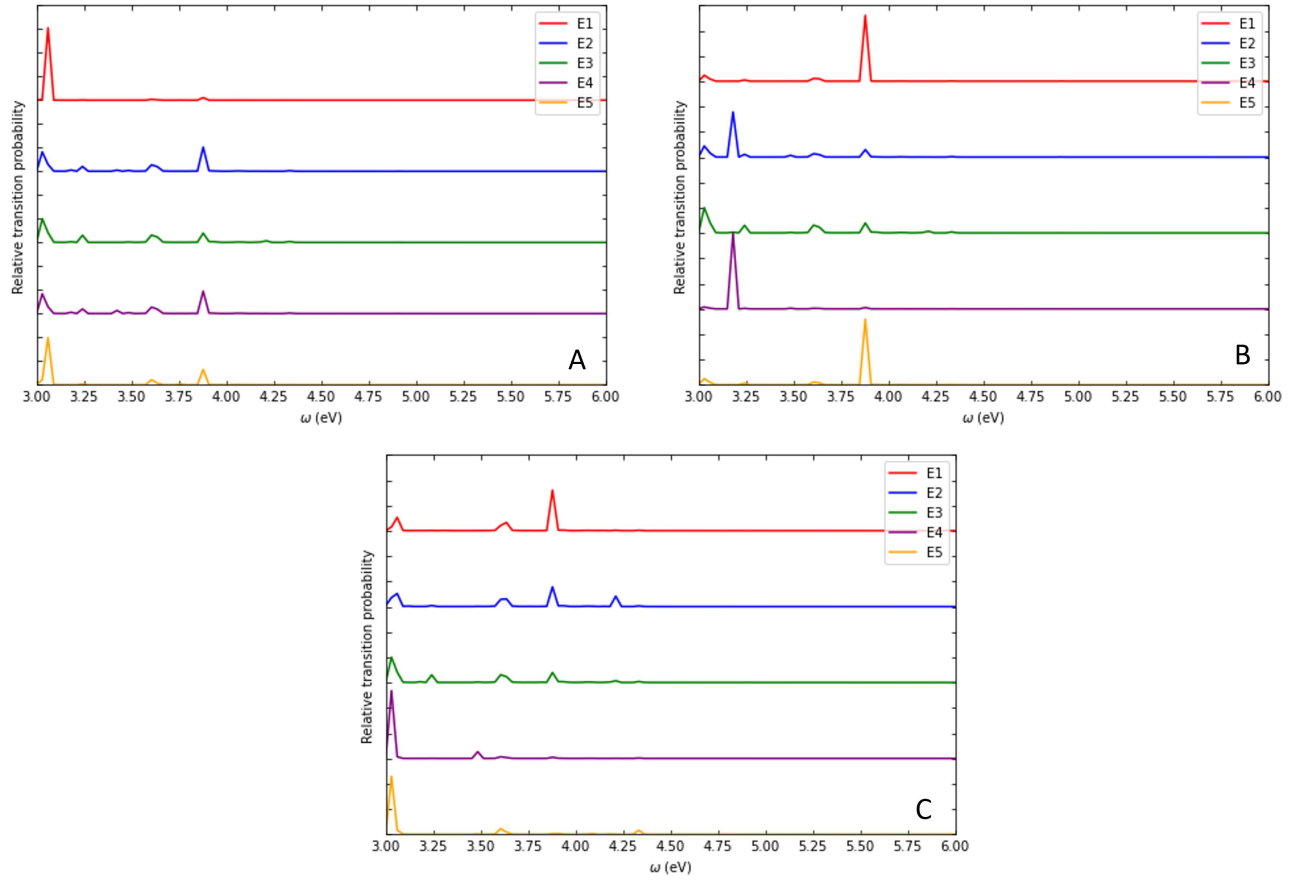


Figure 7.8: Relative transition probability (ordinate) versus ω (abscissa) for $\text{Cd}_{45}\text{S}_{45}$ in the presence of electric fields aligned along the x-direction (Subplot A), y-direction (Subplot B), and z-direction (Subplot C).

Table 7.3: Change in emitted photon energies (eV) at the maximum relative transition probabilities for electric fields aligned along x, y, and z directions (Equation 7.2).

Chemical System	$\omega^{\text{field-off}}$	$\Delta\omega_x^{\text{field-on}}$	$\Delta\omega_y^{\text{field-on}}$	$\Delta\omega_z^{\text{field-on}}$
$\text{Cd}_{24}\text{S}_{24}$	3.091	0.061	0.061	0.061
$\text{Cd}_{45}\text{S}_{45}$	3.030	0.848	0.848	0.848
$\text{Cd}_{24}\text{Se}_{24}$	3.333	-0.212	-0.212	-0.303
$\text{Cd}_{54}\text{Se}_{54}$	3.273	0.545	0.727	0.727
$\text{Pb}_{44}\text{S}_{44}$	3.091	0.424	0.424	0.424
$\text{Pb}_{140}\text{S}_{140}$	3.788	0.606	0.606	0.606
$\text{Pb}_{29}\text{Se}_{29}$	0.909	-0.848	0.000	-0.727
$\text{Pb}_{52}\text{Se}_{52}$	3.212	0.182	0.152	0.152

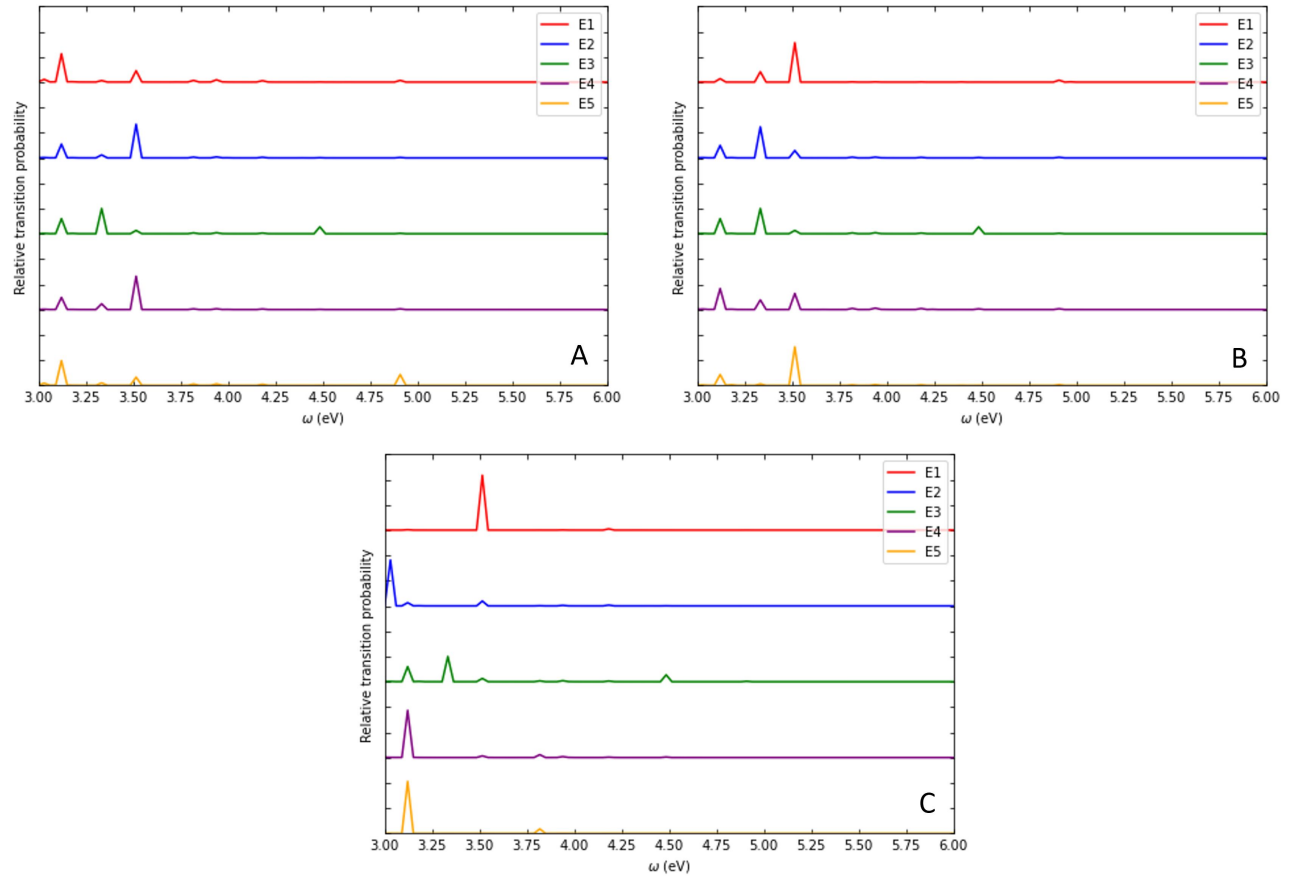


Figure 7.9: Relative transition probability (ordinate) versus ω (abscissa) for $\text{Cd}_{24}\text{Se}_{24}$ in the presence of electric fields aligned along the x-direction (Subplot A), y-direction (Subplot B), and z-direction (Subplot C).

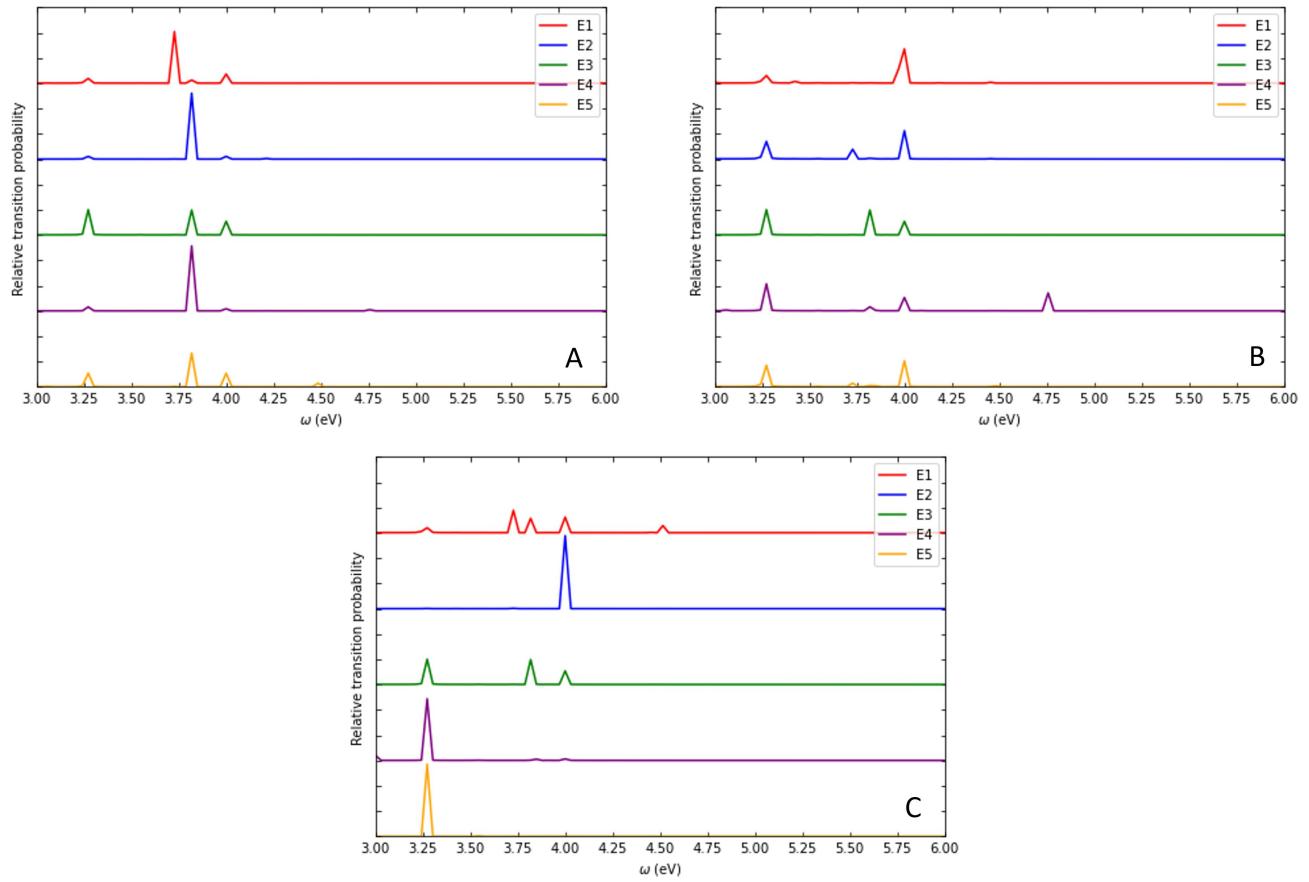


Figure 7.10: Relative transition probability (ordinate) versus ω (abscissa) for $\text{Cd}_{54}\text{Se}_{54}$ in the presence of electric fields aligned along the x-direction (Subplot A), y-direction (Subplot B), and z-direction (Subplot C).

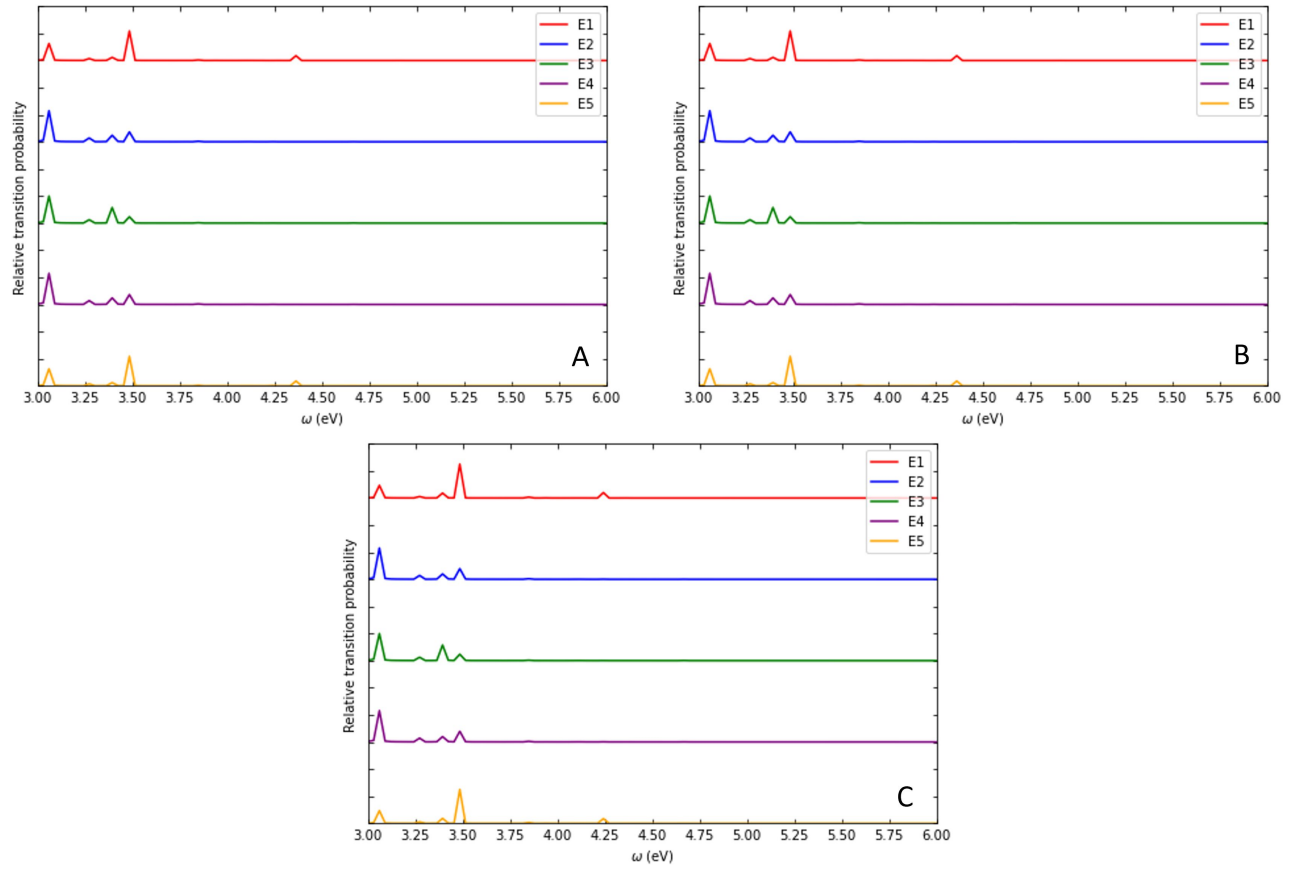


Figure 7.11: Relative transition probability (ordinate) versus ω (abscissa) for $\text{Pb}_{44}\text{S}_{44}$ in the presence of electric fields aligned along the x-direction (Subplot A), y-direction (Subplot B), and z-direction (Subplot C).

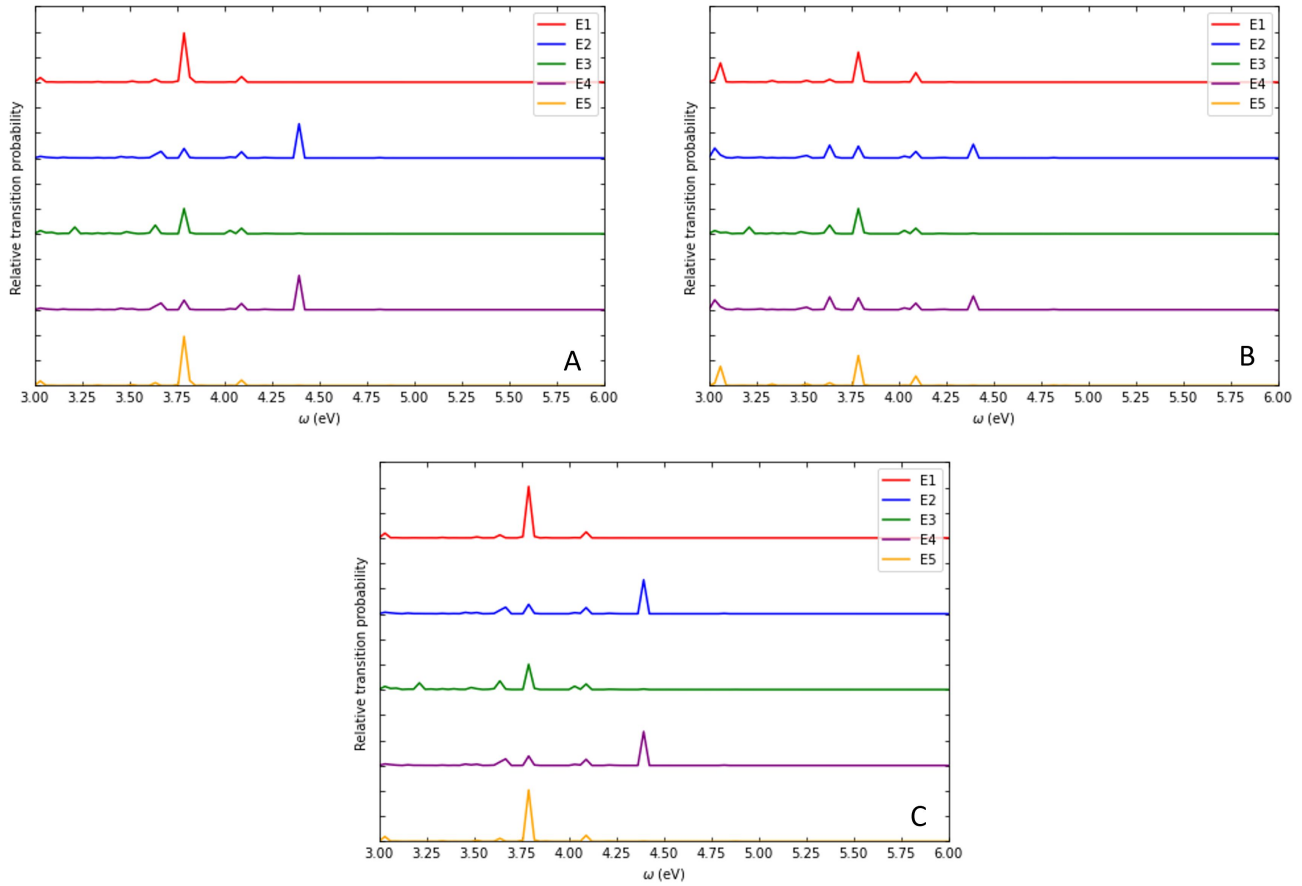


Figure 7.12: Relative transition probability (ordinate) versus ω (abscissa) for $\text{Pb}_{140}\text{S}_{140}$ in the presence of electric fields aligned along the x-direction (Subplot A), y-direction (Subplot B), and z-direction (Subplot C).

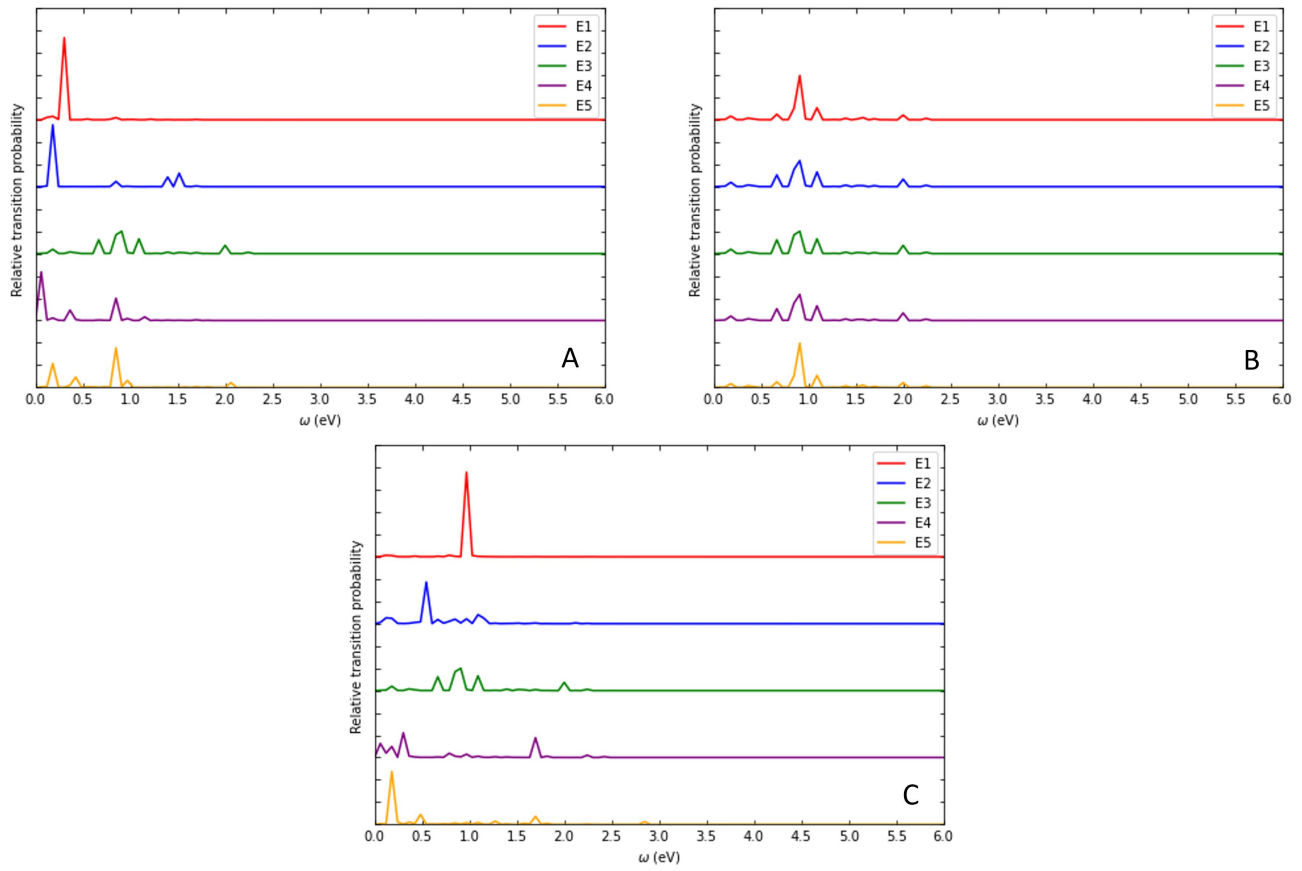


Figure 7.13: Relative transition probability (ordinate) versus ω (abscissa) for $\text{Pb}_{29}\text{Se}_{29}$ in the presence of electric fields aligned along the x-direction (Subplot A), y-direction (Subplot B), and z-direction (Subplot C).

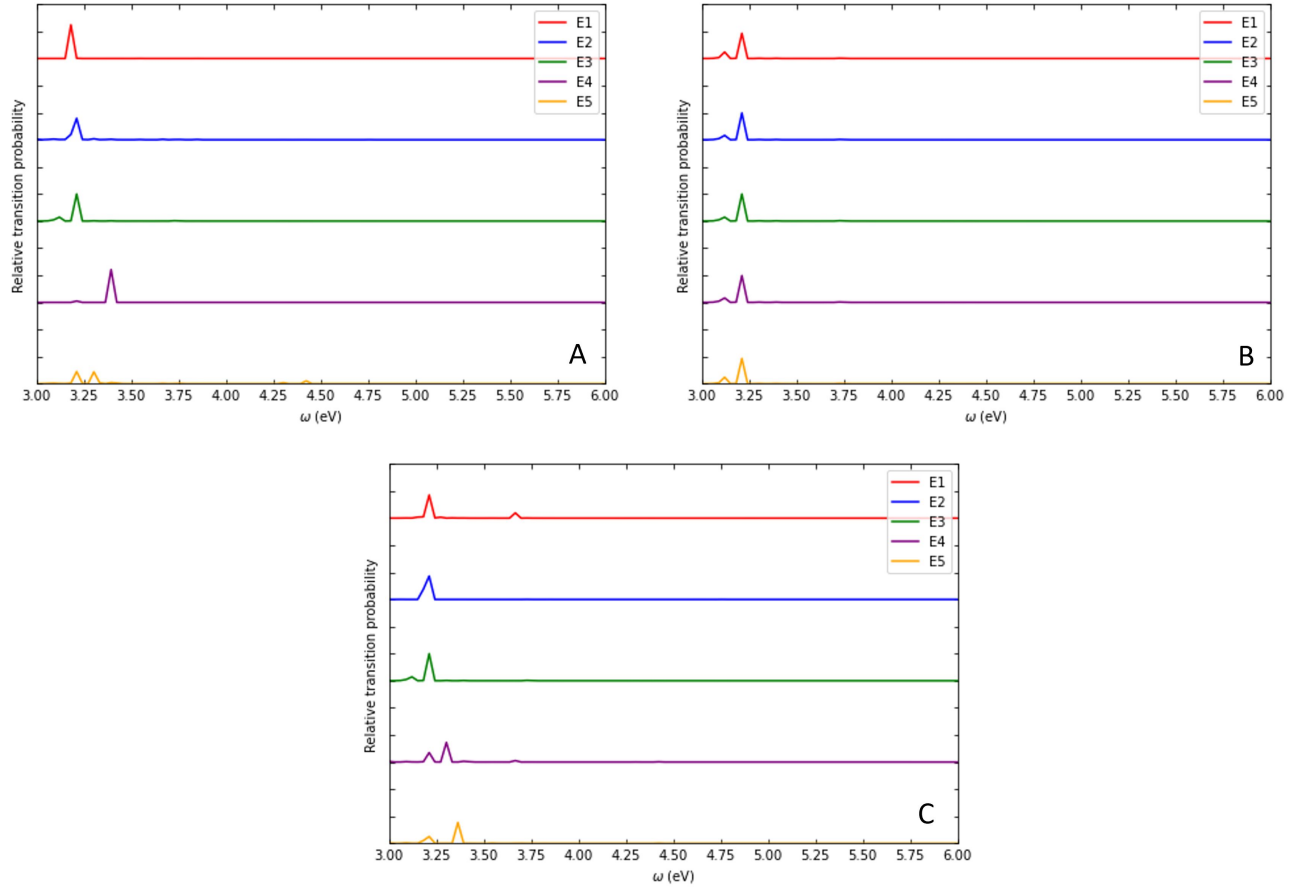


Figure 7.14: Relative transition probability (ordinate) versus ω (abscissa) for $\text{Pb}_{52}\text{Se}_{52}$ in the presence of electric fields aligned along the x-direction (Subplot A), y-direction (Subplot B), and z-direction (Subplot C).

Enhancement of light–matter interaction using directed Stark field

The direction of the applied Stark field can be used to enhance light–matter coupling and increase the spontaneous emission characteristic of the QDs. We demonstrated this phenomenon by calculating the cumulative change in the IPE spectra (Equation 7.3) as a function of Stark field direction while restricting the field strength to $10^{-5}E_{\text{au}}$. A search over a set of directions was performed, and the direction corresponding to the maximum change in the IPE lineshape over the entire frequency range was selected. We refer to this direction as the maximally coupled direction because this directed Stark field induced the most significant change in the light–matter interaction in the QDs. The IPE spectra for $\text{Cd}_{24}\text{S}_{24}$ in the presence of the maximally coupled field displayed the greatest

Table 7.4: Overall change in the IPE spectra for maximally coupled directed Stark fields (Equation 7.3).

Chemical System	$\Delta g_{\text{lineshape}}$	Optimized Stark field direction
$\text{Cd}_{24}\text{S}_{24}$	193%	$[\frac{1}{\sqrt{3}}, -\frac{1}{\sqrt{3}}, -\frac{1}{\sqrt{3}}]$
$\text{Cd}_{45}\text{S}_{45}$	189%	$[0, 1, 0]$
$\text{Cd}_{24}\text{Se}_{24}$	115%	$[0, -\frac{1}{\sqrt{2}}, -\frac{1}{\sqrt{2}}]$
$\text{Cd}_{54}\text{Se}_{54}$	103%	$[-\frac{1}{\sqrt{2}}, 0, -\frac{1}{\sqrt{2}}]$
$\text{Pb}_{44}\text{S}_{44}$	66%	$[-\frac{1}{\sqrt{3}}, -\frac{1}{\sqrt{3}}, -\frac{1}{\sqrt{3}}]$
$\text{Pb}_{140}\text{S}_{140}$	148%	$[\frac{1}{\sqrt{3}}, \frac{1}{\sqrt{3}}, -\frac{1}{\sqrt{3}}]$
$\text{Pb}_{29}\text{Se}_{29}$	155%	$[-\frac{1}{\sqrt{3}}, -\frac{1}{\sqrt{3}}, \frac{1}{\sqrt{3}}]$
$\text{Pb}_{52}\text{Se}_{52}$	189%	$[\frac{1}{\sqrt{2}}, -\frac{1}{\sqrt{2}}, 0]$

enhancement of light–matter coupling (193%), while $\text{Pb}_{44}\text{S}_{44}$ displayed the least enhancement (66%). In figures 7.15–7.18, the IPE spectra (relative transition probability versus ω) are displayed for the CdS, CdSe, PbS, and PbSe quantum dots when in the presence an electric field direction with which they are maximally-coupled. The spectra for when an external electric field is absent (E3) are also displayed in these plots. Again, it is important to note that the maximally-coupled electric field direction does not necessarily correspond to the field that results in the largest total relative transition probability. Instead, the field directions with which the dots are maximally-coupled produce the largest change in the maximum relative transition probabilities compared to maximum relative transition probabilities observed in the absence of an electric field.

For most of the quantum dots, the presence of the maximally-coupled electric field produces a noticeable shift in the energy of the emitted photon compared to energy of the emitted photon in the absence of an electric field, as is verified by Figure 7.15–Figure 7.18. For example, in subplot A of Figure 7.15 we see that when the $\text{Cd}_{24}\text{S}_{24}$ is in the presence of the maximally-couple field, the most probable energy of the emitted photon is 3.939 eV, while in the absence of an electric the most probable energy of the emitted photon is 3.091 eV. It is of paramount importance to note that these maximally-coupled electric fields are fields that result in either the greatest enhancement or de-enhancement of the inverse photoemission processes. For example, the maximally-coupled electric fields de-enhance the IPE processes in the $\text{Pb}_{44}\text{S}_{44}$ and $\text{Pb}_{140}\text{S}_{140}$ dots (Figure 7.17). Conversely, the maximally-coupled electric fields enhance the IPE processes in the CdS, CdSe,

and PbSe QDs. In particular, especially strong enhancement of the IPE processes is observed for $\text{Cd}_{24}\text{S}_{24}$ (Figure 7.15) and $\text{Pb}_{29}\text{Se}_{29}$ (Figure 7.18).

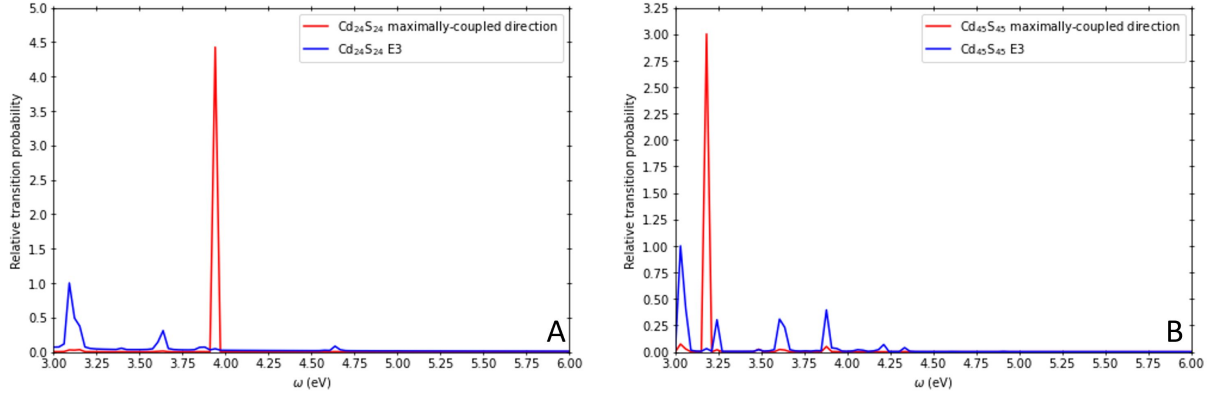


Figure 7.15: Relative transition probability versus ω for $\text{Cd}_{24}\text{S}_{24}$ (subplot A) and $\text{Cd}_{45}\text{S}_{45}$ (subplot B), in the presence of electric fields with which the dots are maximally coupled, along with the spectra for the E3 field.

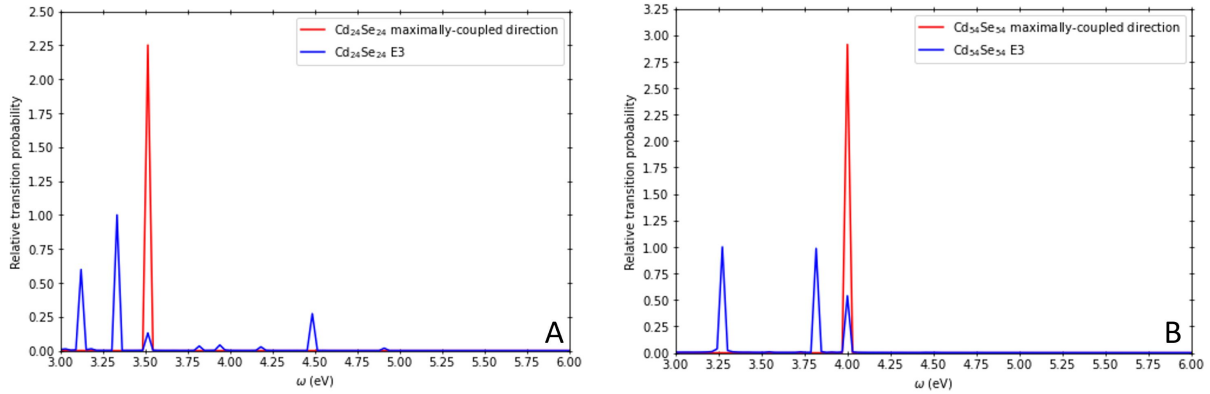


Figure 7.16: Relative transition probability versus ω for $\text{Cd}_{24}\text{Se}_{24}$ (subplot A) and $\text{Cd}_{54}\text{Se}_{54}$ (subplot B), in the presence of electric fields with which the dots are maximally coupled, along with spectra for the E3 field.

We also see that when in the presence of the maximally-coupled fields the number of prominent peaks in the inverse PE spectra, for all of the systems studied, decreases compared to when an external electric field is absent. In subplot A of Figure 7.15, we see that there is one dominant peak, at 3.939 eV, of the spectrum for $\text{Cd}_{24}\text{S}_{24}$ in the presence of the maximally-coupled field, while there are multiple prominent peaks when an external field is absent. In subplot B of Figure 7.15, we also see that there is also only one dominant peak, at 3.182 eV, of the inverse PE spectrum for $\text{Cd}_{45}\text{S}_{45}$

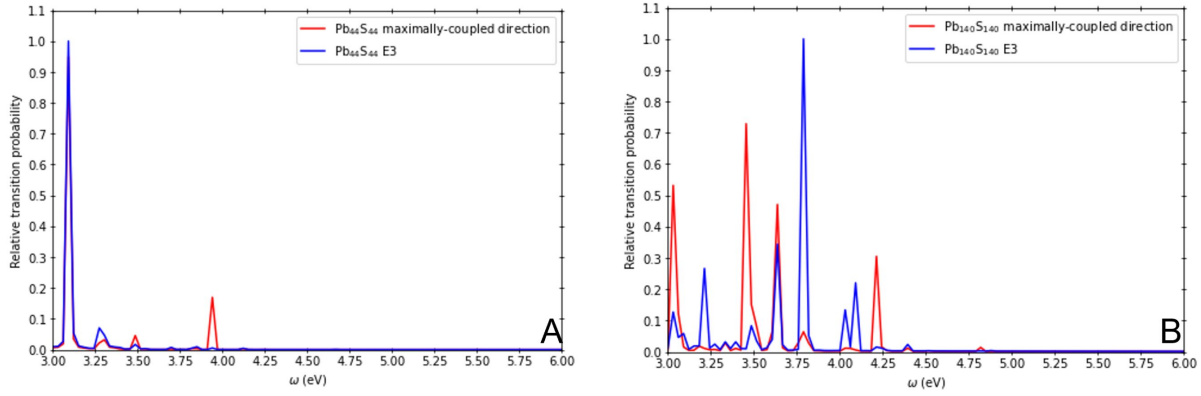


Figure 7.17: Relative transition probability versus ω for $\text{Pb}_{44}\text{S}_{44}$ (subplot A) and $\text{Pb}_{140}\text{S}_{140}$ (subplot B), in the presence of electric fields with which the dots are maximally coupled, along with spectra for the E3 field.

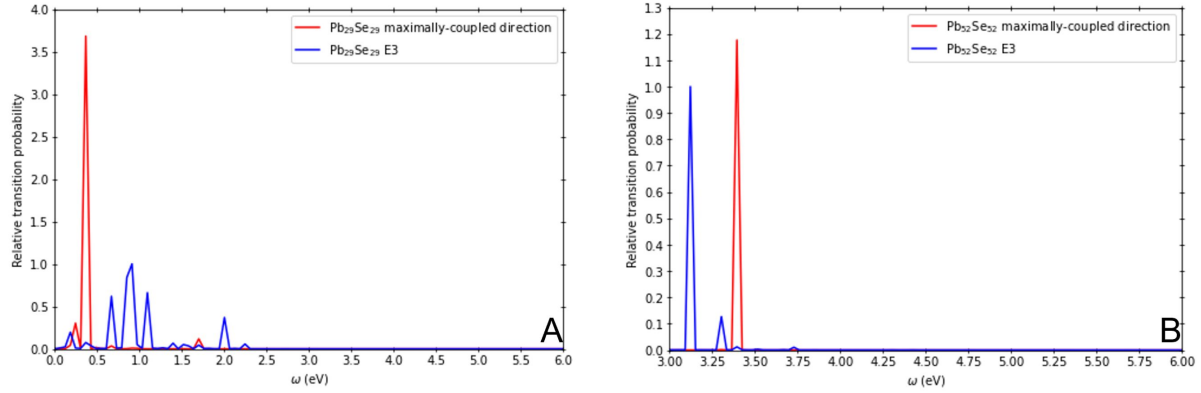


Figure 7.18: Relative transition probability versus ω for $\text{Pb}_{29}\text{Se}_{29}$ (subplot A) and $\text{Pb}_{52}\text{Se}_{52}$ (subplot B), in the presence of electric fields with which the dots are maximally coupled, along with spectra for the E3 field.

in the presence of the maximally-coupled field, but multiple prominent peaks are observed when an external field is absent.

In subplot A of [Figure 7.16](#), we see that there is one dominant peak, at 3.515 eV, of the spectrum for $\text{Cd}_{24}\text{Se}_{24}$ in the presence of the maximally-coupled field, while there are multiple prominent peaks when an external field is absent. In subplot B of [Figure 7.16](#), again we see that there is only one dominant peak, at 4.000 eV, for the spectrum for $\text{Cd}_{54}\text{Se}_{54}$ in the presence of the maximally-coupled field, but again we see that multiple prominent peaks are observed when an external field is absent.

By examination of subplot A of [Figure 7.17](#), we see that there are two prominent peaks of the spectrum for $\text{Pb}_{44}\text{S}_{44}$ in the presence of the maximally-coupled field. The most dominant peak for $\text{Pb}_{44}\text{S}_{44}$ in the presence of the maximally-coupled field and in the absence of an external field both occur at 3.091 eV. We also observe a peak at approximately 3.90 eV, on the spectrum for $\text{Pb}_{44}\text{S}_{44}$, in the presence of the maximally-coupled field. This particular peak is not present in the inverse

PE spectrum of this dot when an external electric field is absent. In subplot B of [Figure 7.17](#), we see that there are multiple prominent peaks on the spectrum $\text{Pb}_{140}\text{S}_{140}$ in the presence of the maximally-coupled field. The most prominent peak observed for this systems spectrum when the maximally-coupled field is present occurs at 3.455 eV. Additionally, by comparing subplot B of [Figure 7.5](#) and subplot B of [Figure 7.17](#) we observe that the peaks of the spectrum for $\text{Pb}_{140}\text{S}_{140}$ in the absence of an external field, occurring at approximately 3.05 eV and 3.65 eV, are greatly enhanced when the maximally-coupled field is present.

In subplot A of [Figure 7.18](#), we see that there is one dominant peak at 0.364 eV on the spectrum for $\text{Pb}_{29}\text{Se}_{29}$ in the presence of the maximally-coupled field, while there are multiple prominent peaks when an external field is absent. In subplot B of [Figure 7.18](#), we also see that there is also only one dominant peak, at 3.394 eV, of the inverse PE spectrum for $\text{Pb}_{52}\text{Se}_{52}$ in the presence of the maximally-coupled field, while two prominent peaks are observed when an external field is absent. Additionally, we observe that for $\text{Pb}_{29}\text{Se}_{29}$ in the presence of the maximally-coupled field, the most probably energy of the emitted photon is 0.545 eV less than the most probable energy of the photon emitted when an external field is absent. When $\text{Pb}_{52}\text{Se}_{52}$ is in the presence of the maximally-coupled field, the most probably energy of the emitted photon is 0.182 eV greater than the most probable energy of the photon emitted when an external field is absent. When in the presence of the maximally-coupled fields, the number of prominent peaks in the inverse PE spectra of all of the systems studied, decreases compared to when an external electric field is absent.

7.5 Discussion

Spontaneous photon emission and enhancement of light–matter coupling: As compared to photoluminescence spectroscopy which involves both spontaneous and stimulated photon emission, IPE spectroscopy is unique because it involves only the spontaneous emission of a photon. This provides a remarkable experimental opportunity to solely investigate the spontaneous emissive characteristics of quantum dots. However, the absence of an incoming radiation field also introduces new challenges in controlling the light–matter interactions which can otherwise be achieved by changing the intensity, power, frequency, and other optical characteristics of the incident radiation field. In this work, we have demonstrated that the application of Stark fields can significantly enhance light–matter interactions and favorably impact the IPE process. Specifically, we have identified field directions that result in the greatest enhancement of light–matter interactions for CdS, CdSe, PbS, and PbSe QDs, and we have found a significant increase in the IPE transition probabilities for these systems ([Table 7.4](#)). These results demonstrate that the customization of IPE transition probabilities can be achieved by systematically applying Stark fields, which can be relevant for electroluminescence applications.[\[128\]](#)

Accessing unoccupied states with low particle-hole oscillator strengths: As opposed to absorption spectroscopy, IPE spectroscopy does not require a radiation field to induce particle-hole excitations to generate electronically excited states. Consequently, IPE can be used to investigate particle–hole excited states with low oscillator strengths which are optically dark. In conjunction with photoluminescence spectroscopic techniques, IPE spectroscopy can be used to generate enhanced maps of optically bright and dark low-lying excited electronic states in QDs. Knowledge about excited states with low oscillator strengths can also aid in attaining greater insight into the electrochemical and cyclic voltammetric characteristics of quantum dots. [\[36, 85, 63, 48, 69\]](#)

Photon emission with sub-bandgap energies: One of the distinguishing characteristics of the IPE process is that photon emission occurs due to unoccupied-to-unoccupied level transitions. Consequently, because of the intra-band nature of the transitions, the IPE process can potentially generate photons with energies smaller than the bandgap in wide-bandgap semiconductor materials. For example, in QDs, the HOMO–LUMO gaps for $\text{Pb}_{44}\text{S}_{44}$ and $\text{Pb}_{140}\text{S}_{140}$ were found to be 6.30 and 5.6 eV, respectively, while the energies of the emitted photons, resulting from the IPE process, were found to be 3.1 and 3.8 eV, respectively (Table 7.3).

Stark field control of intra-band transition: The application of a Stark field can be used not only to increase the intensity of the IPE transition (Table 7.2) but also to change the frequency of the emitted photon (Table 7.3). This provides an exciting opportunity for narrow-bandgap materials to optimize the IPE transitions to have a strong spectral overlap with interband particle–hole transitions. For example, in the case of $\text{Cd}_{54}\text{Se}_{54}$, the HOMO–LUMO gap is 1.8 eV and field-free IPE photon energy is 3.3 eV. We also demonstrate, for $\text{Cd}_{54}\text{Se}_{54}$, that the application of a directed Stark field can facilitate an increase in the IPE photon energy from 3.3 to 4.0 eV (Table 7.3).

7.6 Future Directions

In future works, the methodology presented here can be used to investigate the inverse photoemission processes in a greater variety of materials. Furthermore, because of the observed enhancement in the IPE transition probabilities for these dots, due the application of the maximally-coupled electric fields, future investigation into this effect for a greater variety of fields, and also a greater range of dot sizes may be warranted. Additionally, the effect of the presence of alternating current fields on the IPE transition probabilities and emitted photon energies can be investigated for a variety of materials in the future.

Chapter 8

Nonlinear Stark effect and field-assisted photoionization in PbS semiconductor quantum dots

8.1 Scope of Chapter Content

This chapter presents a theoretical and computational investigation into field-assisted photoionization in PbS quantum dots. In particular, we investigated how the IPs, for ionization from the HOMO, of Pb_4S_4 , $\text{Pb}_{44}\text{S}_{44}$, and $\text{Pb}_{140}\text{S}_{140}$ are impacted by the application of non-ionizing Stark fields, of differing strengths and directions. The ability to control the position of energy levels in quantum dots is of great importance for the optimization of optoelectronic devices. In order to obtain a first-order approximation to the field-dependent Green's function IPs, of these PbS systems, we employed the recently developed SSE-MO method accompanied by the use of a Padé approximation. The results presented in this chapter suggest that the ionization potentials of PbS quantum dots can be controlled by carefully fine-tuning the magnitude and direction of external static electric fields.

8.2 Introduction

When in the presence of an external electric field, the optical and electronic properties of chemical systems are altered. This phenomenon is known as the Stark effect. In many-electron systems, electronic and optical properties display a non-linear dependence on the strength of an external electric field (nonlinear Stark effect). For quantum dots, this effect is usually referred to as the quantum-confined Stark effect. [75, 12, 10] The effects of external electric fields on the optical properties of quantum dots have been investigated in previous works. [75, 10, 34, 41] It has also been demonstrated that some properties of nanomaterials such as photoconductivity and photoluminescence intensity can be modulated by the application of an external electric field. Additionally, the relationship between QD ionization in the presence of an electric field and fluorescence quenching has also been a topic of interest. Although the processes of ionization and exciton ionization has been observed in nanomaterials when in the presence of an external electric field, an in depth investigation into the relationship between the strength and direction of static external electric fields and the ionization potentials, for ionization from the HOMO, of PbS quantum dots has not yet been conducted. [90, 67, 108, 52, 97]

This chapter presents a theoretical and computational investigation into how the IPs, for ionization from the HOMO, of Pb_4S_4 , $\text{Pb}_{44}\text{S}_{44}$, and $\text{Pb}_{140}\text{S}_{140}$ are impacted by the application of

Stark fields of differing strengths and directions. In particular, we examined this relationship for electric fields aligned along axes either parallel or orthogonal with respect to the expectation value of the dipole moment operator of the HOMOs of these PbS systems. Additionally, we investigated how the IPs, for ionization from the HOMO, are impacted by external electric fields aligned with these systems along the x, y, or z axis. A first-order approximation to the field-dependent IPs were obtained, by single-shot solution of the Dyson equation using the recently published SSE-MO method, in conjunction with the use of a Padé approximation [114]. The use of the Padé approximation, as outlined in the Theory section of this chapter, enables the calculation of sufficiently accurate field-dependent IPs, in an extremely efficient manner. By comparing the IPs obtained from the use of the Padé approximation with the field-dependent IPs obtained from the single-shot solution of the Dyson equation, we demonstrate that sufficiently accurate approximations to IPs can be obtained using a Padé approximation to the field-dependent self-energy.

8.3 Theory

Field-dependent self-energy operator

To account for the affect of the external electric fields we define the field-dependent Fock operator as,

$$\hat{f}^{\text{field-on}} = \hat{f}^{\text{field-off}} - \mathbf{E} \cdot \mathbf{r} \quad (8.1)$$

where \mathbf{r} is the position operator and \mathbf{E} is an electric field vector. The components of both \mathbf{r} and \mathbf{E} are in atomic units. The field-dependent dressed orbitals and energies were obtained by diagonalizing the field-on Fock operator.

$$\hat{f}^{\text{field-on}} |\chi_p^{\text{field-on}}\rangle = \epsilon_p^{\text{field-on}} |\chi_p^{\text{field-on}}\rangle \quad (8.2)$$

We then define the field-dependent self-energy as given in Equation 8.3.

$$\begin{aligned} \Sigma_{ii}^{(2),\text{field-on}}(\omega) = & \frac{1}{2} \sum_{jab} \frac{\langle i^{\text{field-on}} j^{\text{field-on}} | r_{12}^{-1} | a^{\text{field-on}} b^{\text{field-on}} \rangle_A \langle a^{\text{field-on}} b^{\text{field-on}} | r_{12}^{-1} | i^{\text{field-on}} j^{\text{field-on}} \rangle_A}{\omega + \epsilon_j^{\text{field-on}} - \epsilon_a^{\text{field-on}} - \epsilon_b^{\text{field-on}}} \\ & + \frac{1}{2} \sum_{jak} \frac{\langle i^{\text{field-on}} a^{\text{field-on}} | r_{12}^{-1} | j^{\text{field-on}} k^{\text{field-on}} \rangle_A \langle j^{\text{field-on}} k^{\text{field-on}} | r_{12}^{-1} | i^{\text{field-on}} a^{\text{field-on}} \rangle_A}{\omega + \epsilon_a^{\text{field-on}} - \epsilon_j^{\text{field-on}} - \epsilon_k^{\text{field-on}}} \end{aligned} \quad (8.3)$$

In this work, we use only the field-dependent orbital energies to construct the self-energy. This serves as a first-order approximation to the Green's function IP when the external electric fields are present. The first-order approximation for the field-dependent self-energy is displayed in Equation 8.4.

$$\begin{aligned} \Sigma_{ii}^{(2),\text{field-on,PT1}}(\omega) = & \frac{1}{2} \sum_{jab} \frac{\langle ij | r_{12}^{-1} | ab \rangle_A \langle ab | r_{12}^{-1} | ij \rangle_A}{\omega + \epsilon_j^{\text{field-on}} - \epsilon_a^{\text{field-on}} - \epsilon_b^{\text{field-on}}} \\ & + \frac{1}{2} \sum_{jak} \frac{\langle ia | r_{12}^{-1} | jk \rangle_A \langle jk | r_{12}^{-1} | ia \rangle_A}{\omega + \epsilon_a^{\text{field-on}} - \epsilon_j^{\text{field-on}} - \epsilon_k^{\text{field-on}}} \end{aligned} \quad (8.4)$$

Padé approximation to field-dependent self-energy operator

In addition to the full field-dependent self-energy operator, we also present an approximate derivation based on the Padé approximation. We start with the diagonal approximation to the Dyson equation and define the reduced self-energy operator $R^{\text{field-on}}$ as,

$$R(E) = \frac{\Sigma^{\text{field-on}}(E)}{\omega_0^{\text{field-on}}(E)} \quad (8.5)$$

$$\omega^{\text{field-on}} = \omega_0^{\text{field-on}} + \omega_0^{\text{field-on}} R^{\text{field-on}}(E) \quad (8.6)$$

By expressing both the numerator and denominator a series expansion in E we obtain,

$$R(E) = \frac{\Sigma^{\text{field-on}}(E)}{\omega_0^{\text{field-on}}(E)} = \frac{\Sigma^{\text{field-off}} + \alpha_1 E + \alpha_2 E^2 + \dots}{\omega_0^{\text{field-off}} + \beta_1 E + \beta_2 E^2 + \dots} \quad (8.7)$$

However, because of the non-linearity of the Stark effect, the coefficients for the linear terms can be ignored so that,

$$\alpha_1 = \beta_1 = 0 \quad (8.8)$$

which implies,

$$\frac{\Sigma^{\text{field-on}}(E)}{\omega_0^{\text{field-on}}(E)} = \frac{\Sigma^{\text{field-off}} + \alpha_2 E^2}{\omega_0^{\text{field-off}} + \beta_2 E^2} = \gamma_0 + \gamma_1 E + \dots \quad (8.9)$$

By taking the first derivative of [Equation 8.9](#) we obtain $\gamma_1(E)$ which is given below in [Equation 8.10](#).

$$\gamma_1(E) = \frac{d}{dE} \left(\frac{\Sigma^{\text{field-off}} + \alpha_2 E^2}{\omega_0^{\text{field-off}} + \beta_2 E^2} \right) = \frac{2\alpha_2 E}{\omega_0^{\text{field-off}} + \beta_2 E^2} - 2\beta_2 E \frac{\Sigma^{\text{field-off}} + \alpha_2 E^2}{(\omega_0^{\text{field-off}} + \beta_2 E^2)^2} \quad (8.10)$$

Note that,

$$\gamma_1(E = 0) = 0 \quad (8.11)$$

which implies, that up to first order, the following expression is true.

$$\frac{\Sigma^{\text{field-on}}(E)}{\omega_0^{\text{field-on}}(E)} = \frac{\Sigma^{\text{field-off}}}{\omega_0^{\text{field-off}}} \quad (8.12)$$

We define the Padé approximation to the field-dependent self-energy operator as follows.

$$\Sigma^{\text{field-on,PA}}(E) = \gamma_0 \omega_0^{\text{field-on}}(E) \quad (8.13)$$

where,

$$\gamma_0 = \frac{\Sigma^{\text{field-off}}}{\omega_0^{\text{field-off}}} \quad (8.14)$$

Upon examination of Equation 8.13 and Equation 8.14, it can be observed that a first-order approximation to the field-dependent self-energy, $\Sigma^{\text{field-on,PA}}(E)$, can be obtained directly from "field-on" Koopmans' IP ($\omega_0^{\text{field-on}}(E)$) and the "field-off" Koopmans' IP ($\omega_0^{\text{field-off}}$) and self-energy ($\Sigma^{\text{field-off}}$). This is a particularly convenient result, which indicates that it is not strictly necessary to construct the self-energy operator, each field investigated. Instead, within the framework of this approximation, we only need to obtain $\omega_0^{\text{field-on}}(E)$ and to construct the self-energy for "field-off" scenarios, for each system investigated. It is relevant to note that $\omega_0^{\text{field-on}}(E)$, for each system, was obtained for each unique field investigated.

Computational details

In Table 8.1, we provide the labels by which we refer to the different electric fields throughout this work in the column labeled Electric Field. The magnitudes of the electric field vectors, in atomic units, are denoted as E_{mag} in Table 8.1. These magnitudes indicate the strengths of the electric fields investigated. It is relevant to note, that the negative sign accompanying some of the field strengths is indicative of the direction that these external electric fields are approaching the dots. For example, an external field that is aligned with a dot along the x-axis, with a strength of -3.0×10^{-2} (E1 field), is approaching the quantum dot from the -x direction, while an external field that is aligned with a dot along the x-axis, with a strength of 3.0×10^{-2} (E7 field), is approaching the quantum dot from the +x direction. Therefore, the fields used for this example are aligned with a quantum dot along the same axis, but approach the QD from opposite ends. The single-particle

Table 8.1: Electric field vector magnitudes

Electric Field	E_{mag} (au)
E1	-3.0×10^{-2}
E2	-2.0×10^{-2}
E3	-1.0×10^{-2}
E4	0.00
E5	1.0×10^{-2}
E6	2.0×10^{-2}
E7	3.0×10^{-2}

states and energies for the PbS quantum dots were obtained from Hartree-Fock calculations using the LANL-2DZ ECP basis. The TeraChem electronic structure package was used to perform these Hartree-Fock calculations for the PbS quantum dots in the absence of an external electric field. Instead of performing AO-to-MO transformations, we evaluated each MO at 1 million points in 3-dimensional Cartesian space and stored the results on a grid. Using these pre-computed grids enables us to perform required integrals in the MO basis using Monte Carlo integration.

8.4 Results and Discussion

Comparison of field-dependent Padé approximation IPs with field-dependent Green's function IPs

In [Figure 8.1](#) we compare the field-dependent IPs obtained using the Padé approximation and the field-dependent Green's function IPs, obtained using the SSE-MO method for $\text{Pb}_{140}\text{S}_{140}$, in the presence of electric fields that are aligned orthogonal with respect to the expectation value of the dipole moment operator of the HOMO. The field-dependent IPs obtained using the Padé approximation are extremely similar to the field-dependent Green's function IPs, obtained using the SSE-MO method, as demonstrated by [Figure 8.1](#). [\[114\]](#) The largest discrepancy between the IPs obtained from the the Padé approximation and the Green's function IPs occurs for the E3 orthogonal field, for which the IP obtained from the Padé approximation is 0.035 eV less than the Green's function IP ([Figure 8.1](#)).

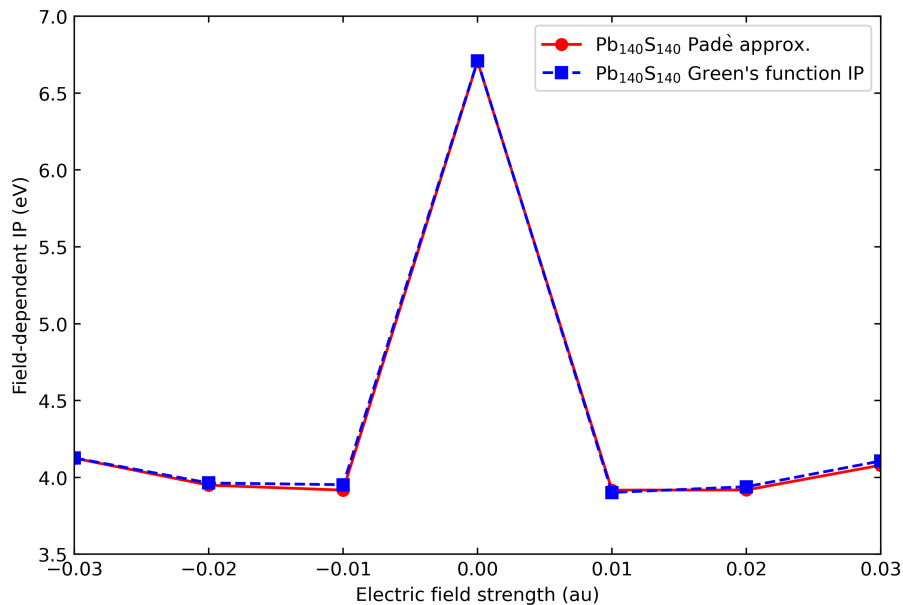


Figure 8.1: Comparison of Padé approximation IPs and Green's function IPs obtained using first-order approximation ([Equation 8.4](#)) and the SSE-MO method, for $\text{Pb}_{140}\text{S}_{140}$. Electric fields are aligned along an axis that is orthogonal with respect to the expectation value of the dipole moment operator of the HOMO.

In this section we present results describing the impact of external electric fields, of varying strength and direction, on the IPs of Pb_4S_4 , $\text{Pb}_{44}\text{S}_{44}$, and $\text{Pb}_{140}\text{S}_{140}$, for ionization from their HOMOs. It is important to note that the external electric fields chosen for this investigation are not strong enough to ionize these systems.

In this work, the field-dependent IPs of Pb_4S_4 , $\text{Pb}_{44}\text{S}_{44}$, and $\text{Pb}_{140}\text{S}_{140}$ were determined using the Padé approximation. In [Figure 8.3](#), we demonstrate the dependence of the IPs of these PbS systems on the strength and direction of external electric fields aligned with these dots along axes either parallel or orthogonal with respect to the expectation value of the dipole moment operator

of the HOMOs. In [Figure 8.1](#), we demonstrate that the field-dependent IPs of $\text{Pb}_{140}\text{S}_{140}$, obtained from the use of the Padé approximation, are comparable to the field-dependent Green's function IPs obtained using the SSE-MO method. Additionally, we demonstrate how the IPs, for ionization from the HOMO, are impacted when external electric fields are aligned with these PbS systems along the x, y, or z axes ([Figure 8.4](#)).

Impact of external Stark field aligned parallel or orthogonal with respect to the expectation value of the dipole moment operator of the HOMO

The IPs of Pb_4S_4 are very similar for both the weakest parallel and orthogonal fields, while for the stronger fields, we observe a greater difference between the IPs of Pb_4S_4 for the parallel and orthogonal fields, as is demonstrated by [Figure 8.2](#). In the presence of the E6 and E7 orthogonal fields, the IPs of Pb_4S_4 are lower than the IPs observed for the parallel fields with these same strengths. Conversely, when in the presence of the E1 and E2 parallel fields, the IPs of Pb_4S_4 are slightly lower than the IPs observed for the orthogonal fields with these same strengths ([Figure 8.2](#)). The IPs of $\text{Pb}_{44}\text{S}_{44}$ when in the presence of the parallel fields are very similar to the IPs observed for the orthogonal fields, for both weaker and stronger fields ([Figure 8.2](#)). When the $\text{Pb}_{140}\text{S}_{140}$ dot is in the presence of the E1, E2, E6, and E7 parallel fields, the IPs observed are lower compared to the IPs observed for the orthogonal electric fields of corresponding strengths ([Figure 8.2](#)). It is relevant to note that the relationship between IP and the strengths of the external parallel and orthogonal fields is nonlinear for Pb_4S_4 , $\text{Pb}_{44}\text{S}_{44}$, and $\text{Pb}_{140}\text{S}_{140}$, as demonstrated in [Figure 8.2](#).

By further examining [Figure 8.2](#), we can compare how the IPs of Pb_4S_4 , $\text{Pb}_{44}\text{S}_{44}$, and $\text{Pb}_{140}\text{S}_{140}$ are impacted by the presence of external electric fields aligned with the dots along axes parallel with respect to the expectation value of the dipole moment operator of their HOMOs. The parallel external electric fields have a greater impact on the IPs of $\text{Pb}_{44}\text{S}_{44}$ and $\text{Pb}_{140}\text{S}_{140}$ compared to the IPs of Pb_4S_4 . Interestingly, we observe that when in the presence of the E1 and E7 parallel fields, the IP of $\text{Pb}_{140}\text{S}_{140}$ is greater than the IP of $\text{Pb}_{44}\text{S}_{44}$. Additionally, we observe that the curves of Field-dependent IP versus Electric field strength, for $\text{Pb}_{44}\text{S}_{44}$ and $\text{Pb}_{140}\text{S}_{140}$, intersect twice. One of these intersections occur when the strength of the external parallel field is between that of the E2 field and E1 field. The second intersection occurs when the strength of the external parallel field is between that of E6 field and the E7 field. This suggests that the IPs of $\text{Pb}_{44}\text{S}_{44}$ and $\text{Pb}_{140}\text{S}_{140}$ are equivalent when in the presence of parallel external static fields with strengths corresponding to the values at which these intersections occur. The IPs of Pb_4S_4 and $\text{Pb}_{44}\text{S}_{44}$ decrease as the strength of the external electric field increases ([Figure 8.2](#)).

In [Figure 8.3](#), we compare how the IPs of Pb_4S_4 , $\text{Pb}_{44}\text{S}_{44}$, and $\text{Pb}_{140}\text{S}_{140}$ are impacted by external electric fields aligned along axes orthogonal with respect to the expectation value of the dipole moment operator of their HOMOs. Similar to the trend observed for the parallel fields, we observe that the presence of the orthogonal external electric fields have a greater impact on the IPs of $\text{Pb}_{44}\text{S}_{44}$ and $\text{Pb}_{140}\text{S}_{140}$ compared to the IPs of Pb_4S_4 , as is demonstrated in [Figure 8.3](#). When in the presence of fields with strengths between that of the E1 and E2 orthogonal fields, the IP of $\text{Pb}_{140}\text{S}_{140}$ is greater than the IP of $\text{Pb}_{44}\text{S}_{44}$. This is also observed for some orthogonal fields with strengths between that of the E6 and E7 fields. We also observe that the curves of Field-dependent IP versus Electric field strength, for $\text{Pb}_{44}\text{S}_{44}$ and $\text{Pb}_{140}\text{S}_{140}$, intersect twice. These intersections occur when the strength of the external orthogonal field strengths are close to the strengths of the E2 and E6 fields. This suggests that the IPs of $\text{Pb}_{44}\text{S}_{44}$ and $\text{Pb}_{140}\text{S}_{140}$ are identical when in the

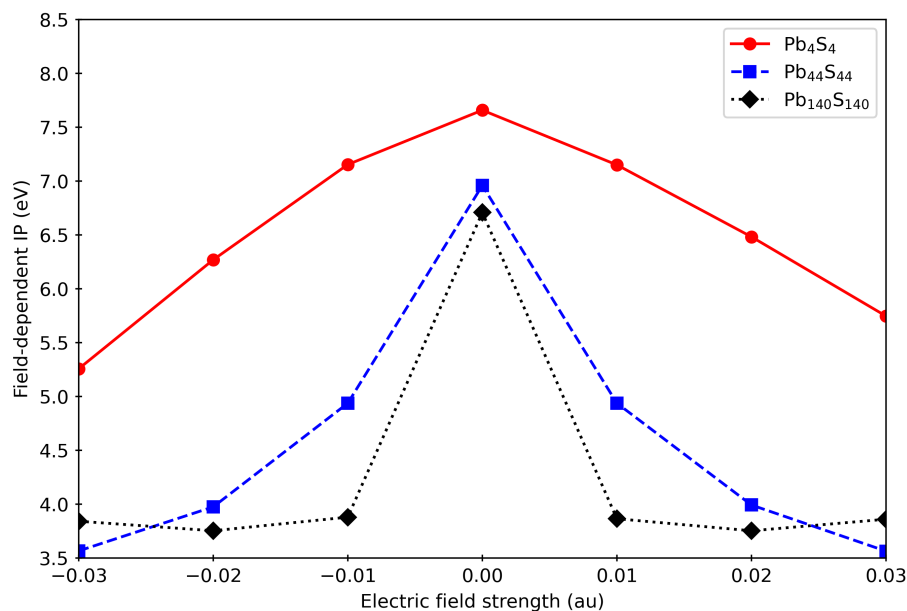


Figure 8.2: Impact of static external electric fields on the ionization potentials of Pb₄S₄, Pb₄₄S₄₄, and Pb₁₄₀S₁₄₀. The fields were aligned with these systems along axes parallel with respect to the expectation value of the dipole moment operator of their HOMOs.

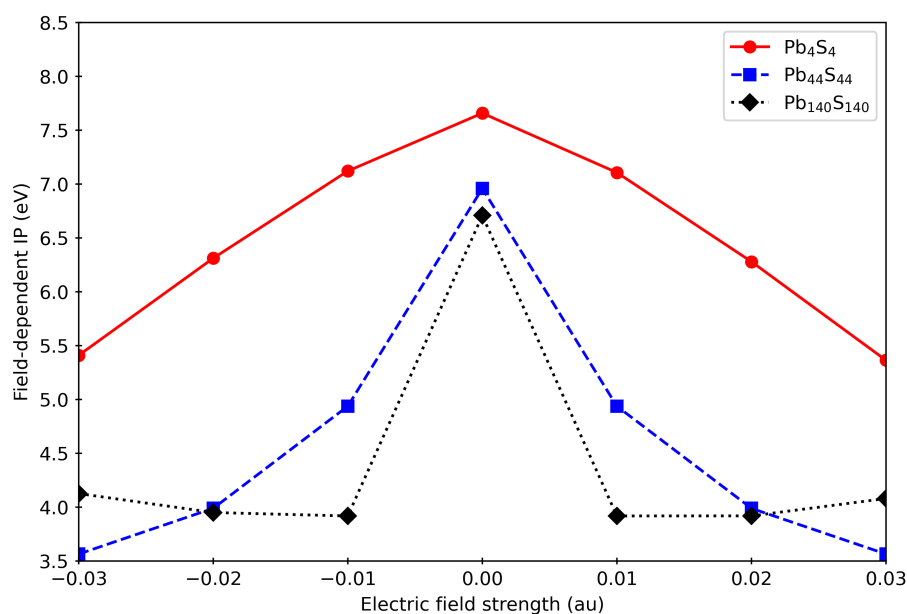


Figure 8.3: Impact of static external electric fields on the ionization potentials of Pb₄S₄, Pb₄₄S₄₄, and Pb₁₄₀S₁₄₀. The fields were aligned with these systems along axes orthogonal with respect to the expectation value of the dipole moment operator of their HOMOs.

presence of some orthogonal external static fields with strengths that correspond to the locations at which these intersections occur. Similar to what was observed for the parallel fields, in [Figure 8.3](#)

we see that the IPs of Pb_4S_4 and $\text{Pb}_{44}\text{S}_{44}$ decrease as the strength of the external electric field increases.

Impact of external Stark field aligned along the x, y, and z axis

In figure [Figure 8.4](#), we examine how the IPs of Pb_4S_4 , $\text{Pb}_{44}\text{S}_{44}$, and $\text{Pb}_{140}\text{S}_{140}$ are affected by the presence of external electric fields aligned with these dots along the x, y, or z axis. The IPs of Pb_4S_4 are similarly impacted by the presence of electric fields of corresponding strengths aligned along either the x, y, or z axis ([Figure 8.4](#)).

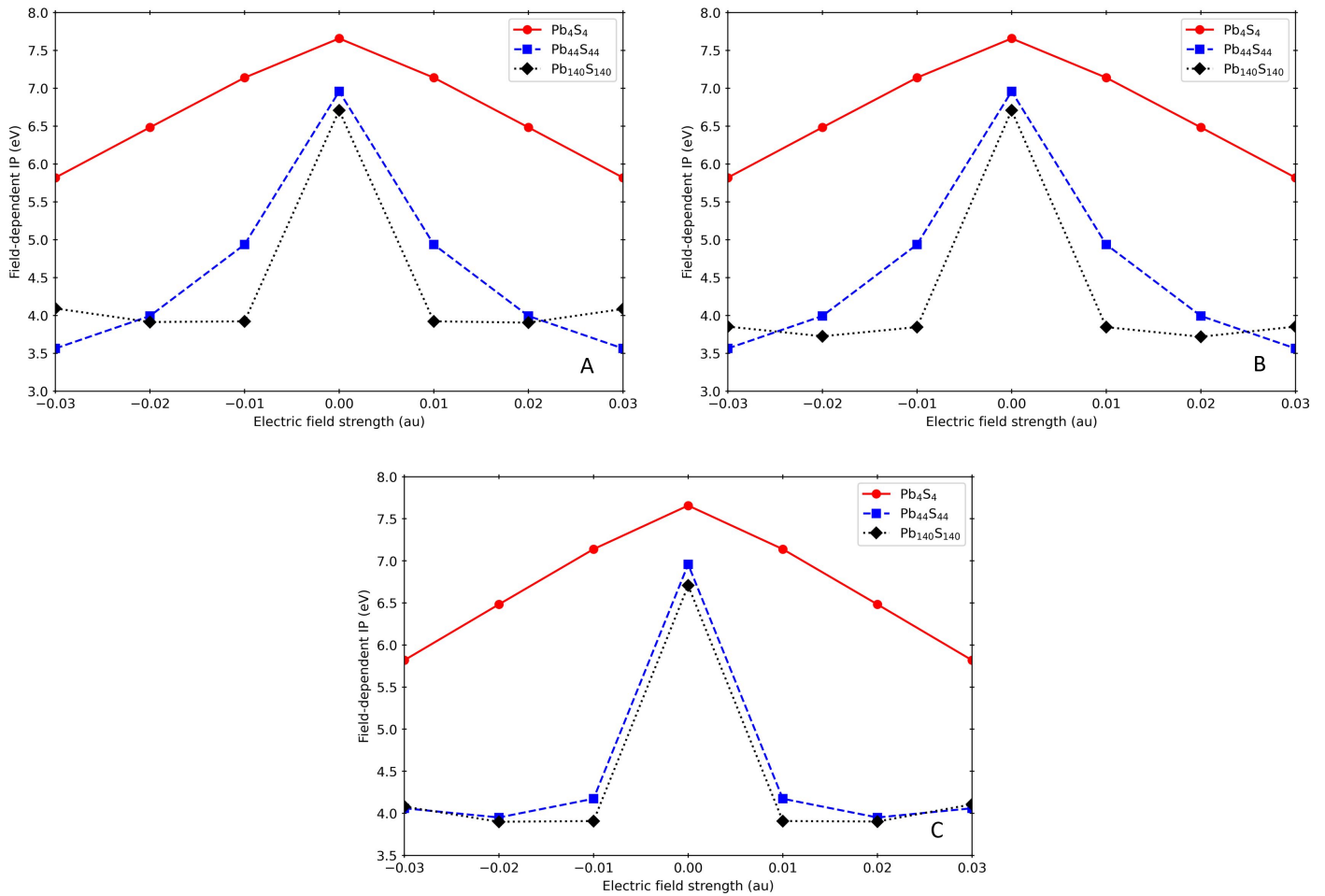


Figure 8.4: Inter-system comparison of the impact of static external electric fields on the ionization potentials of Pb_4S_4 , $\text{Pb}_{44}\text{S}_{44}$, and $\text{Pb}_{140}\text{S}_{140}$. The fields were aligned with these systems along the x (subplot A), y (subplot B), or z axes (subplot C).

For fields of corresponding strength aligned with $\text{Pb}_{44}\text{S}_{44}$ along the x and y axes, the IPs are extremely similar, as demonstrated in ([Figure 8.4](#)). Other than for the E1 and E7 fields, the IPs are lower when the external field is aligned with $\text{Pb}_{44}\text{S}_{44}$ along the z axis compared to the situation in which the external field is aligned with the dot along either the x or y axis. Additionally, we see that when in the presence of fields aligned along either the x or y axis, the IP of $\text{Pb}_{44}\text{S}_{44}$ decreases

as field strength increases. When the external fields are aligned with $\text{Pb}_{44}\text{S}_{44}$ along the z axis, we initially observe that the IP of $\text{Pb}_{44}\text{S}_{44}$ decreases as field strength increases, but as the field strength is increased from -0.02 au (E2 field) to -0.03 au (E1 field) and from 0.02 au (E6 field) to 0.03 au (E7 field), we observe an increase in the IP (Figure 8.4).

For fields of corresponding strengths aligned along the x or z axis, the IPs of $\text{Pb}_{140}\text{S}_{140}$ are very similar, as shown in Figure 8.4. Compared to the IPs observed when the fields are aligned with $\text{Pb}_{140}\text{S}_{140}$ along the x or z axis, the IPs of $\text{Pb}_{140}\text{S}_{140}$ are lower when the external fields are aligned with the dot along the y axis. We also observe that in the presence of fields aligned along the x, y, or z direction, the IP of $\text{Pb}_{140}\text{S}_{140}$ initially decreases as field strength increases, but when field strength is increased from -0.02 au (E2 field) to -0.03 au (E1 field) and from 0.02 au (E6 field) to 0.03 au (E7 field), we observe an increase in the IP (Figure 8.4).

Additionally, by examining Figure 8.4 we can compare how the IPs, of Pb_4S_4 , $\text{Pb}_{44}\text{S}_{44}$, and $\text{Pb}_{140}\text{S}_{140}$, are impacted by the presence of external electric fields aligned with these systems along x, y, or z axis. The presence of these static electric fields have a greater impact on the IPs of $\text{Pb}_{44}\text{S}_{44}$ and $\text{Pb}_{140}\text{S}_{140}$ compared to the IPs of Pb_4S_4 . Due to the presence of external electric fields aligned with the dots along the x, y, or z axes, we observe that for $\text{Pb}_{44}\text{S}_{44}$ and $\text{Pb}_{140}\text{S}_{140}$, the curves of field-dependent IP versus electric field strength intersect once when the field strength is between -0.02 au (E2 field) and -0.03 au (E1 field) and again when the field strength is between 0.02 au (E6 field) and 0.03 au (E7 field). Again, we note that the occurrence of these intersections indicate that for the fields aligned along x, y, or z axis, there exists particular field strengths for which the IPs of $\text{Pb}_{44}\text{S}_{44}$ and $\text{Pb}_{140}\text{S}_{140}$ are equivalent. As expected, we observe that the relationship between the IPs of Pb_4S_4 , $\text{Pb}_{44}\text{S}_{44}$, and $\text{Pb}_{140}\text{S}_{140}$ and external field strength is nonlinear for the fields aligned along the x, y, or z axis (Figure 8.4).

8.5 Conclusions

This chapter presented results demonstrating how the IPs, for ionization from the HOMO, of Pb_4S_4 , $\text{Pb}_{44}\text{S}_{44}$, and $\text{Pb}_{140}\text{S}_{140}$ are impacted by the application of Stark fields of differing strengths and directions. Results that demonstrate how the IPs of these PbS systems are impacted by fields of differing strengths, aligned along axes either parallel or orthogonal to the expectation value of the dipole moment operator of their HOMOs, were presented. Additionally, this chapter also presented results demonstrating how the IPs of these systems are impacted by static external electric fields aligned with these systems along either the x, y, or z axis. We employed the use of the Padé approximation to calculate the field-dependent IPs of these PbS systems in an accurate and extremely efficient manner. By using $\text{Pb}_{140}\text{S}_{140}$ in the presence of static external fields that are aligned along an axis orthogonal to the expectation value of the dipole moment operator of the HOMO as an example, we demonstrated that the IPs obtained from the Padé approximation are in good agreement with the first-order approximation to the field-dependent Green's function IPs. It is relevant reiterate that calculating the field-dependent IP using the Padé approximation to the field dependent self-energy, requires only the field-independent self-energy and the field-independent Koopmans' IP along with the field-dependent Koopmans' IP. As a result, a sufficiently accurate approximation to the field-dependent Green's function IPs, for many different external fields, can be obtained without constructing the field-dependent self-energy operator for each of the external fields investigated.

For Pb_4S_4 , we demonstrated that as IP decreases as relative field strength increases for all of the fields studied. Additionally, we found that for $\text{Pb}_{44}\text{S}_{44}$ the IP decreases as the relative strength of the external fields increases for all of the fields studied, with the exception of the field aligned along the z-axis. When the external field is aligned with $\text{Pb}_{44}\text{S}_{44}$ along the z direction, we observed that the IP initially decreased as the relative field strength increased, but then began to increase for the stronger external fields. For all of the fields studied, we found that the IP of $\text{Pb}_{140}\text{S}_{140}$ initially decreased as the relative field strength was increased, but then began to increase for the stronger external fields. Furthermore, for all of the fields studied, we found that the the IPs of $\text{Pb}_{44}\text{S}_{44}$ and $\text{Pb}_{140}\text{S}_{140}$ were more dramatically impacted by the presence of the external static fields compared to the IPs of Pb_4S_4 . Interestingly, the results from this study suggest that for all of the field directions investigated there exist particular relative field strengths, for which the IPs of $\text{Pb}_{44}\text{S}_{44}$ and $\text{Pb}_{140}\text{S}_{140}$ are equivalent.

The results presented in this chapter indicate, that by fine-tuning the direction and magnitude of an external static field, the ionization potentials of materials can be finely controlled. The ability to predict the impact of external electric fields on the positions of energy levels in a material, can be applied for the purpose of enhancing photocatalytic reactions and optimizing photoelectrodes, photomultipliers, and tandem solar cells. It is also relevant to emphasize that the methodology presented here can be adapted in order to predict the field-dependence of other properties of materials, including excitation energies and electron affinities.

Bibliography

- [1] N. Alidoust, M. C. Toroker, and E. A. Carter. “Revisiting photoemission and inverse photoemission spectra of nickel oxide from first principles: Implications for solar energy conversion”. In: *J. Phys. Chem. B* 118.28 (2014), pp. 7963–7971. DOI: [10.1021/jp500878s](https://doi.org/10.1021/jp500878s).
- [2] P.W. Atkins and R.S. Friedman. *Molecular Quantum Mechanics*. OUP Oxford, 2011. ISBN: 9780199541423.
- [3] V. Averbukh, I.B. Müller, and L.S. Cederbaum. “Mechanism of interatomic coulombic decay in clusters”. In: *Phys. Rev. Lett.* 93.26 I (2004). DOI: [10.1103/PhysRevLett.93.263002](https://doi.org/10.1103/PhysRevLett.93.263002).
- [4] E.F. Aziz et al. “Interaction between liquid water and hydroxide revealed by core-hole de-excitation”. In: *Nature* 455.7209 (2008), pp. 89–91. DOI: [10.1038/nature07252](https://doi.org/10.1038/nature07252).
- [5] Rodney J Bartlett. “Towards an exact correlated orbital theory for electrons”. In: *Chem. Phys. Lett.* 484.1-3 (2009), pp. 1–9.
- [6] Michael G Bayne and Arindam Chakraborty. “Development of composite control-variate stratified sampling approach for efficient stochastic calculation of molecular integrals”. In: *arXiv:1804.01197* (2018).
- [7] Michael G. Bayne, John Drogo, and Arindam Chakraborty. “Infinite-order diagrammatic summation approach to the explicitly correlated congruent transformed Hamiltonian”. In: *Phys. Rev. A* 89 (3 Mar. 2014), p. 032515. DOI: [10.1103/PhysRevA.89.032515](https://doi.org/10.1103/PhysRevA.89.032515).
- [8] Michael G. Bayne et al. “Construction of explicitly correlated geminal-projected particle-hole creation operators for many-electron systems using the diagrammatic factorization approach”. In: *Phys. Rev. A* 94 (5 Nov. 2016), p. 052504. DOI: [10.1103/PhysRevA.94.052504](https://doi.org/10.1103/PhysRevA.94.052504).
- [9] Michael G. Bayne et al. “Linked-Cluster Formulation of Electron–Hole Interaction Kernel in Real-Space Representation without Using Unoccupied States”. In: *J. Chem. Theory Comput.* 14.7 (2018), pp. 3656–3666.
- [10] Christopher J. Blanton, Christopher Brenon, and Arindam Chakraborty. “Development of polaron-transformed explicitly correlated full configuration interaction method for investigation of quantum-confined Stark effect in GaAs quantum dots”. In: *J. Chem. Phys.* 138.5 (2013), p. 054114.
- [11] Paul Bratley, Bennet L Fox, and Linus E Schrage. *A guide to simulation*. Springer Science and Business Media, 2011.

- [12] L. Brus. “Quantum crystallites and nonlinear optics”. In: *Applied Physics A Solids and Surfaces* 53.6 (1991). cited By 1070, pp. 465–474. doi: [10.1007/BF00331535](https://doi.org/10.1007/BF00331535).
- [13] D. Cahen and A. Kahn. “Electron Energetics at Surfaces and Interfaces: Concepts and Experiments”. In: *Advanced Materials* 15.4 (2003), pp. 271–277. doi: <https://doi.org/10.1002/adma.200390065>.
- [14] David Cahen, Antoine Kahn, and Eberhard Umbach. “Energetics of molecular interfaces”. In: *Materials Today* 8.7 (2005), pp. 32–41. ISSN: 1369-7021. doi: [https://doi.org/10.1016/S1369-7021\(05\)70985-8](https://doi.org/10.1016/S1369-7021(05)70985-8).
- [15] M.E. Casida and M. Huix-Rotllant. “Progress in time-dependent density-functional theory”. In: *Annu. Rev. Phys. Chem.* 63 (2012), pp. 287–323. doi: [10.1146/annurev-physchem-032511-143803](https://doi.org/10.1146/annurev-physchem-032511-143803).
- [16] Mark E. Casida and Delano P. Chong. “Quasi-particle equation from the configuration-interaction (CI) wave-function method”. In: *Int. J. Quantum Chem.* 40.2 (1991), pp. 225–242. doi: <https://doi.org/10.1002/qua.560400206>.
- [17] L.S. Cederbaum. “Direct calculation of ionization potentials of closed-shell atoms and molecules”. In: *Theoret. Chim. Acta* 31.3 (1973), pp. 239–260. doi: [10.1007/BF00526514](https://doi.org/10.1007/BF00526514).
- [18] L.S. Cederbaum, J. Zobeley, and F. Tarantelli. “Giant intermolecular decay and fragmentation of clusters”. In: *Phys. Rev. Lett.* 79.24 (1997), pp. 4778–4781. doi: [10.1103/PhysRevLett.79.4778](https://doi.org/10.1103/PhysRevLett.79.4778).
- [19] Jiangchao Chen et al. “First-Principles Study of p-n-Doped Silicon Quantum Dots: Charge Transfer, Energy Dissipation, and Time-Resolved Emission”. In: *J. Phys. Chem. Lett.* 4.17 (2013), pp. 2906–2913. doi: [10.1021/jz400760h](https://doi.org/10.1021/jz400760h).
- [20] T.-T. Chen, J. Simons, and K.D. Jordan. “Analysis of the equation-of-motion theory of electron affinities and ionization potentials”. In: *Chem. Phys.* 14.1 (1976), pp. 145–158. doi: [10.1016/0301-0104\(76\)80033-X](https://doi.org/10.1016/0301-0104(76)80033-X).
- [21] J. P. Connerade and A. V. Solov'yov. “Radiative electron capture by metallic clusters”. In: *J. Phys. B* 29.2 (Jan. 1996), pp. 365–375. ISSN: 0953-4075. doi: [10.1088/0953-4075/29/2/023](https://doi.org/10.1088/0953-4075/29/2/023).
- [22] H. H. Corzo et al. “NR2 and P3+: Accurate, Efficient Electron-Propagator Methods for Calculating Valence, Vertical Ionization Energies of Closed-Shell Molecules”. In: *The Journal of Physical Chemistry A* 119.33 (2015). PMID: 26226061, pp. 8813–8821. doi: [10.1021/acs.jpca.5b00942](https://doi.org/10.1021/acs.jpca.5b00942).
- [23] H.H. Corzo and J.V. Ortiz. “Electron Propagator Theory: Foundations and Predictions”. In: *Adv. Quantum Chem.* 74 (2017), pp. 267–298. doi: [10.1016/bs.aiq.2016.05.001](https://doi.org/10.1016/bs.aiq.2016.05.001).
- [24] Peng Cui and Yuan Xue. “Effects of co-adsorption on interfacial charge transfer in a quantum dot dye composite”. In: *Nanoscale Res. Lett.* 16 (2021). doi: [10.1186/s11671-021-03604-0](https://doi.org/10.1186/s11671-021-03604-0).
- [25] N. D’Angelo. “Recombination of Ions and Electrons”. In: *Phys. Rev.* 121 (2 Jan. 1961), pp. 505–507. doi: [10.1103/PhysRev.121.505](https://doi.org/10.1103/PhysRev.121.505).

- [26] Mohamad Taghi Dejpasand et al. “Tuning HOMO and LUMO of three region (UV, Vis and IR) photoluminescent nitrogen doped graphene quantum dots for photodegradation of methylene blue”. In: *Mater. Res. Bull.* 128 (2020), p. 110886. ISSN: 0025-5408. DOI: <https://doi.org/10.1016/j.materresbull.2020.110886>.
- [27] M. Díaz-Tinoco et al. “Composite electron propagator methods for calculating ionization energies”. In: *J. Chem. Phys.* 144.22 (2016). DOI: [10.1063/1.4953666](https://doi.org/10.1063/1.4953666).
- [28] Manuel Díaz-Tinoco et al. “Composite electron propagator methods for calculating ionization energies”. In: *J. Chem. Phys.* 144.22 (2016), p. 224110.
- [29] Peter I. Djurovich et al. “Measurement of the lowest unoccupied molecular orbital energies of molecular organic semiconductors”. In: *Organic Electronics* 10.3 (2009), pp. 515–520. ISSN: 1566-1199. DOI: <https://doi.org/10.1016/j.orgel.2008.12.011>.
- [30] O. Dolgounitcheva et al. “Accurate Ionization Potentials and Electron Affinities of Acceptor Molecules IV: Electron-Propagator Methods”. In: *J. Chem. Theory Comput.* 12.2 (2016), pp. 627–637. DOI: [10.1021/acs.jctc.5b00872](https://doi.org/10.1021/acs.jctc.5b00872).
- [31] Alexander E. Doran and So Hirata. “Stochastic evaluation of fourth-order many-body perturbation energies”. In: *J. Chem. Phys.* 154.13 (2021), p. 134114. DOI: [10.1063/5.0047798](https://doi.org/10.1063/5.0047798).
- [32] Kevin T. Early and David J. Nesbitt. “Ultrafast Laser Studies of Two-Photon Excited Fluorescence Intermittency in Single CdSe/ZnS Quantum Dots”. In: *Nano Lett.* 15.12 (2015). PMID: 26542640, pp. 7781–7787. DOI: [10.1021/acs.nanolett.5b01139](https://doi.org/10.1021/acs.nanolett.5b01139).
- [33] Pavel D. Elkind and Viktor N. Staroverov. “Energy expressions for Kohn–sham potentials and their relation to the Slater–janak theorem”. In: *J. Chem. Phys.* 136.12 (2012), p. 124115. DOI: [10.1063/1.3695372](https://doi.org/10.1063/1.3695372).
- [34] S. A. Empedocles and M. G. Bawendi. “Quantum-Confined Stark Effect in Single CdSe Nanocrystallite Quantum Dots”. In: *Science* 278.5346 (1997), pp. 2114–2117. DOI: [10.1126/science.278.5346.2114](https://doi.org/10.1126/science.278.5346.2114).
- [35] James Endres et al. “Valence and Conduction Band Densities of States of Metal Halide Perovskites: A Combined Experimental–Theoretical Study”. In: *J. Phys. Chem. Lett.* 7.14 (2016), pp. 2722–2729. DOI: [10.1021/acs.jpcllett.6b00946](https://doi.org/10.1021/acs.jpcllett.6b00946).
- [36] Th. Fauster and V. Dose. “Inverse Photoemission Spectroscopy”. In: *Chemistry and Physics of Solid Surfaces VI*. Berlin, Heidelberg: Springer Berlin Heidelberg, 1986, pp. 483–507. ISBN: 978-3-642-82727-3. DOI: [10.1007/978-3-642-82727-3_18](https://doi.org/10.1007/978-3-642-82727-3_18).
- [37] A.L. Fetter and J.D. Walecka. *Quantum Theory of Many-particle Systems*. Dover Books on Physics. Dover Publications, 2003. ISBN: 9780486428277.
- [38] K.F. Freed and D.L. Yeager. “A wavefunction approach to equations of motion-Green’s function methods”. In: *Chem. Phys.* 22.3 (1977), pp. 401–414. DOI: [10.1016/0301-0104\(77\)89027-7](https://doi.org/10.1016/0301-0104(77)89027-7).
- [39] M. Govoni and G. Galli. “Large Scale GW Calculations”. In: *J. Chem. Theory Comput.* 11.6 (2015), pp. 2680–2696. DOI: [10.1021/ct500958p](https://doi.org/10.1021/ct500958p).
- [40] Yukap Hahn. “Radiative capture and recombination in electron-atom collisions”. In: *Phys. Rev. A* 12 (3 Sept. 1975), pp. 895–907. DOI: [10.1103/PhysRevA.12.895](https://doi.org/10.1103/PhysRevA.12.895).

- [41] W. Heller, U. Bockelmann, and G. Abstreiter. “Electric-field effects on excitons in quantum dots”. In: *Phys. Rev. B* 57 (11 1998), pp. 6270–6273. doi: [10.1103/PhysRevB.57.6270](https://doi.org/10.1103/PhysRevB.57.6270).
- [42] M.F. Herman, D.L. Yeager, and K.F. Freed. “Analysis of third order contributions to equations of motion-green’s function ionization potentials: Application to N₂”. In: *Chem. Phys.* 29.1-2 (1978), pp. 77–96. doi: [10.1016/0301-0104\(78\)85063-0](https://doi.org/10.1016/0301-0104(78)85063-0).
- [43] M.F. Herman et al. “Critical test of equation-of-motion-Green’s function methods. II. Comparison with configuration interaction results”. In: *J. Chem. Phys.* 72.1 (1980), pp. 611–620. doi: [10.1063/1.438951](https://doi.org/10.1063/1.438951).
- [44] I.G. Hill et al. “Charge-separation energy in films of π -conjugated organic molecules”. In: *Chemical Physics Letters* 327.3 (2000), pp. 181–188. issn: 0009-2614. doi: [https://doi.org/10.1016/S0009-2614\(00\)00882-4](https://doi.org/10.1016/S0009-2614(00)00882-4).
- [45] S. Hirata, M. Nooijen, and R.J. Bartlett. “High-order determinantal equation-of-motion coupled-cluster calculations for electronic excited states”. In: *Chem. Phys. Lett.* 326.3-4 (2000), pp. 255–262. doi: [10.1016/S0009-2614\(00\)00772-7](https://doi.org/10.1016/S0009-2614(00)00772-7).
- [46] So Hirata et al. “General-order many-body green’s function method”. In: *J. Chem. Theory Comput.* 11.4 (2015), pp. 1595–1606. doi: [10.1021/acs.jctc.5b00005](https://doi.org/10.1021/acs.jctc.5b00005).
- [47] Byung-Ryool Hyun et al. “Electron Injection from Colloidal PbS Quantum Dots into Titanium Dioxide Nanoparticles”. In: *ACS Nano* 2.11 (2008). PMID: 19206384, pp. 2206–2212. doi: [10.1021/nl800336b](https://doi.org/10.1021/nl800336b).
- [48] Shaunkatali N. Inamdar, Pravin P. Ingole, and Santosh K. Haram. “Determination of Band Structure Parameters and the Quasi-Particle Gap of CdSe Quantum Dots by Cyclic Voltammetry”. In: *ChemPhysChem* 9.17 (2008), pp. 2574–2579. doi: [10.1002/cphc.200800482](https://doi.org/10.1002/cphc.200800482).
- [49] T. Jahnke. “Interatomic and intermolecular Coulombic decay: The coming of age story”. In: *J. Phys. B At. Mol. Opt. Phys.* 48.8 (2015). doi: [10.1088/0953-4075/48/8/082001](https://doi.org/10.1088/0953-4075/48/8/082001).
- [50] Russell D Johnson III. *NIST Computational Chemistry Comparison and Benchmark Database*. <http://cccbdb.nist.gov/> (Accessed May 20, 2022).
- [51] D.B. Jones et al. “Electron-impact ionization of the water molecule at large momentum transfer above the double-ionization threshold”. In: *Phys. Rev. A* 83.1 (2011). doi: [10.1103/PhysRevA.83.012704](https://doi.org/10.1103/PhysRevA.83.012704).
- [52] Stijn Joonen et al. “Enhanced electric field sensitivity of quantum dot/rod two-photon fluorescence and its relevance for cell transmembrane voltage imaging”. In: *Nanophotonics* 10.9 (2021), pp. 2407–2420. doi: [doi:10.1515/nanoph-2021-0077](https://doi.org/10.1515/nanoph-2021-0077).
- [53] Yousung Jung et al. “Auxiliary basis expansions for large-scale electronic structure calculations”. In: *Proc. Natl. Acad. Sci. U.S.A.* 102.19 (2005), pp. 6692–6697.
- [54] M.H. Kalos and P.A. Whitlock. *Monte Carlo Methods*. Wiley, 2009. isbn: 9783527626229.
- [55] M. Kamiya and S. Hirata. “Higher-order equation-of-motion coupled-cluster methods for ionization processes”. In: *J. Chem. Phys.* 125.7 (2006). doi: [10.1063/1.2244570](https://doi.org/10.1063/1.2244570).
- [56] Eric R. Kennehan et al. “Dynamic Ligand Surface Chemistry of Excited PbS Quantum Dots”. In: *J. Phys. Chem. Lett.* 11.6 (2020), pp. 2291–2297. doi: [10.1021/acs.jpclett.0c00539](https://doi.org/10.1021/acs.jpclett.0c00539).

- [57] Svetlana V. Kilina, Patrick K. Tamukong, and Dmitri S. Kilin. “Surface Chemistry of Semi-conducting Quantum Dots: Theoretical Perspectives”. In: *Acc. Chem. Res.* 49.10 (2016), pp. 2127–2135. doi: [10.1021/acs.accounts.6b00196](https://doi.org/10.1021/acs.accounts.6b00196).
- [58] Mee Rahn Kim and Dongling Ma. “Quantum-Dot-Based Solar Cells: Recent Advances, Strategies, and Challenges”. In: *The Journal of Physical Chemistry Letters* 6.1 (2015), pp. 85–99. doi: [10.1021/jz502227h](https://doi.org/10.1021/jz502227h).
- [59] J.W. Knight et al. “Accurate Ionization Potentials and Electron Affinities of Acceptor Molecules III: A Benchmark of GW Methods”. In: *J. Chem. Theory Comput.* 12.2 (2016), pp. 615–626. doi: [10.1021/acs.jctc.5b00871](https://doi.org/10.1021/acs.jctc.5b00871).
- [60] A. V. Korol, F. J. Currell, and G. F. Gribakin. “The role of target polarization in electron–ion recombination”. In: *J. Phys. B* 37.11 (2004), p. 2411. doi: [10.1088/0953-4075/37/11/017](https://doi.org/10.1088/0953-4075/37/11/017).
- [61] A. V. Korol, G. F. Gribakin, and F. J. Currell. “Effect of target polarization in electron-ion recombination”. In: *Phys. Rev. Lett.* 97.22 (2006), p. 223201. doi: [10.1103/PhysRevLett.97.223201](https://doi.org/10.1103/PhysRevLett.97.223201).
- [62] Leeor Kronik et al. “PARSEC – the pseudopotential algorithm for real-space electronic structure calculations: recent advances and novel applications to nano-structures”. In: *Phys. Status Solidi B* 243.5 (2006), pp. 1063–1079. doi: <https://doi.org/10.1002/pssb.200541463>.
- [63] Erol Kucur et al. “Determination of quantum confinement in CdSe nanocrystals by cyclic voltammetry”. In: *J. Chem. Phys.* 119.4 (July 2003), pp. 2333–2337. ISSN: 0021-9606. doi: [10.1063/1.1582834](https://doi.org/10.1063/1.1582834).
- [64] C. Lemieux. *Monte Carlo and Quasi-Monte Carlo Sampling*. Springer Series in Statistics. Springer New York, 2009. ISBN: 9780387781655.
- [65] G. Leobacher and F. Pillichshammer. *Introduction to Quasi-Monte Carlo Integration and Applications*. Compact Textbooks in Mathematics. Springer International Publishing, 2014. ISBN: 9783319034256.
- [66] Patrick J. Lestrange et al. “Density of States Guided Møller–Plesset Perturbation Theory”. In: *J. Chem. Theory Comput.* 10.5 (2014). PMID: 26580520, pp. 1910–1914. doi: [10.1021/ct400765a](https://doi.org/10.1021/ct400765a).
- [67] Dehui Li et al. “Electric-Field-Dependent Photoconductivity in CdS Nanowires and Nanobelts: Exciton Ionization, Franz–Keldysh, and Stark Effects”. In: *Nano Letters* 12.6 (2012). PMID: 22642694, pp. 2993–2999. doi: [10.1021/nl300749z](https://doi.org/10.1021/nl300749z).
- [68] A. G. Lyalin and A. V. Solov’yov. “Polarizational bremsstrahlung from atomic clusters”. In: *Radiat. Phys. Chem.* 75.10 (2006), pp. 1358–1379. ISSN: 0969-806X. doi: [10.1016/j.radphyschem.2006.01.002](https://doi.org/10.1016/j.radphyschem.2006.01.002).
- [69] Xuedan Ma, Alf Mews, and Tobias Kipp. “Determination of Electronic Energy Levels in Type-II CdTe-Core/CdSe-Shell and CdSe-Core/CdTe-Shell Nanocrystals by Cyclic Voltammetry and Optical Spectroscopy”. In: *J. Phys. Chem. C* 117.32 (2013), pp. 16698–16708. doi: [10.1021/jp404556b](https://doi.org/10.1021/jp404556b).

- [70] N.T. Maitra. “Perspective: Fundamental aspects of time-dependent density functional theory”. In: *J. Chem. Phys.* 144.22 (2016). DOI: [10.1063/1.4953039](https://doi.org/10.1063/1.4953039).
- [71] George Marsaglia. “Choosing a Point from the Surface of a Sphere”. In: *The Annals of Mathematical Statistics* 43.2 (1972), pp. 645–646. ISSN: 00034851.
- [72] B.K. McFarland et al. “Ultrafast X-ray Auger probing of photoexcited molecular dynamics”. In: *Nat. Commun.* 5 (2014). DOI: [10.1038/ncomms5235](https://doi.org/10.1038/ncomms5235).
- [73] Peter F. McLaughlin and Arindam Chakraborty. “Compact Real-Space Representation of Excited States Using Frequency-Dependent Explicitly Correlated Electron–Hole Interaction Kernel”. In: *J. Chem. Theory Comput.* 16.9 (2020), pp. 5762–5770. DOI: [10.1021/acs.jctc.9b01238](https://doi.org/10.1021/acs.jctc.9b01238).
- [74] Robert W. Meulenbergh et al. “Determination of the Exciton Binding Energy in CdSe Quantum Dots”. In: *ACS Nano* 3.2 (2009). PMID: 19236067, pp. 325–330. DOI: [10.1021/nm8006916](https://doi.org/10.1021/nm8006916).
- [75] D. A. B. Miller et al. “Band-Edge Electroabsorption in Quantum Well Structures: The Quantum-Confined Stark Effect”. In: *Phys. Rev. Lett.* 53 (22 Nov. 1984), pp. 2173–2176. DOI: [10.1103/PhysRevLett.53.2173](https://doi.org/10.1103/PhysRevLett.53.2173).
- [76] Elisa M. Miller et al. “Revisiting the Valence and Conduction Band Size Dependence of PbS Quantum Dot Thin Films”. In: *ACS Nano* 10.3 (2016), pp. 3302–3311. DOI: [10.1021/acsnano.5b06833](https://doi.org/10.1021/acsnano.5b06833).
- [77] M. Morkel et al. “Flat conduction-band alignment at the CdS/CuInSe₂ thin-film solar-cell heterojunction”. In: *Appl. Phys. Lett.* 79.27 (2001), pp. 4482–4484. DOI: [10.1063/1.1428408](https://doi.org/10.1063/1.1428408).
- [78] Mervin E. Muller. “A Note on a Method for Generating Points Uniformly on N-Dimensional Spheres”. In: *Commun. ACM* 2.4 (Apr. 1959), pp. 19–20. ISSN: 0001-0782. DOI: [10.1145/377939.377946](https://doi.org/10.1145/377939.377946).
- [79] I.B. Müller and L.S. Cederbaum. “Ionization and double ionization of small water clusters”. In: *J. Chem. Phys.* 125.20 (2006). DOI: [10.1063/1.2357921](https://doi.org/10.1063/1.2357921).
- [80] Sultana N. Nahar and Anil K. Pradhan. “Unified treatment of electron-ion recombination in the close-coupling approximation”. In: *Phys. Rev. A* 49 (3 Mar. 1994), pp. 1816–1835. DOI: [10.1103/PhysRevA.49.1816](https://doi.org/10.1103/PhysRevA.49.1816).
- [81] Toshio Nishi et al. “Electronic structures of ionic liquids [Cnmim]+BF₄[−] and [Cnmim]+PF₆[−] studied by ultraviolet photoemission, inverse photoemission, and near-edge X-ray absorption fine structure spectroscopies”. In: *Chemical Physics Letters* 455.4 (2008), pp. 213–217. ISSN: 0009-2614. DOI: <https://doi.org/10.1016/j.cplett.2008.01.049>.
- [82] M. Nooijen and J.G. Snijders. “Coupled cluster approach to the single-particle Green’s function”. In: *Int. J. Quantum Chem.* 44.26 S (1992), pp. 55–83. DOI: [10.1002/qua.560440808](https://doi.org/10.1002/qua.560440808).
- [83] M. Nooijen and J.G. Snijders. “Coupled cluster Green’s function method: Working equations and applications”. In: *Int. J. Quantum Chem.* 48.1 (1993), pp. 15–48. DOI: [10.1002/qua.560480103](https://doi.org/10.1002/qua.560480103).

- [84] Marcel Nooijen and Jaap G. Snijders. “Coupled cluster approach to the single-particle Green’s function”. In: *Int. J. Quantum Chem.* 44.S26 (1992), pp. 55–83. doi: <https://doi.org/10.1002/qua.560440808>.
- [85] T. Ollonqvist et al. “Inverse photoemission and photoemission spectra of the PbS(001) surface”. In: *Journal of Electron Spectroscopy and Related Phenomena* 76 (1995). Proceedings of the Sixth International Conference on Electron Spectroscopy, pp. 729–734. ISSN: 0368-2048. doi: [https://doi.org/10.1016/0368-2048\(95\)02434-4](https://doi.org/10.1016/0368-2048(95)02434-4).
- [86] Daniel Opalka et al. “The ionization potential of aqueous hydroxide computed using many-body perturbation theory”. In: *J. Chem. Phys.* 141.3 (2014), p. 034501. doi: [10.1063/1.4887259](https://doi.org/10.1063/1.4887259).
- [87] J.V. Ortiz. “Electron propagator theory: An approach to prediction and interpretation in quantum chemistry”. In: *Wiley Interdiscip. Rev. Comput. Mol. Sci.* 3.2 (2013), pp. 123–142. doi: [10.1002/wcms.1116](https://doi.org/10.1002/wcms.1116).
- [88] JV Ortiz. “A nondiagonal, renormalized extension of partial third-order quasiparticle theory: Comparisons for closed-shell ionization energies”. In: *J. Chem. Phys.* 108.3 (1998), pp. 1008–1014.
- [89] Lazaro A. Padilha et al. “Spectral Dependence of Nanocrystal Photoionization Probability: The Role of Hot-Carrier Transfer”. In: *ACS Nano* 5.6 (2011), pp. 5045–5055. doi: [10.1021/nl201135k](https://doi.org/10.1021/nl201135k).
- [90] Vasili Perebeinos and Phaedon Avouris. “Exciton Ionization, Franz-Keldysh, and Stark Effects in Carbon Nanotubes”. In: *Nano Letters* 7.3 (2007), pp. 609–613. doi: [10.1021/nl0625022](https://doi.org/10.1021/nl0625022).
- [91] P.A. Pieniazek et al. “Benchmark full configuration interaction and equation-of-motion coupled-cluster model with single and double substitutions for ionized systems results for prototypical charge transfer systems: Noncovalent ionized dimers”. In: *J. Chem. Phys.* 127.16 (2007). doi: [10.1063/1.2795709](https://doi.org/10.1063/1.2795709).
- [92] Y. Ping, D. Rocca, and G. Galli. “Electronic excitations in light absorbers for photoelectrochemical energy conversion: First principles calculations based on many body perturbation theory”. In: *Chem. Soc. Rev.* 42.6 (2013), pp. 2437–2469. doi: [10.1039/c3cs00007a](https://doi.org/10.1039/c3cs00007a).
- [93] Pavel Pokhilko, Daniil Izmodenov, and Anna I. Krylov. “Extension of frozen natural orbital approximation to open-shell references: Theory, implementation, and application to single-molecule magnets”. In: (2019). doi: [10.26434/chemrxiv.10308053](https://doi.org/10.26434/chemrxiv.10308053).
- [94] William H Press et al. *Numerical recipes in Fortran 90 the art of parallel scientific computing*. Cambridge university press, 1996.
- [95] D.S. Ranasinghe et al. “Vertical valence ionization potential benchmarks from equation-of-motion coupled cluster theory and QTP functionals”. In: *J. Chem. Phys.* 150.7 (2019). doi: [10.1063/1.5084728](https://doi.org/10.1063/1.5084728).
- [96] Duminda S. Ranasinghe et al. “Vertical valence ionization potential benchmarks from equation-of-motion coupled cluster theory and QTP functionals”. In: *The Journal of Chemical Physics* 150.7 (Feb. 2019), p. 074108. ISSN: 0021-9606. doi: [10.1063/1.5084728](https://doi.org/10.1063/1.5084728).

- [97] Clare E. Rowland et al. “Electric Field Modulation of Semiconductor Quantum Dot Photoluminescence: Insights Into the Design of Robust Voltage-Sensitive Cellular Imaging Probes”. In: *Nano Letters* 15.10 (2015), pp. 6848–6854. DOI: [10.1021/acs.nanolett.5b02725](https://doi.org/10.1021/acs.nanolett.5b02725).
- [98] R.Y. Rubinstein and D.P. Kroese. *Simulation and the Monte Carlo Method*. Wiley Series in Probability and Statistics. Wiley, 2016. ISBN: 9781118632161.
- [99] Reuven Rubinstein. “Stochastic enumeration method for counting NP-Hard problems”. In: *Methodol. Comput. Appl. Probab.* 15.2 (2011), pp. 249–291. DOI: [10.1007/s11009-011-9242-y](https://doi.org/10.1007/s11009-011-9242-y).
- [100] A. Rudenko et al. “Femtosecond response of polyatomic molecules to ultra-intense hard X-rays”. In: *Nature* 546.7656 (2017), pp. 129–132. DOI: [10.1038/nature22373](https://doi.org/10.1038/nature22373).
- [101] E. Runge and E.K.U. Gross. “Density-functional theory for time-dependent systems”. In: *Phys. Rev. Lett.* 52.12 (1984), pp. 997–1000. DOI: [10.1103/PhysRevLett.52.997](https://doi.org/10.1103/PhysRevLett.52.997).
- [102] G. Sansone et al. “Electron correlation in real time”. In: *ChemPhysChem* 13.3 (2012), pp. 661–680. DOI: [10.1002/cphc.201100528](https://doi.org/10.1002/cphc.201100528).
- [103] Samim Sardar et al. “Enhanced Charge Separation and FRET at Heterojunctions between Semiconductor Nanoparticles and Conducting Polymer Nanofibers for Efficient Solar Light Harvesting”. English. In: *Sci. Rep.* 5 (Nov. 2015). Copyright - Copyright Nature Publishing Group Nov 2015; Last updated - 2019-09-25, p. 17313.
- [104] J. Schirmer, L.S. Cederbaum, and O. Walter. “New approach to the one-particle Green’s function for finite Fermi systems”. In: *Phys. Rev. A* 28.3 (1983), pp. 1237–1259. DOI: [10.1103/PhysRevA.28.1237](https://doi.org/10.1103/PhysRevA.28.1237).
- [105] P. Schulz et al. “Interface energetics in organo-metal halide perovskite-based photovoltaic cells”. In: *Energy Environ. Sci.* 7.4 (2014), pp. 1377–1381. DOI: [10.1039/c4ee00168k](https://doi.org/10.1039/c4ee00168k).
- [106] P. Senellart, G. Solomon, and A. White. “High-performance semiconductor quantum-dot single-photon sources”. In: *Nature Nanotechnology* 12.11 (2017). cited By 517, pp. 1026–1039. DOI: [10.1038/nnano.2017.218](https://doi.org/10.1038/nnano.2017.218).
- [107] R. Shankar. *Principles of Quantum Mechanics*. Springer US, 2012. ISBN: 9781475705768.
- [108] Dharmendar Kumar Sharma et al. “Stark Effect and Environment-Induced Modulation of Emission in Single Halide Perovskite Nanocrystals”. In: *ACS Nano* 13.1 (2019), pp. 624–632. DOI: [10.1021/acs.nano.8b07677](https://doi.org/10.1021/acs.nano.8b07677).
- [109] Michael D Shields et al. “Refined stratified sampling for efficient Monte Carlo based uncertainty quantification”. In: *Reliab. Eng. Syst. Saf.* 142 (2015), pp. 310–325.
- [110] J. Simons. *Equations of motion methods for computing electron affinities and ionization potentials*. 2005. DOI: [10.1016/B978-044451719-7/50060-3](https://doi.org/10.1016/B978-044451719-7/50060-3).
- [111] J. Simons and W.D. Smith. “Theory of electron affinities of small molecules”. In: *J. Chem. Phys.* (1973), pp. 4908–4911.
- [112] R.K. Singh, J.V. Ortiz, and M.K. Mishra. “Tautomeric forms of adenine: Vertical ionization energies and Dyson orbitals”. In: *Int. J. Quantum Chem.* 110.10 (2010), pp. 1901–1915. DOI: [10.1002/qua.22363](https://doi.org/10.1002/qua.22363).

- [113] N V Smith. “Inverse photoemission”. In: *Rep. Prog. Phys.* 51.9 (Sept. 1988), pp. 1227–1294. DOI: [10.1088/0034-4885/51/9/003](https://doi.org/10.1088/0034-4885/51/9/003).
- [114] Nicole Spanedda et al. “Investigation of Ionization Potential in Quantum Dots Using the Stratified Stochastic Enumeration of Molecular Orbitals Method”. In: *Journal of Chemical Theory and Computation* 18.10 (2022). PMID: 36136935, pp. 5920–5935. DOI: [10.1021/acs.jctc.2c00329](https://doi.org/10.1021/acs.jctc.2c00329).
- [115] *Supporting Information: Description of stratified sampling and common random number sampling is presented in the supporting information. This material is available free of charge via the Internet at <http://pubs.acs.org>.*
- [116] A. Szabo and N.S. Ostlund. *Modern Quantum Chemistry: Introduction to Advanced Electronic Structure Theory*. Dover Books on Chemistry. Dover Publications, 2012. ISBN: 9780486134598.
- [117] De Nyago Tafen and Oleg V. Prezhdo. “Size and Temperature Dependence of Electron Transfer between CdSe Quantum Dots and a TiO₂ Nanobelt”. In: *J. Phys. Chem. C* 119.10 (2015), pp. 5639–5647. DOI: [10.1021/jp5110278](https://doi.org/10.1021/jp5110278).
- [118] Ryota Usui and Hiroyuki Yoshida. “Enhancement of Signal Intensity for Inverse Photoelectron Spectroscopy by Surface Plasmon Resonance of Ag Nanoparticles”. In: *The Journal of Physical Chemistry C* 123.47 (2019), pp. 28789–28794. DOI: [10.1021/acs.jpcc.9b08814](https://doi.org/10.1021/acs.jpcc.9b08814).
- [119] Vojtech Vlcek et al. “Stochastic GW calculations for molecules”. In: *J. Chem. Theory Comput.* 13.10 (2017), pp. 4997–5003.
- [120] J.F. Ward. “DNA Damage Produced by Ionizing Radiation in Mammalian Cells: Identities, Mechanisms of Formation, and Reparability”. In: *Prog. Nucleic Acid Res. Mol. Biol.* 35.C (1988), pp. 95–125. DOI: [10.1016/S0079-6603\(08\)60611-X](https://doi.org/10.1016/S0079-6603(08)60611-X).
- [121] N.J. Watkins et al. “Electron spectra of a self-assembled monolayer on gold: Inverse photoemission and two-photon photoemission spectroscopy”. In: *Chemical Physics Letters* 446.4 (2007), pp. 359–364. ISSN: 0009-2614. DOI: <https://doi.org/10.1016/j.cplett.2007.08.070>.
- [122] Soohaeng Yoo Willow and So Hirata. “Stochastic, real-space, imaginary-time evaluation of third-order Feynman–Goldstone diagrams”. In: *The Journal of Chemical Physics* 140.2 (Jan. 2014), p. 024111. ISSN: 0021-9606. DOI: [10.1063/1.4861561](https://doi.org/10.1063/1.4861561).
- [123] Soohaeng Yoo Willow, Kwang S Kim, and So Hirata. “Stochastic evaluation of second-order Dyson self-energies”. In: *J. Chem. Phys.* 138.16 (2013), p. 164111.
- [124] Soohaeng Yoo Willow, Kwang S. Kim, and So Hirata. “Stochastic evaluation of second-order Dyson self-energies”. In: *J. Chem. Phys.* 138.16 (2013), p. 164111. DOI: [10.1063/1.4801862](https://doi.org/10.1063/1.4801862).
- [125] Soohaeng Yoo Willow et al. “Convergence Acceleration of Parallel Monte Carlo Second-Order Many-Body Perturbation Calculations Using Redundant Walkers”. In: *Journal of Chemical Theory and Computation* 9.10 (2013), pp. 4396–4402. DOI: [10.1021/ct400557z](https://doi.org/10.1021/ct400557z).




- [126] Hiroyuki Yoshida. “Near-ultraviolet inverse photoemission spectroscopy using ultra-low energy electrons”. In: *Chemical Physics Letters* 539-540 (2012), pp. 180–185. ISSN: 0009-2614. DOI: <https://doi.org/10.1016/j.cplett.2012.04.058>.
- [127] Benjamin Young, James Warner, and David Heskett. “Ion bombardment of Ni(110) studied with inverse photoemission spectroscopy and low-energy electron diffraction”. In: *Surface Science* 644 (2016), pp. 64–68. ISSN: 0039-6028. DOI: <https://doi.org/10.1016/j.susc.2015.09.020>.
- [128] Qilin Yuan et al. “A review on the electroluminescence properties of quantum-dot light-emitting diodes”. In: *Organic Electronics* 90 (2021), p. 106086. ISSN: 1566-1199. DOI: <https://doi.org/10.1016/j.orgel.2021.106086>.
- [129] Dietrich R.T. Zahn, Gianina N. Gavrilă, and Mihaela Gorgoi. “The transport gap of organic semiconductors studied using the combination of direct and inverse photoemission”. In: *Chem. Phys.* 325.1 (2006), pp. 99–112. ISSN: 0301-0104. DOI: [10.1016/j.chemphys.2006.02.003](https://doi.org/10.1016/j.chemphys.2006.02.003).
- [130] Haiming Zhu et al. “Auger-assisted electron transfer from photoexcited semiconductor quantum dots”. In: *Nano Lett.* 14.3 (2014), pp. 1263–1269. DOI: [10.1021/nl4041687](https://doi.org/10.1021/nl4041687).

Curriculum Vitae

Nicole Spanedda

✉ nspanedd@syr.edu mobile:(973)-714-5769

Education

- September 5th 2023  **Ph.D. in Chemistry:** Syracuse University
 Thesis title: *Development of Stochastic and Time-Dependent Quantum Chemical Methods for Accurate Description of Light-Matter Interactions with Applications in Photoionization and Inverse Photoemission in Nanomaterials*
- May 2020  **M.S. in Chemistry:** Syracuse University
- May 2018  **Bachelor of Science in Chemistry:** Fairleigh Dickinson University

Research Publications

- Spanedda, N., McLaughlin, P. F., Beyer, J. J., & Chakraborty, A. (2022). Investigation of Ionization Potential in Quantum Dots Using the Stratified Stochastic Enumeration of Molecular Orbitals Method. *Journal of Chemical Theory and Computation*, 18(10), 5920-5935. [link to paper](#) and [link to supporting info](#).
- Rodrigues, N., Mohan, C.K., Spanedda, N & Chakraborty, A. (2023) Accelerating Quantum Chemistry Calculations: Machine Learning for Efficient Evaluation of Electron-Repulsion Integrals (accepted 06/2023 *International Conference on Quantum Mechanics and Machine Learning*)
- Spanedda, N., Mesta, K. & Chakraborty, A. (2023) Enhancement of spontaneous photon emission in inverse photoemission transitions in semiconductor quantum dots (very recently submitted)

Research Experience

Experience: My PhD research has been focused on developing quantum chemistry methods in order to solve challenging quantum chemistry problems in a highly efficient and accurate manner. In particular, I have focused on developing methodology for predicting the electronic properties and investigating the spectroscopic properties of nanomaterials. One of the most unique aspects of my research experience is that I have experience in applying techniques that are primarily used in fields outside of quantum chemistry, for the purpose of solving very computationally expensive quantum chemistry problems. This experience is valuable and highly applicable for investigating a variety of properties of very large chemical systems and nanomaterials, which can be a very computationally expensive endeavor. This particular experience is best demonstrated by the methodology presented in the paper, Investigation of Ionization Potential in Quantum Dots Using the Stratified Stochastic Enumeration of Molecular Orbitals Method, published in the *Journal of Chemical Theory and Computation*. A second thing that makes my particular experience unique is

that, during my PhD research career, I have gained experience in interdisciplinary collaborative research with computer scientists who specialize in machine-learning. During my time in the Chakraborty group at Syracuse University, I have gained a deep knowledge of electronic structure theory and I have achieved a strong knowledge base in the theoretical details of many-body perturbation theory, Green's function theory, real-space correlated methods, time-dependent perturbation theory, along with practical experience in implementing these methods.

Programming, Computing, and Software Experience:

Programming in FORTRAN, Julia, Python, and Latex, Test-driven software development, Grid computing, High throughput computing, parallel computing, expert user of TeraChem, Q-Chem, Avogadro, and Linux environments

Academic background:

Knowledgeable in the fields of quantum chemistry, quantum and statistical mechanics, physical chemistry, theoretical and computational spectroscopy, solid state chemistry, inorganic chemistry, statistics, and mathematics (analytical and numerical)

Conference Presentations (presenter and co-author)

Year 2023: 2 presentations

1. *Investigation of two-photon photoemission process in semiconductor nanoparticles using explicitly correlated quasiparticle kernel and diagrammatic many-body perturbation theory*
Session: Quantum Chemistry at National Meeting of American Chemical Society Spring 2023
[link to abstract](#)
2. *Investigation of inverse photoemission and field-assisted radiative electron capture in semiconductor nanoparticles*
Session: First-Principles Simulations of Excited-State Phenomena at National Meeting of the American Physical Society 2023 [link to abstract](#)

Year 2022: 8 presentations

1. *Investigation of size-dependent ionization potentials of PbS quantum dots*
Session: Photocatalysis and Photoelectrocatalysis: from Synthesis, Characterization, and Theoretical Studies of Advanced Materials to Clean Energy Applications at National Meeting of American Chemical Society Spring 2022 [link to abstract](#)
2. *Impact of surface ligand coverage on ionization potential of semiconductor nanoparticles*
Session: Frontiers and Challenges in Nanoparticle-Mediated Chemical Transformations at National Meeting of American Chemical Society Spring 2022 [link to abstract](#)
3. *Inverse photoemission energies and oscillator strengths in PbS, PbSe, CdSe, and CdS quantum dots*
Session: Photocatalysis and Photoelectrocatalysis: from Synthesis, Characterization, and Theoretical Studies of Advanced Materials to Clean Energy Applications at National Meeting of American Chemical Society Spring 2022 [link to abstract](#)
4. *Characterization of electron detachment energies in silver nanowires*
Session: Chemistry of Materials – Nanomaterials Session at National Meeting of American Chemical Society Spring 2022 [link to abstract](#)

5. *Calculation of ionization energies and electron affinities of quantum dots and nanowires*
Session: Division of Colloid & Surface Chemistry and at Sci Mix at National Meeting of American Chemical Society Spring 2022 [link to abstract](#)
6. *First-principles construction of frequency-dependent self-energy operator using stochastically enumerated stratified sampling of molecular orbitals method*
Session: Division of Physical Chemistry at National Meeting of American Chemical Society Spring 2022 [link to abstract](#)
7. *Construction of Bayesian mixture model for efficient calculation of electron-hole interaction kernel in quantum dots*
Session: Machine Learning for Quantum Matter III at National Meeting of the American Physical Society 2022 [link to abstract](#)
8. *Characterization of weak and strong dot-to-dot interaction in electronically coupled double quantum dots*
Session: Nanomaterials and Applications at National Meeting of the American Physical Society 2022 [link to abstract](#)
9. *Investigation of ionization energies and photoelectron cross-section of semiconductor quantum dots beyond the electric dipole approximation*
Session: Poster Session II at National Meeting of the American Physical Society 2022 [link to abstract](#)

Year 2019: 1 presentation

1. *First-principles construction of frequency-dependent self-energy operator using stochastically enumerated stratified sampling of molecular orbitals method*
Poster presented at Penn Conference in Theoretical Chemistry (PCTC): University of Pennsylvania

Projects near to completion:

1. Spanedda, N., Gao, C., Chaudhuri, A, & Chakraborty, A. (2023) Nonlinear Stark effect and field-assisted photoionization in semiconductor quantum dots (manuscript close to completion and to be submitted to *The Journal of Physical Chemistry C*)
2. Spanedda, N., Ross, D.H. & Chakraborty, A. (2023) Development of stratified diagrammatic Monte Carlo method for efficient construction of the self-energy operator (manuscript close to completion and to be submitted to *Physical Review B*)
3. Spanedda, N., Mesta, K. & Chakraborty, A. (2023) Investigation of 2-photon photoionization spectra in semiconductor quantum dots using explicitly correlated methods and diagrammatic many-body perturbation theory (manuscript in progress)
4. Spanedda, N., Nangia, S. & Chakraborty, A. (2023) Calculation of distance-dependent ionization potentials of electronically coupled quantum dots (manuscript in progress)

References

1. **Ari Chakraborty** (Research advisor) [archakra@syr.edu]
2. **Chilukuri K Mohan** [ckmohan@syr.edu]
3. **Shivangi Nangia** [nangia@hartford.edu]